Optimized Nonlinear Substrate Integrated Waveguide for Pulse Compression

by

Byron Caudle

A dissertation submitted to the Graduate Faculty of
Auburn University
in partial fulfillment of the
requirements for the Degree of
Doctor of Philosophy

Auburn, Alabama
May 5, 2013

Keywords: FDTD, NLTL, Ferroelectrics, Pulse Compression

Approved by

Michael Baginski, Chair, Associate Professor of Electrical and Computer Engineering
Stuart Wentworth, Associate Professor of Electrical and Computer Engineering
Lloyd Riggs, Professor of Electrical and Computer Engineering
Michael Hamilton, Assistant Professor of Electrical and Computer Engineering
Hulya Kirkici, Professor of Electrical and Computer Engineering
George Flowers, Dean of the Graduate School and Professor of Mechanical Engineering

Abstract

The time compression and associated frequency broadening of electromagnetic pulses has numerous applications in communication and radar systems. In this work, a new type of pulse compression device based on nonlinear ferroelectric materials in a substrate integrated waveguide (SIW) is proposed and simulated, with low temperature co-fired ceramic (LTCC) fabrication compatibility considered. The ferroelectric material Barium Strontium Titanate ($Ba_xSr_{x-1}TiO_3$) commonly used with tunable microwave components, is placed in vertical slabs within the SIW and driven with an input pulse into the nonlinear polarization region. The nonlinearity causes field amplitude dependent propagation velocity, resulting in a tendency for energy to "pile-up" or compress in time. The fields within the SIW are simulated with a Finite Difference Time Domain (FDTD) method, and a Genetic Algorithm (GA) finds the optimal material configuration that maximizes pulse compression. Pulse compression of 58% is shown by simulation to be possible with the proposed design.

Acknowledgments

I would like to thank my parents, Alan and the late Ellen Caudle, for their encouragement and support of graduate education. I would also like to thank my wife, Kali, for her great care and encouragement during the last two years of my Ph.D. program. Finally, I would like to thank my advisor, Dr. Micheal Baginski and my committee for their time and insight into the many challenging problems encountered.

Table of Contents

List of Figures

List of Tables

List of Abbreviations

α	Real Part of Propagation Constant (loss term)
Δs	Spatial Step
Δt	Time Step
η	Intrinsic Impedance
γ	Propagation Constant
λ_g	Guided Wavelength
$\mathbf{B}$	Magnetic Flux Density $[Wb/m^2]$
$\mathbf{D}$	Electric Flux Density $[C/m^2]$
$\mathbf{E}$	Electric Field $[V/m]$
$\mathbf{H}$	Magnetic Field $[A/m]$
$\mathbf{J}$	Current Density [A/m]
$\mathbf{J}_c$	Conduction Current Density [A/m]
$\mathbf{P}$	Polarization Density $[C/m^2]$
μ	Magnetic Permeability [Webers per meter]
μ_0	Vacuum Magnetic Permeability $= 4\pi \times 10^{-7}$ [Webers per meter]
μ_r	Relative Magnetic Permeability
σ	Conductivity [Siemens per meter]

τ_r	Rise Time
ε	Dielectric Permittivity [Farads per meter]
ε_0	Vacuum Dielectric Permittivity $= 8.854 \times 10^{-12}$ [Farads per meter]
ε_r	Relative Dielectric Permittivity
c	Speed of Light in Vacuum $= 3 \times 10^8$ m/s
C_c	Curie-Weiss constant
$f_{c_{nm}}$	Cutoff Frequency for the n^{th} horizontal and m^{th} vertical mode
k	Wave Number
$p(r)$	Charge Density
P_{sat}	Saturation Polarization
T_0	Curie-Weiss temperature
v_g	Group Velocity
v_p	Phase Velocity
Z_0	Transmission Line Characteristic Inpedance
BST	Barium Strontium Titanate ($Ba_xSt_{x-1}TiO_3$)
CPML	Convolutional Perfectly Matched Layer
CPW	Coplanar Waveguide
FDTD	Finite Difference Time Domain
GA	Genetic Algorithm
LTCC	Low Temperature Cofired Ceramic

NLTL	Nonlinear Transmission Line
RAM	Random Access Memory
SIW	Substrate Integrated Waveguide
TE	Transverse Electric
TEM	Transverse Electric and Magnetic
TM	Transverse Magnetic

Chapter 1

Introduction

The generation and transmission of short duration, broadband electromagnetic pulses has been of significant interest to the communications and defense industries for at least the last decade. Multi-path fading, selective absorption, and multiuser interference make narrow bandwidth ($f \; < 5MHz$) communication signals especially difficult to use in indoor environments. Ultra wideband communications signals and radar pulses have significant immunity to these frequency dependent effects and thus offer a distinct advantages for indoor communications. On a larger scale, wideband radar pulses are much more difficult to jam and largely defeat radar absorbing materials, when compared to narrow bandwidth pulses. Pulses with ultra-short rise times are also used as trigger signals for larger circuits.

The generation, transmission and radiation of such wideband pulses has historically been challenging due to frequency dependent dispersion and narrow bandwidth tuning circuits. All transmission lines experience frequency dispersion due to parasitic reactance, thus deviating from a true linear response to a wideband signal. These nonlinear effects can be exploited through the creation of specialized structures known as Nonlinear Transmission Lines (NLTLs), to change a waveform's shape during propagation. Much work has gone into designing nonlinear transmission lines that maximize pulse compression for the production of solitary waves also known as solitons. A historical perspective and review of NLTL designs is given in Chapter 2.

This works exploits the nonlinear amplitude response of the ferroelectric material Barium Strontium Titanate ($Ba_xSt_{x-1}TiO_3$) (BST) to cause spatial and temporal compression. While most prior NLTL designs focused on lumped nonlinear elements in ladder networks or ferrite shock lines, this work examines the use of a new type of NLTL formed by a rectangular waveguide. Waveguides offer an attractive alternative to microstrip traces and coaxial cable transmission lines due to better isolation and higher power handling. The recent development of substrate integrated waveguides (SIWs) has demonstrated that waveguide structures can be formed at the circuit board and micro-fabrication level. The primary goal of this work is the combination of classical NLTL and SIW concepts to form an optimized pulse compression system. The design is simulated with the Finite Difference Time Domain (FDTD) method and a Genetic Algorithm (GA) optimally selects material options and dimensions. The design considers fabrication in Low Temperature Cofired Ceramic (LTCC) with a Sol-Gel process used to fill trenches (vias in the LTCC) with ferroelectric material. A review of waveguides and ferroelectric materials necessary for development of the design is given in Chapter 3.

Chapter 2

Background

2.1 Nonlinear Transmission Lines

All transmission lines have nonlinear effects that cause less than perfect, linear, loss-less propagation of electromagnetic energy. In particular, parasitic inductance and capacitance, along with frequency dependence of the dielectric permittivity ε and magnetic permeability μ, causes waveform components to propagate with velocity as function of frequency. The wide range of frequency components that make up a short duration Gaussian pulse will spread out, or disperse, as they propagate down a real transmission line. This frequency dispersion effect usually broadens the pulse time signature. The term “Nonlinear Transmission Line” refers to the intentional exploitation of nonlinear effects to achieve a specific change in a transmitted wave, as first studied by Landauer [13]. Most NLTL designs are based on a goal of pulse compression caused by superposition of portions of the input pulse in time. This is accomplished by changing the propagation velocity of different portions of the pulse such that they will “pile-up” at the same instant in time. The compressed pulse has a greater peak power over a shorter period of time in comparison to the input pulse. As the pulse is compressed in time, simple Fourier analysis gives an associated bandwidth broadening of the spectral density of the pulse. The compressive effect is commonly measured as the reduction in pulse rise time (τ_r) from input to output, as given by percent compression:

$$Compression = \frac{\tau_{r_{initial}} - \tau_{r_{final}}}{\tau_{r_{initial}}} \times 100; \tag{2.1}$$

Some NLTL designs specifically seek to maximize the frequency spectrum broadening effect of pulse compression. Third order and higher harmonics can be generated at high

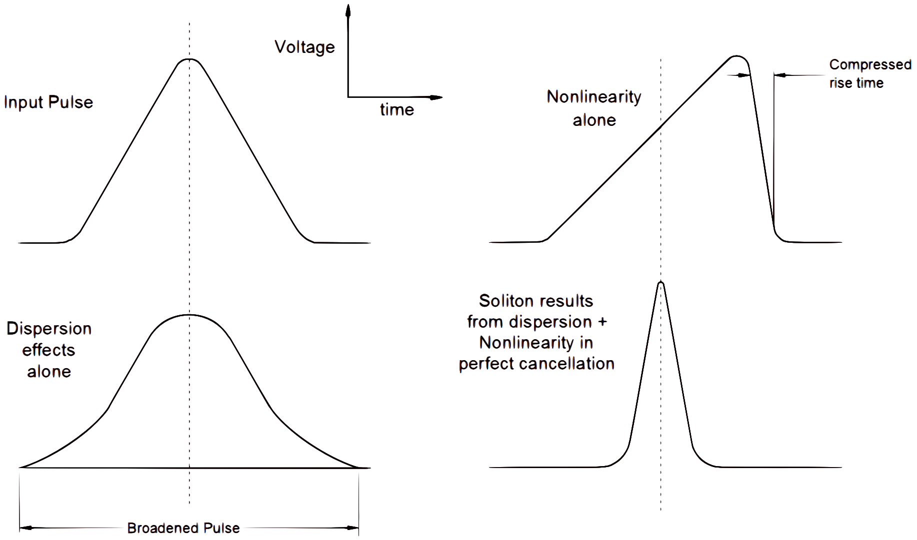

Figure 2.1: Combination of dispersion and NLTL compression to create solitons

power levels, which may prove useful at frequencies and power levels beyond what can be produced by direct synthesis [14, 15].

In 1845, Russell [16] introduced the concept of a solitary water wave. These solitary waves are now known as solitons [17]. A pure soliton propagates without loss or change in the wave shape. If the pulse compression of an NLTL perfectly cancels the dispersion for a given pulse shape and frequency, a soliton can propagate, as shown by Figure 2.1. Some NLTL designs, especially optical designs, are based on this concept.

Solitons have numerous applications, but the communications applications are most notable [18]. Device interconnects at the board level and larger are commonly limited in data rate by frequency dispersion of square pulses. This dispersion limits the minimum rise time and the resulting broadening of pulse eventually causes inter-symbol interference if the data rate is pushed too high. A reduced dispersion NLTL can thus be used to enable device interconnects with higher data rates than traditional microstrip or stripline transmission lines [19].

Ref	NLTL Type	Compression %	Study Type	notes
[20]	Lumped Element Nonlinear Capacitor	80%	Simulated and Fabricated	-
[21]	Lumped Element Nonlinear Capacitor	82%	Fabricated	Nonlinear ferroelectric capacitors
[1]	Nonlinear parallel plate waveguide	92%	Fabricated	BST based nonlinearity
[22]	Ferrite shock line	98%	Simulated and Fabricated	Uses axial magnetic bias

Table 2.1: Summary of prior NLTL design results

Most NLTL designs can be placed in one of three categories: lumped element transmission lines, ferrite shock lines, and nonlinear optical systems. Each of these categories are discussed in the following sections. Table 2.1 summarizes the performance of several NLTL designs.

2.1.1 Lumped Element Designs

One method of NLTL design takes advantage of either the nonlinear capacitance (C) vs. voltage (V) curve or the nonlinear inductance (L) vs. current (I) curve of discrete specialized capacitors or inductors respectively [23, 24]. Of particular interest is the nonlinear $C - V$ curve of the depletion region capacitance of a reverse bias diode [25–28]. As the depletion region expands with increasing reverse bias (V) (limited by carrier mobility and relaxation), the capacitance formed by the depletion interface planes will decrease as given by (2.2) and (2.3), where A is the diode cross-sectional area.

$$C(V) = \frac{\varepsilon_0 \varepsilon_r A}{d(V)} \tag{2.2}$$

$$d(V) \propto \frac{1}{V} \tag{2.3}$$

A network can be formed using these nonlinear capacitors in combination with the inherent inductance of a microstrip transmission line, as shown in Figure 2.2. This ladder network design has a phase velocity (v_p) inversely proportional to the capacitance of each

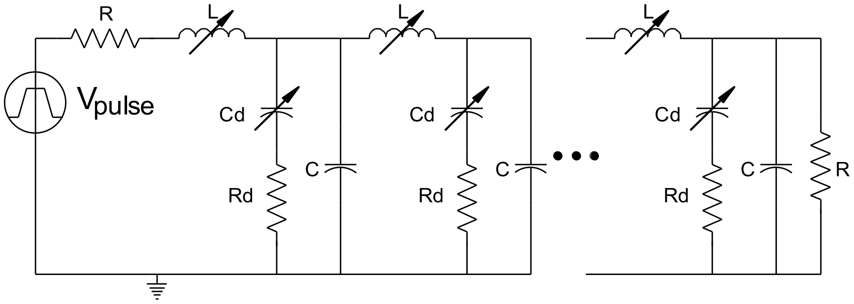

Figure 2.2: Lumped element ladder network NLTL

section, as given by (2.4). Thus the frequency components of the portion of the pulse having the largest amplitude propagate fastest (typically near the transients center). This results in the central region of the pulse, near the peak, eventually superimposing on the front edge, causing the front edge to appear spatially compressed with increased magnitude. Compression is limited for any given design by the maximum change of the nonlinear elements (ΔC) with reverse bias, the impedance matching of each stage to the next and the overall impedance matching of the NLTL to the source and load impedance.

$$v_p = \frac{1}{\sqrt{C(V)L(I)}} \tag{2.4}$$

The design choices for the capacitors and inductors (or transmission line lengths) for maximum compression is a non-trivial process; however Afshari and Hajimiri [20] demonstrated greater compression can be achieved by gradually scaling the design parameters along the line length. A simulated and fabricated metal oxide semiconductor (MOS) varactor based NLTL achieved 80% rise time compression.

Wilson, Turner and Smith [21] demonstrated a lumped element NLTL using nonlinear ferroelectric filled capacitors (general ferroelectric properties are discussed in Section 2.3). Experimental results for a 15 section network yielded 82% rise time compression. Zhao et al. [29], recently developed simulation models that show good agreement with the fabricated experiments using ferroelectric capacitors. Related to the prior work [21], Branch and Smith

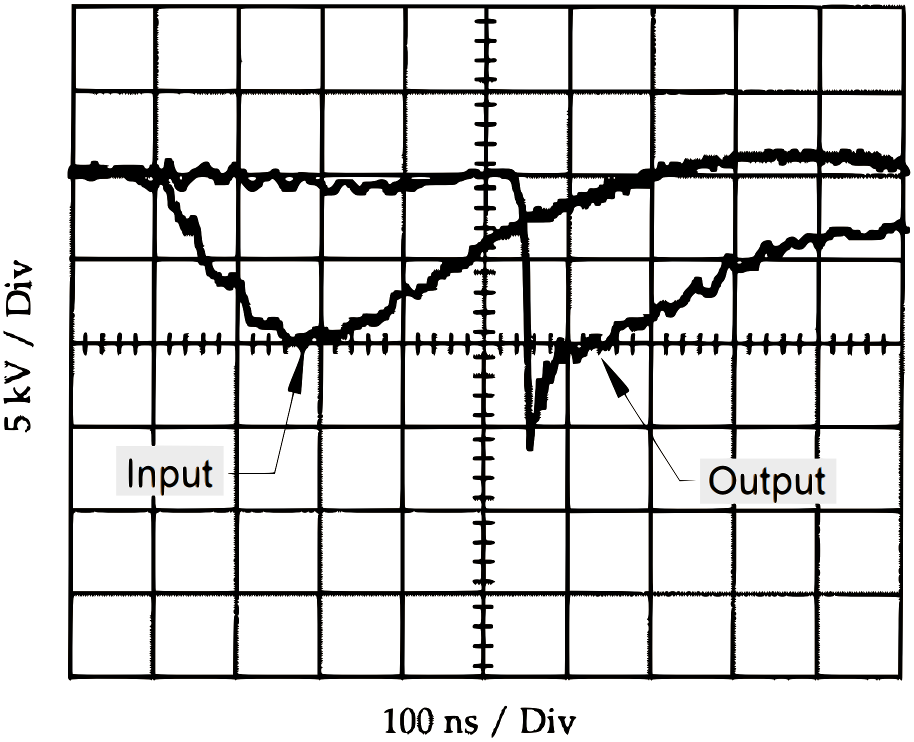

Figure 2.3: Input and output voltages for the BST filled parallel plate waveguide of Branch and Smith [1]

[1], fabricated and tested a NLTL using a parallel plate waveguide filled with BST, which achieved at least 92% rise time compression, as shown in Figure 2.3. The challenge of creating a matched load for the low impedance BST ($\sim 1-2\ \Omega$) was met by terminating the parallel plates into a copper sulfate solution, as shown by Figure 2.4. While the performance of this NLTL design is remarkable, the implementation is impractical.

While most designs have used either nonlinear inductors or capacitors, Bostick, Nardi and Zucker [30] have shown that hybrid lines with both nonlinear capacitors and nonlinear inductors have greater energy storage potential. In 2012, Kuek, Liew, Schamiloglu, and Rossi [31] examined the use of such a hybrid NLTL for the generation of microwave pulses. When the nonlinear elements were scaled exponentially, simulations demonstrated better matching to 50 Ω resistive loads and higher amplitude output in comparison to designs using only one type of nonlinear element.

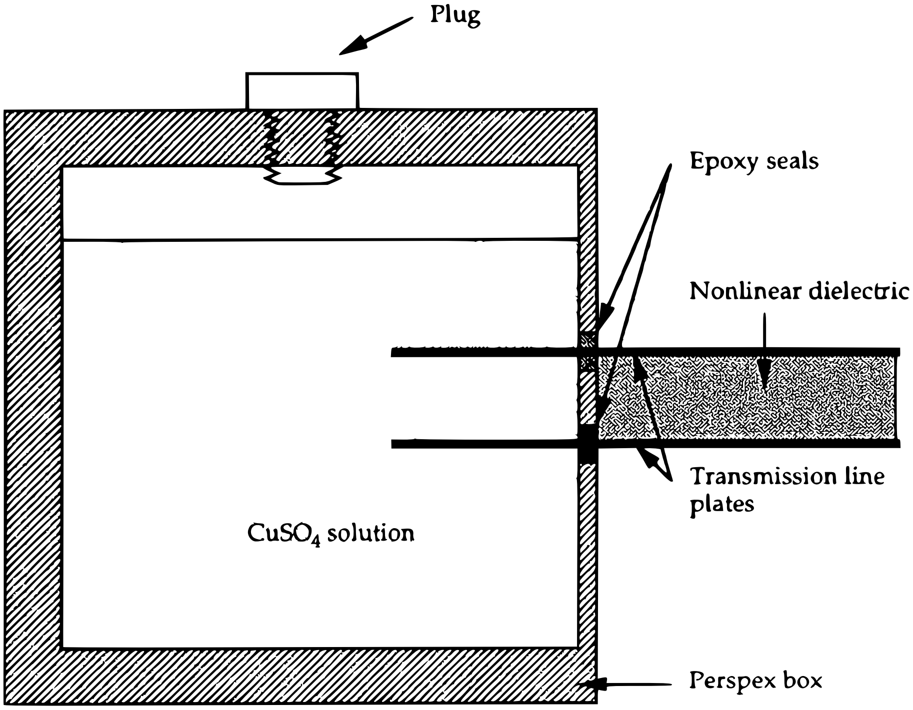

Figure 2.4: Termination resistor used by Branch and Smith [1] for BST filled parallel pate waveguide

2.1.2 Ferrite Shock Lines

Another NLTL design takes advantage of the nonlinear magnetization (**B**) vs. magnetic Field (**H**) relationship of ferromagnetic materials. For these materials in the linear region (small magnetic field values), the slope of the (**B**) vs. (**H**) curve represents the magnetic permeability (μ) as given by (2.5). For stronger magnetic fields, the magnetization asymptotically approaches a near constant saturation value, proportional only to the free space magnetic permeability μ_0. The permeability for ferromagnetic materials smoothly changes from the weak field value of $\mu_{\mathbf{H}=0}$ to μ_0 with increasing applied field, as shown in Figure 2.5. Given the propagation velocity of a wave through any medium as shown in (2.6) [32], in a ferromagnetic material this velocity is nonlinear, as shown in (2.7). Thus portions of the pulse with higher amplitude will "catch-up" and "pile-up" on the portions with smaller amplitude, resulting in a shock wave effect [33].

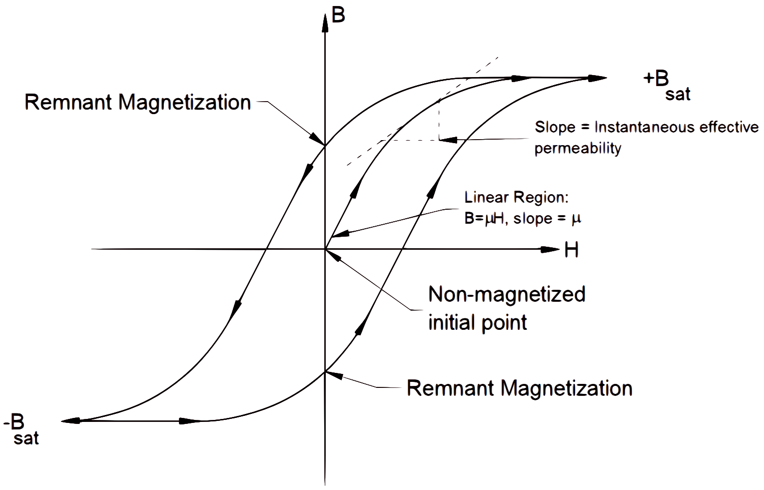

Figure 2.5: Magnetic flux density vs. applied magnetic field, sinusoidal excitation

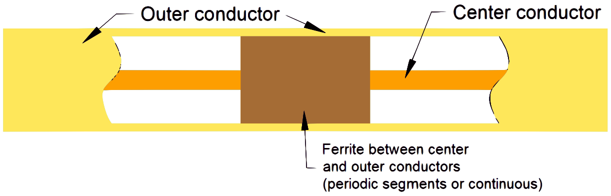

Figure 2.6: Coaxial ferrite shock line

$$\mathbf{B} = \mu\mathbf{H} \tag{2.5}$$

$$v_p = \frac{1}{\sqrt{\varepsilon\mu}} \tag{2.6}$$

$$v_p(\mathbf{H}) = \frac{1}{\sqrt{\varepsilon\mu(\mathbf{H})}} \tag{2.7}$$

In 1999, Dolan [2] described and simulated a ferrite shock line based on coaxial line with ferrite material between the center and outer conductors, as shown in Figure 2.6. Axial magnetic bias was used to place the ferrite into the nonlinear region of the (**B**) vs. (**H**) curve prior to the firing of the an input pulse. The test setup for such a line is shown in Figure 2.7. Sanders et al. [22] built a similar ferrite line using axial bias that reduced the 35 ns rise time input pulse to a rise time of only 700 ps, for a rise time compression of 98%.

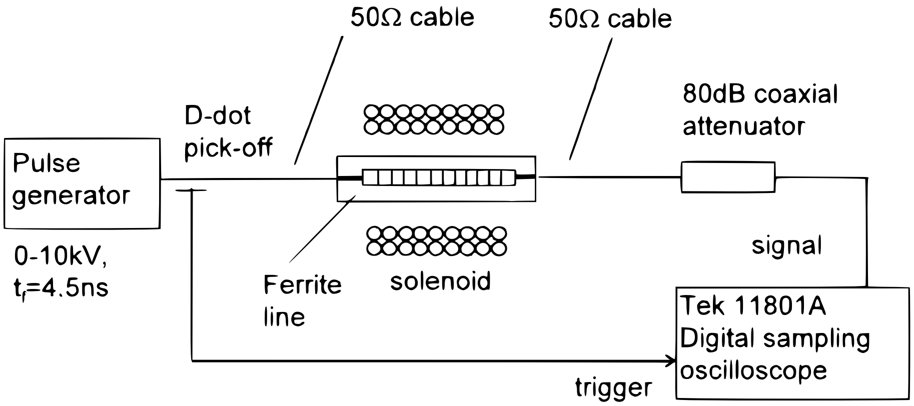

Figure 2.7: Ferrite loaded shock line with axial bias [2]

Norgard and Curry [34] presented a simulation study on an NLTL similar to ferrite shock line using ferroelectric material instead. While this work was a very preliminary study using one-dimensional modeling, the results suggest that a coaxial line loaded with ferroelectric materials would be successful for high power RF pulse generation.

2.1.3 Optics

Most nonlinear optics studies are concerned with the production and transmission of solitons. Entire textbooks are devoted to the study of optical solitons [35–37]. While nonlinear optics and NLTL's at microwave frequencies generally developed along separate research lines, it is important in the context of this work to note some key similarities. Many nonlinear fiber optic lines utilize the Kerr nonlinearity to cancel frequency dependent ('chromatic') dispersion. The Kerr nonlinearity also causes self-focusing and self-trapping of light beams, where energy collapses in both space and time [38,39]. If sufficient incident power is provided, the self-focusing effect will continue without bound until microscopic scattering, absorption, or breakdown results in the beam spitting into small high intensity filaments of light [40]. The intensity of this effect can even destroy the crystalline structure of some materials, as demonstrated by the laser ablation of sapphire due to self focusing effects of air [19].

The optical Kerr effect is based on the same polarization nonlinearity as discussed in Section 2.3 and is frequently modeled using a similar power series model. Though the effects are related, the practical materials and dependencies due to temperature, frequency, etc. are different for optical frequencies. Numerous studies [41–44] have used the FDTD method for the study of nonlinear optical systems. The resulting detailed published material of integrating nonlinear effects [45] made the FDTD method the clear choice for simulations to be done in this work.

2.2 Rectangular Waveguides

Any structure that can direct electromagnetic energy in a desired direction can be called a waveguide. In the early development of electric telegraph, simple two conductor transmission lines were used to convey electrical current from one location to another. These simple lines and other transmission lines types, such as coaxial cable, were very successful in carrying communications signals. The discovery and use of electromagnetic waves for location finding, now known as radio detection and ranging or radar, drove the need to contain and carry high power electromagnetic energy. As the military needs leading up to World War II demanded higher power radar systems, simple transmission lines became impractical in terms of power loss, power handling and unintentional coupling of signals. The solution came from using the theory and analysis of guided waves as first studied in the late 19th century [46]. Because electromagnetic waves reflect off of a metal surface with minimal loss, waves injected into a hollow metal tube will reflect between the walls and thus be carried down the tube, as shown by Figure 2.8. Exploiting this concept began with the novel use of rectangular architectural tubing to carry radio waves, but would soon become the system of rectangular waveguides that we know today [47]. The structure of rectangular waveguide along with the coordinate convention used for this work is detailed in Figure 2.9. The following sections details the theory, properties and modes of rectangular waveguides.

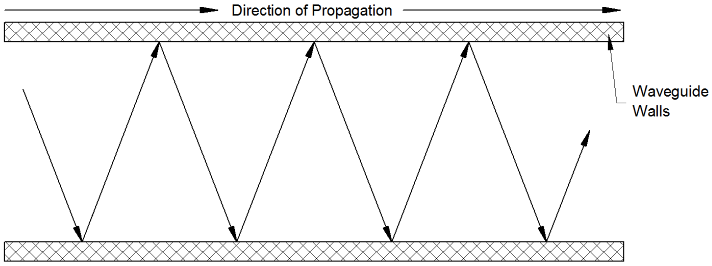

Figure 2.8: Top view of rectangular waveguide and reflecting wavefront vectors

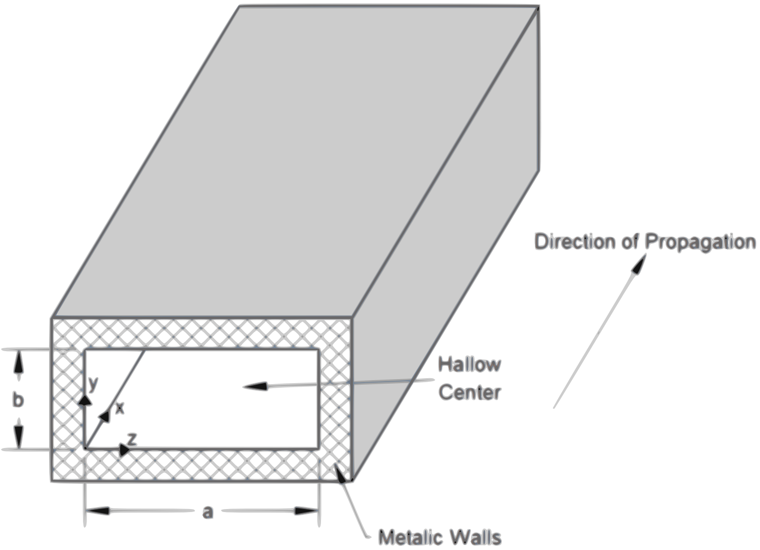

Figure 2.9: Rectangular waveguide and coordinate convention used in this work

2.2.1 Waveguide Properties and Modes of Operation

Basic Theory

In two conductor transmission lines, waves propagate with both electric and magnetic field components transverse to the direction of propagation, thus known as Transverse Electric and Magnetic (TEM) mode. The TEM mode satisfies Ampere's circuit law (2.8) as long as two conductors are present, but in a hollow waveguide, the absence of a conductor inside the guide implies the conduction current term $\mathbf{J}_c$ is zero. If closed loops of magnetic field circulate in a transverse plane (Transverse Magnetic or TM mode), as required by Gauss's law ($\nabla \cdot \mathbf{D} = 0$), then (2.8) requires that there must be electric flux $\mathbf{D}$ and thus electric field passing through that plane. Therefore the TM mode will have electric field terms in the direction of propagation. Initial enforcement of a transverse electric field and application of (2.8) demonstrates a requirement for non-transverse magnetic field, giving rise to the Transverse Electric or TE mode.

$$\oint \mathbf{H} \cdot d\mathbf{L} = \int \mathbf{J}_c \cdot d\mathbf{S} + \frac{\partial}{\partial t} \int \mathbf{D} \cdot d\mathbf{S} \tag{2.8}$$

Defining the possible fields within a rectangular waveguide begins with the enforcement of boundary conditions on Maxwell's equations for electromagnetic waves. The waveguide walls are initially assumed to be perfect conductors (conductivity $\sigma = \infty$). Applying Faraday's law and Ampere's law in integral form (enclosing the boundary between the interior of the waveguide and the walls), gives the resulting boundary conditions that the electric field tangent to the boundary (2.9) and magnetic field normal to the boundary (2.10) must be zero.

$$\mathbf{E}_{tan} = 0 \tag{2.9}$$

$$\mathbf{H}_{norm} = 0 \tag{2.10}$$

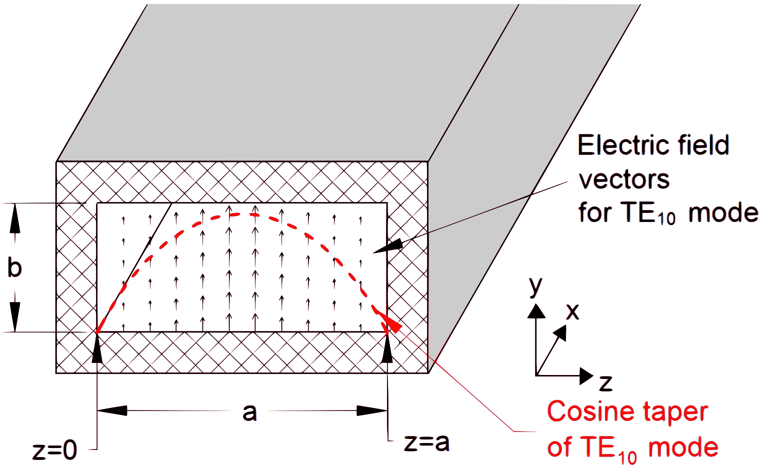

Figure 2.10: Electric field vectors for the TE_{10} mode

Modes of Operation

The simplest field distribution compliant to the boundary conditions is the n-half sinusoidal electric field distribution across the width ($\hat{z}$) of the waveguide as given by the wave number in (2.11) and the field in (2.12). The number of one-half sinusoid variations in the horizontal ($\hat{z}$) and vertical ($\hat{y}$) dimensions is used to identify the mode as TE_{nm}. The first mode, $n = 1, m = 0$, is referred to as lowest order mode, written as TE_{10} and shown in Figure 2.10.

$$k_c = \frac{n\pi}{a} \tag{2.11}$$

$$\mathbf{E}_y = E_0 \sin(k_c z) e^{-\gamma x} \tag{2.12}$$

The mode distribution gives rise to the frequency - geometry dependence of waveguides, because only electromagnetic energy with half-wavelength equal to or shorter than the waveguide width divided by n will propagate in the n_{th} mode. This maximum wavelength is known as the cutoff wavelength as given by (2.13). The phenomenon is more commonly referred to by the minimum frequency that will propagate, know as the cutoff frequency (2.14), where v_p is the intrinsic phase velocity within the waveguide.

$$\lambda_{c_{10}} = \frac{2a}{n} \tag{2.13}$$

$$f_{c_{10}} = \frac{nv_p}{2a} \tag{2.14}$$

Energy with frequencies higher than the cutoff frequency will also propagate; however at double the cutoff frequency of the first mode (TE_{10}), the next higher mode (TE_{20}) will propagate. This means energy at a frequency at or above the (TE_{20}) cutoff frequency will propagate in both (TE_{10}) and (TE_{20}). In practice, it is difficult to extract energy from a waveguide in multimode operation, so waveguides are almost always limited to single (dominant) mode (TE_{10}) operation. The waveguide height b is limited to one-half the width of the guide to insure the (TE_{10}) mode is the next higher order mode rather than the (TE_{11}) mode, thus maintaining the maximum operational bandwidth of the waveguide [32]. Further reduction of the waveguide height is possible, but results in increasing loss as discussed in Section 2.2.1.

For frequencies at or above the cutoff frequency, the wave number as given in (2.11) can be used to find the propagation constant γ, as given by (2.15), where k is the wave number of the dielectric inside the waveguide (generally air). The guided wavelength λ_g, given by (2.17), characteristic impedance Z_0, given by (2.18), and group velocity (velocity of flowing energy) v_g, given by (2.19), can all be extracted from the propagation constant. The intrinsic impedance η and intrinsic phase velocity v_p are given by (2.20) and (2.21) respectively, where μ is the magnetic permeability and ε is the dielectric permittivity of the inside of the waveguide [32, 48].

$$\gamma = j\beta = jk\sqrt{1 - \left(\frac{f_c}{f}\right)^2} \tag{2.15}$$

$$k = 2\pi f\sqrt{\varepsilon\mu} \tag{2.16}$$

$$\lambda_g = \frac{2\pi}{\beta} = \frac{\lambda}{\sqrt{1-\left(\frac{f_c}{f}\right)^2}} \tag{2.17}$$

$$Z_0 = \frac{j\omega\mu}{\gamma} = \frac{\eta}{\sqrt{1-\left(\frac{f_c}{f}\right)^2}} \tag{2.18}$$

$$v_g = \frac{\partial\omega}{\partial\beta} = \frac{1}{\sqrt{\varepsilon\mu}}\sqrt{1-\left(\frac{f_c}{f}\right)^2} \tag{2.19}$$

$$\eta = \sqrt{\frac{\mu}{\varepsilon}} \tag{2.20}$$

$$v_p = \sqrt{\frac{1}{\varepsilon\mu}} \tag{2.21}$$

The group velocity reveals two additional important properties of waveguides. First, propagating energy near the cutoff frequency moves very slowly. This logically follows as well from the model of waves bouncing between the waveguide walls, where the angle of incidence for frequencies near the cutoff frequency is nearly normal to the waveguide walls. For this reason and the subsequently discussed high conductor loss, the practical minimum frequency for waveguides is typically 125% of the cutoff frequency. Additionaly, since group velocity is a function of frequency, waveguides have an additional frequency dispersion effect, which will be discussed in detail in Section 2.2.1.

Energy injected below the lowest cutoff frequency ($f_{c_{10}}$) results in a propagation constant (2.15) that is all real, meaning such waves will be attenuated by the factor $e^{\alpha x}$. Waves in this frequency region are said to be non-propagating or in evanescent mode. While the attenuation in this mode is rapid with respect to distance from the source and generally of trivial consequence for traditional waveguide systems, it will be important to the consideration of transient propagation in Section 2.2.1.

Loss Properties

Waveguide losses are due to either dielectric losses of the material filling the waveguide (α_d) or losses caused by the finite conductivity of the waveguide walls (α_c). Dielectric losses for a dry air filled guide are negligible. If the waveguide is filled with a material other than dry air, the dielectric loss factor ε'' becomes a part of the calculation of the wave number k and leads to an wave attenuation term of $e^{-\alpha_d x}$ on each component of the fields, as given by (2.22), where f is the operational frequency and η is the intrinsic impedance. For many materials, the loss factor is stated as the loss tangent (2.23) for a specified frequency, where ω is the frequency of interest, ε' is the real part of the permittivity and σ is the conductivity of the material filling the interior of the waveguide.

$$\alpha_d = \frac{2\pi f \varepsilon''}{2}\eta\sqrt{1-\left(\frac{f_c}{f}\right)^2} \tag{2.22}$$

$$\tan\delta = \frac{\omega\varepsilon'' + \sigma}{\omega\varepsilon'} \tag{2.23}$$

In the strictest sense, assuming imperfect conducting walls slightly changes the boundary conditions that are used in initial waveguide analysis and therefore results in a slightly different propagating field. The amount of change is relatively small, which allows the loss to be calculated using perturbational methods outlined in [32]. The process can be viewed as the summation of conductor loss around the four waveguide walls, as caused by currents induced from magnetic fields tangent to those walls. The conductivity of the waveguide walls must be defined by the skin effect resistance, as given by (2.25), where the permeability μ and conductive σ are properties of the waveguide wall material. This equation also assumes sufficiently thick waveguide walls, such that attenuation through the walls is greater than 99%.

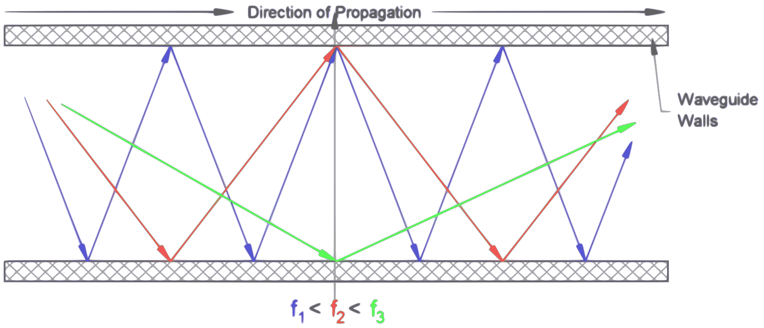

Figure 2.11: Top view of wave fronts at three frequencies

$$\alpha_c = \frac{R_s}{b\eta\sqrt{1-\left(\frac{f_c}{f}\right)^2}}\left[1+\frac{2b}{a}\left(\frac{f_c}{f}\right)^2\right] \tag{2.24}$$

$$R_s = \sqrt{\frac{\pi f \mu}{\sigma}} \tag{2.25}$$

The frequency dependence that appears outside of the skin effect resistance term can be viewed by considering the reflection based waveguide model. Energy near the cutoff frequency will reflect off the waveguide walls many more times per unit length of propagation than energy significantly above cutoff, as depicted by Figure 2.11. Each reflection contributes to the overall conductor loss. It is also important to note the conductor loss factor contains an inversely proportional dependency on the waveguide height (b). If the waveguide height is reduced from the upper limit as discussed in Section 2.2.1, conductor loss will always increase.

Transient Propagation

The goal of this work warrants an examination of transient propagation in standard rectangular waveguide. Though waveguide development and use was significant during World War II, scientific investigation of the transient response did not occur until the mid 1950's [49]. Combining an impulse with quasi-infinite frequency content or relatively content bounded trapezoidal pulse [50] with a frequency dependent propagation constant will clearly result in distortion, but the exact output from such a pulse is not readily obvious. Various analysis [3, 51–53] have sought to find more accurate and general analytical models of the transient response. While a complete restatement of those finding will not be presented here, the transient response effects can be summarized by combining concepts of multi-mode operation, group delay, and precursor waves.

Any injected waveform with frequency content outside of the $f_{c_{10}}$ to $f_{c_{20}}$ range will excite waves in multiple modes. This includes evanescent modes near the source, although the impedance mismatch (Z_0 for the waveguide is largely imaginary for $f < f_{c_{10}}$) will result in significant reflection back into the input transmission line. Since the rate of decay (α) is proportionately related to $\Delta f = f_{c10} - f$, the evanescent mode energy near the lowest cutoff frequency will decay slower with distance than energy far from the cutoff frequency. When considering the higher order modes, if a TE_{10} mode receiving probe is used (see Section 2.2.2), the probe location will be at a null for even-order modes and these modes will not be extracted from the guide.

Dividing the length of the waveguide by the group velocity (2.19) gives the time that energy of a specific frequency will take to reach the end of the waveguide. Comparing this time for two different frequencies gives a group delay. For waveforms with frequency sidebands (a commonly occurrence), severe distortion will occur if the the group delay between sidebands is a multiple of $\pi/2$ radians [49]. The group delay effect explains the behavior of the step response shown in Figure 2.12 [3]. The energy with the highest frequency travels the fastest and arrives at the receiver first. As time elapses, progressively lower frequency energy arrives at the receiver. The frequency of arriving energy will asymptotically decay towards $f_{c_{10}}$, as the frequency content closest to cutoff propagates the slowest. The amplitude will also decay, both due to decreased source spectral energy with decreasing frequency and increasing conductor losses close to $f_{c_{10}}$.

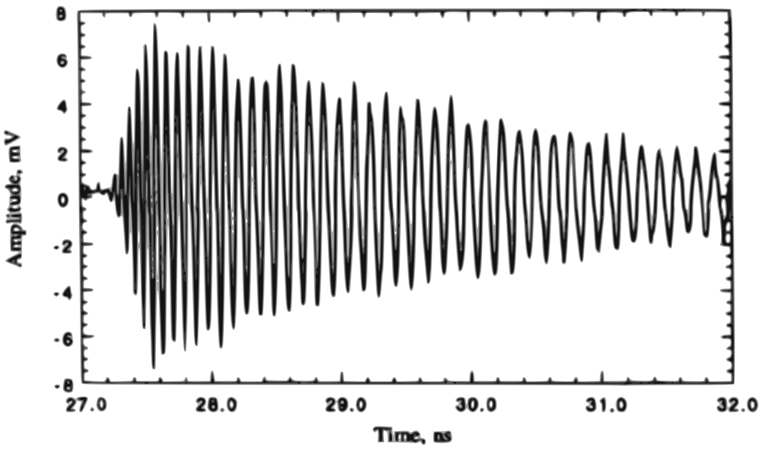

Figure 2.12: Step response of WR90 waveguide to a 40 ps rise yime step [3]

In 1914, Sommerfeld and Brillouin analytically predicted the presence of precursor waves in the transient response of dispersive media. These precursor waves result from high frequency content at the initial rise of a transient, which propagates at the intrinsic (dispersionless) velocity. While these waves are small, they appear (in time) before arrival of the main transient signal. In 1969, Pleshko and Palócz [51] confirmed the existence of precursor waves due to a transient excitation of an air-filled waveguide.

2.2.2 Feed Structures

Since most transmitters and receivers have either coaxial cable connections or at a board level, microstrip, stripline, or coplanar waveguide connections, feed structures must be used to insert and retrieve energy from a rectangular waveguide. Exciting a propagating wave within a waveguide requires careful design of the feed structure to insure a good impedance match and location match with peak fields. Both of these properties are required for maximum power transfer [54].

Broadwall Probes

The simplest and most common method of feeding a waveguide is the half-height probe. A small hole is drilled in the center of the broad wall of the waveguide, one-fourth of a

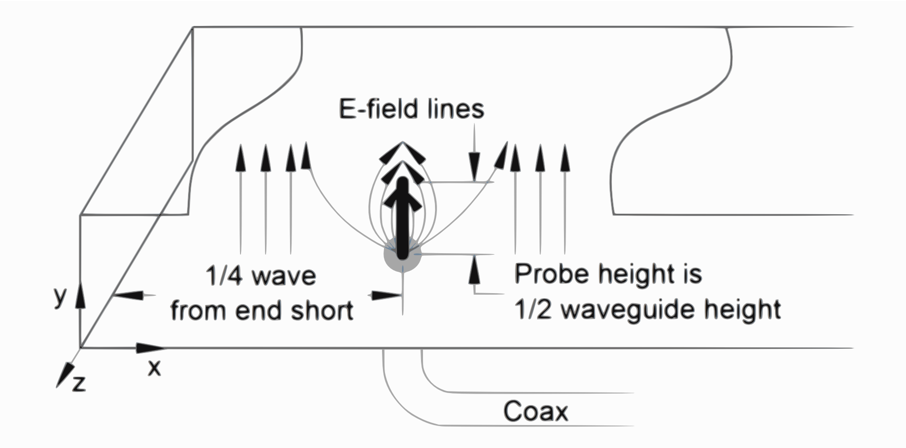

Figure 2.13: Electric field probe

wavelength from an end shorting plate. The hole is approximately the same diameter as the outer diameter of the coax or connector dielectric. A probe of length equal to one-half the guide height is connected to the center conductor of the feeding coax and the coax shell is connected to the waveguide wall. The probe acts like a short monopole antenna within the waveguide. The potential driven between the probe and the waveguide wall causes an electric field from the base to tip of the probe, which with changing current will launch a wave moving away from the probe, as shown in Figure 2.13.

Changing the height of the probe or adding a small metal plate to the top of the probe ("Top Hat") can be used to change the input impedance of the probe in order to achieve a match with the feeding transmission line. This concept has even been applied to substrate integrated waveguides as outlined in [5].

End Loops

The loop method of excitation works by forming an induction loop near the end short of the waveguide. The center conductor of a coaxial cable enters the end shorting plate through a small hole, is formed into a loop, and shorted back to the waveguide wall. Injecting a current into the loop induces magnetic field loops that will expand to fill the guide and propagate away from the source, as shown in Figure 2.14.

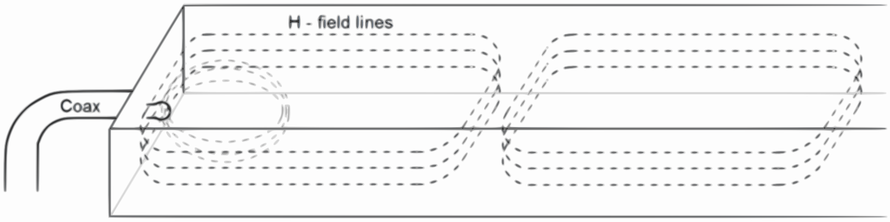

Figure 2.14: Magnetic loop or H-field probe

Aperture Excitation

Aperture excitation methods are based on waves of electromagnetic energy entering a waveguide through a removed portion of the waveguide wall. In the simplest sense, aperture excitation is using a waveguide as an antenna. Both open ended waveguides (without a horn) and guides with slots cut in the broad wall have been used extensively, although the impedance match created by the end iris shape or slot shape tends to be narrowband. As an example, space fed phased array radars use aperture excitation where a single transmit antenna radiates onto an array of waveguide-based phase shifters. While a horn antenna can excite the entire waveguide operating band much more effectively than a simple slot or iris; it is much larger than the waveguide itself and thus is spatially inefficient.

2.2.3 Substrate Integrated Waveguides

Substrate Integrated Waveguides (SIWs) began with the effort to apply the advantages of rectangular waveguide as a transmission line, namely low loss, high isolation and high power handling, to integrated RF circuitry. Most current designs build upon the theory a forming a waveguide with printed circuit board ground planes and tightly spaced vias forming end walls and side walls respectively. This configuration is shown in Figure 2.15. Both simulations and testing of fabricated structures have shown that the effective width

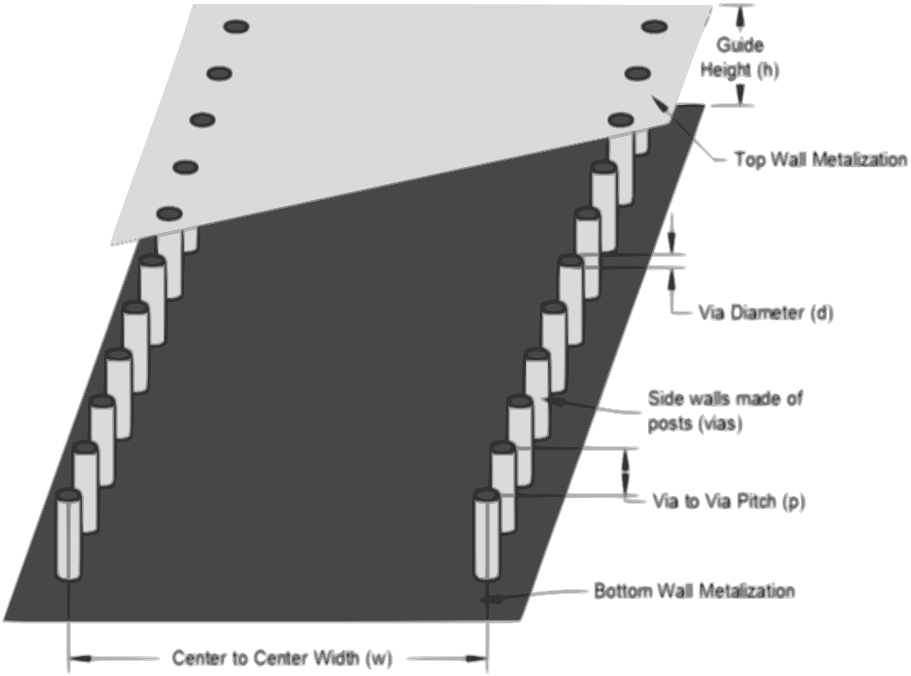

Figure 2.15: Standard substrate integrated waveguide structure and dimension conventions

of the waveguide for purposes of calculating cutoff frequency is slightly different than the distance separating the rows of posts and is given by (2.26) [55].

$$w_{eff} = w - 1.08\frac{d^2}{p} + 0.1\frac{d^2}{w} \tag{2.26}$$

Design Rules

Achieving the desired cutoff frequency with minimal loss requires careful design. Extensive simulation and analysis by Deslandes [4] has produced a set of normalized leakage loss curves (Figure 2.16) and an acceptable operating region (Figure 2.17) based on via (post) pitch and diameter. For a given cutoff wavelength, if the pitch between posts is too large, excessive leakage loss occurs. While ultimately dependent on the operating frequency and selection of conductor, if the leakage loss is constrained as given by (2.28), it will be negligible in comparison to the conductor and dielectric losses. Additionally, the pitch is constrained to be less that $\lambda_c/4$ to prevent bandgap resonances/filtering from occurring, as given by

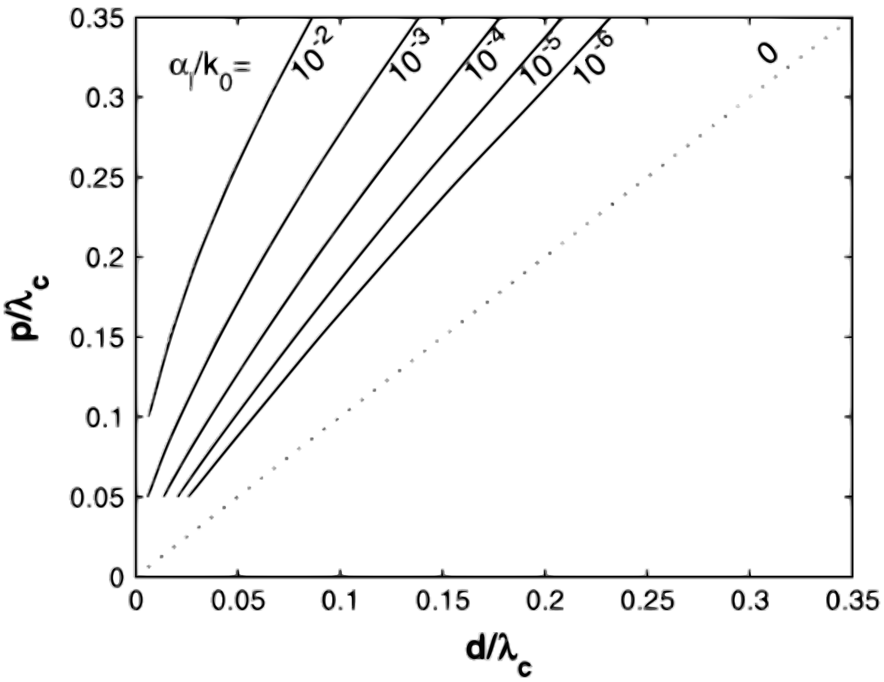

Figure 2.16: Leakage loss characteristics of substrate integrated waveguides [4]

(2.27). Since the posts reduce the strength of the substrate, a limit must be placed on the minimum pitch to ensure substrate integrity, as given by (2.29).

$$\frac{p}{\lambda_c} < 0.25 \tag{2.27}$$

$$\frac{\alpha_l}{k_0} < 1 \times 10^{-4} \tag{2.28}$$

$$\frac{p}{\lambda_c} > 0.05 \tag{2.29}$$

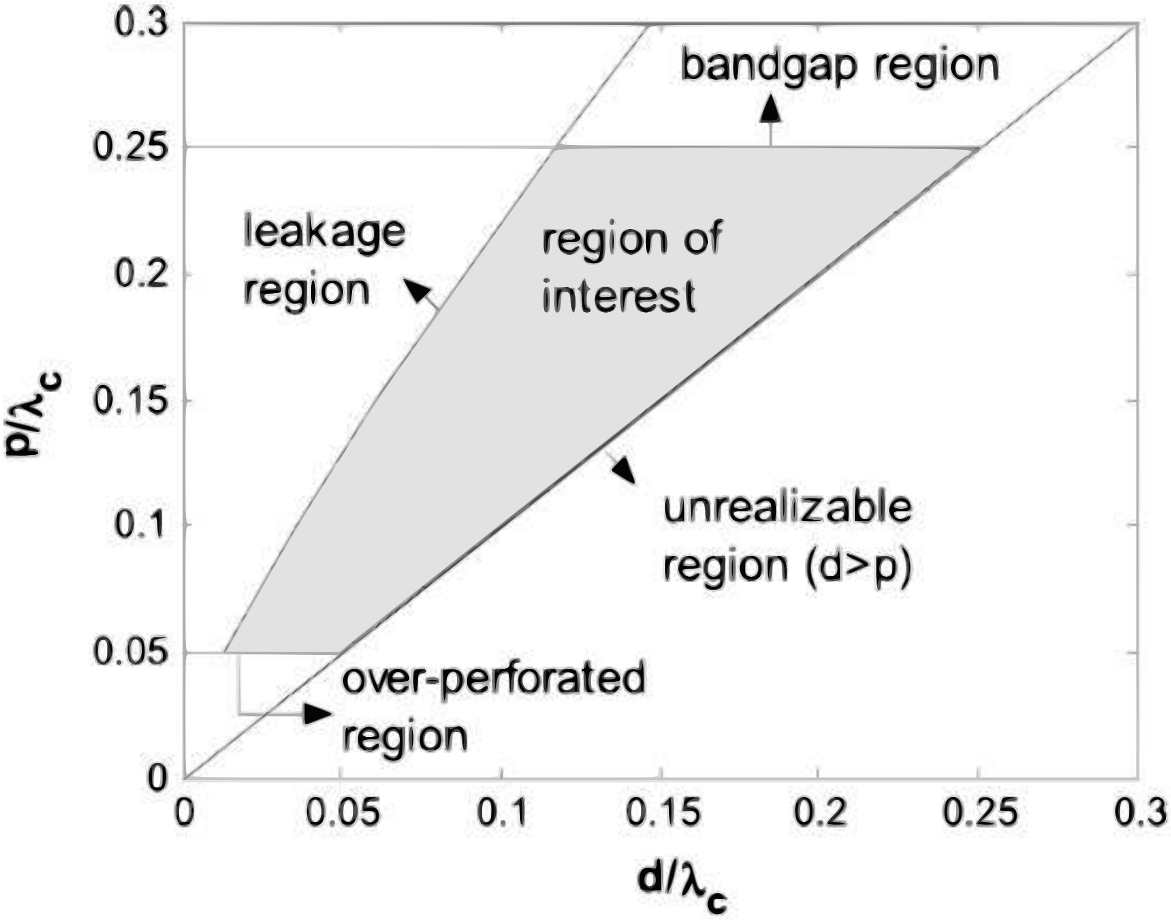

Figure 2.17: Acceptable operating region for substrate integrated waveguides [4]

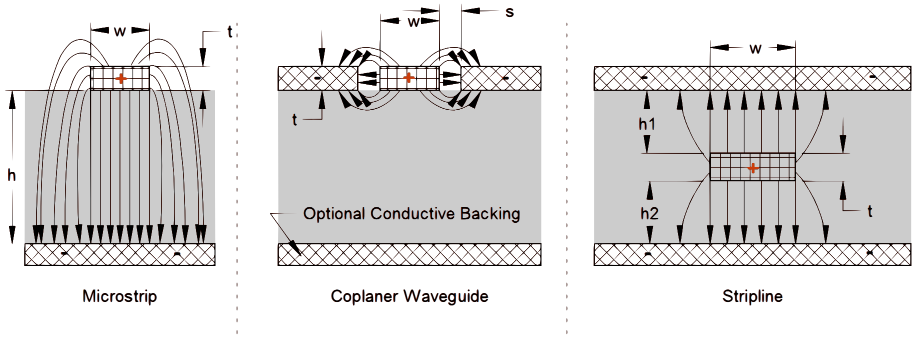

Figure 2.18: Common transmission line technologies and E-field distributions

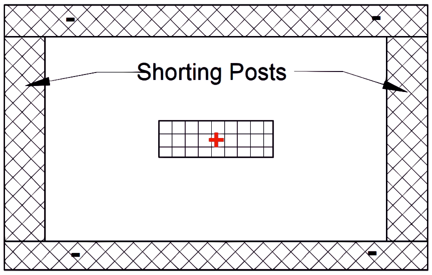

Figure 2.19: Stripline with shorting posts for isolation

Advantages

The transmission of radio frequency and microwave signals at the circuit board level has historically been dominated by TEM or quasi-TEM transmission lines, including microstrip, stripline and coplanar waveguide technologies. The geometry of each of these technologies is reviewed in Figure 2.18. SIWs offer distinct advantages over each of these technologies. Microstrip lines concentrate fields in a narrow portion of the substrate beneath the strip, but a portion of the fields do extend into the air above the strip and outward into the substrate. These uncontained fields can cause crosstalk between adjacent lines (both vertically and horizontally) if strict limits on the density of lines are not maintained. Properly designed SIWs can be placed immediately adjacent to one another, even allowing multiple SIWs stacked on different board layers. The density limit for SIWs is essentially only a function of frequency and the constitutive parameters (permittivity and permeability) of the material filling the waveguide, since this dictates the waveguide width.

Coplanar Waveguide (CPW) is simple from a design perspective, but it suffers similar issues to microstrip in terms of uncontained fields and possible parasitic coupling. The close proximity of the signal trace and ground planes results in higher local electric fields than any of the other designs, including SIWs.

Stripline designs offer better isolation than microstrip due to the upper and lower conducting planes. To achieve better horizontal isolation between adjacent lines requires the use of shorting posts between the two ground planes, as shown in Figure 2.19. Such a design differs from SIWs only by the added center conductor, making the stripline design more complex and costly to fabricate than a SIW.

Feed Structures

As with standard waveguides, special feed structure designs are necessary to achieve maximum power transfer in and out of the SIW. Three recently developed feed structures are outlined below:

Yang et al. [5] designed a microstrip to E-probe feed similar to the standard probe feed. The thin nature of SIW's ($height \ll width/2$) means a simple probe will be a small fraction of a wavelength ($< 0.1\lambda$) and thus relatively inefficient due to poor impedance matching. The addition of a stripline tuning pad greatly improves this problem by reactively loading of the probe to create a better impedance match. While the design offers DC isolation from the input microstrip to the SIW, fabrication is complex and the performance tends to be narrowband with return loss of $\leq -15dB$ only over a 10% bandwidth.

Building on the work of Chen and Wu [56], Taringou and Dornemann [6] have recently designed CPW to SIW transition without a backing conductor under the CPW. The design achieved impedance matching between the CPW and the SIW by a tapered line-to-ground gap and tapered via pattern as shown in Figure 2.21. A simulated K-band SIW using this transition for input and output achieved a return loss of less than $-20dB$ over the entire band. While this design is simple to fabricate, the inherent very high localized electric

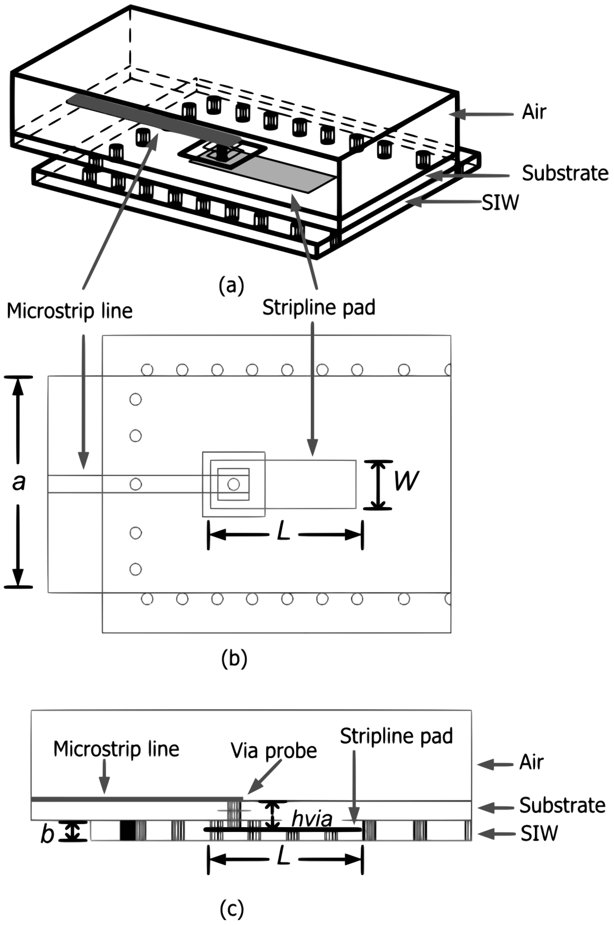

Figure 2.20: SIW probe feed with stripline tuning pad [5]

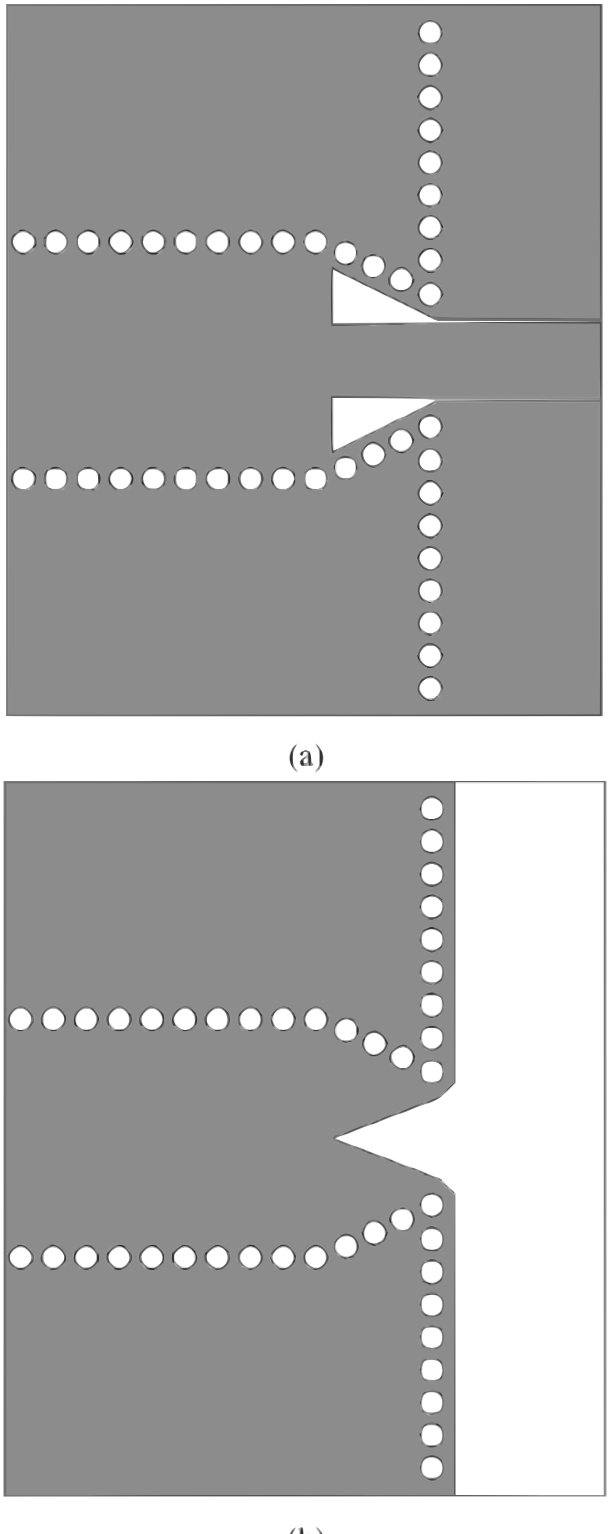

Figure 2.21: CPW to SIW transition [6]

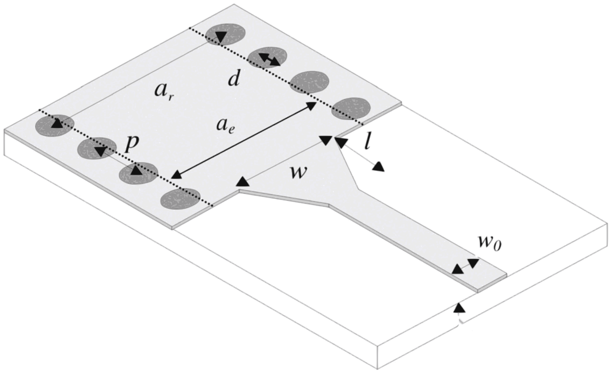

Figure 2.22: Microstrip to SIW transition [7]

fields of CPW mean that the total power handling capability will be limited by the CPW, eliminating a key advantage of SIWs.

Deslandes [7] also utilized a tapered structure to create a microstrip to SIW transition, as shown in Figure 2.22. The design builds on an empirical mode matching (for the dominant TE_{10} mode) developed by Kompa [57] to find the optimum width of the the taper to SIW junction (w). The taper length required to create the impedance match is found using the analysis of Lu [58] and corresponds to odd multiples of $\lambda/4$. A simulated and fabricated design using these transition on Duroid board with a 1 cm SIW achieved a return loss of less than $-18dB$ over the entire TE_{10} bandwidth (24-38 GHz).

Additional Considerations

The typical size restriction on coplanar integrated components has limited the use of SIWs to millimeter wavelengths when these waveguides are either air filled or filled by a low permittivity ($\varepsilon < 10$) substrate. The use of high permittivity ferroelectric materials, as discussed in Section 2.3, allows the use of SIWs at much lower frequency, due to much smaller wavelengths for a given frequency. The low loss properties of Low Temperature Cofired Ceramic (LTCC) substrates at microwave and millimeter wave frequencies make them ideal candidates for fabricating SIWs [59, 60].

2.3 Ferroelectric Materials

Significant research has taken place over the last 20 years into the physics of ferroelectric materials for microwave tunable devices. While a review of the quantum mechanics analysis commonly used is beyond the scope of this work, a brief review of ferroelectric properties will be given, along with a discussion of material applications, the selected materials, and modeling methods.

2.3.1 Physical Basis

The physical basis of ferroelectric material begins with the ability of certain molecules to form an electric dipole moment. An electric dipole occurs anytime positive and negative charges separate within a system (molecule). These dipoles can be fixed with the lattice of a material or they can be formed by an externally applied electric field. The density of charges making up the dipole will be denoted as $p(r)$. An electric dipole moment refers to the strength of the charge separation. The density of dipole moments can be represented by a vector field called the polarization density $\mathbf{P}$. For bulk materials, it is generally acceptable to consider the polarization density identical to the charge density $p(r)$ distribution. This assumption however does not consider surface states that arise at material discontinuities. For linear materials the polarization is a simple linear function of the applied electric field, as given by (2.30). The electric susceptibility χ is a measure of material's ability to be polarized.

$$\mathbf{P} = \varepsilon_0 \chi \mathbf{E} \tag{2.30}$$

The polarization verses electric field response in a ferroelectric material differs in two key ways. First, at sufficiently high electric field values the polarization begins to asymptotically approach a saturation limit (P_{sat}) . Secondly, after an electric field is applied and polarization is established, a ferroelectric material will retain some polarization when the applied electric

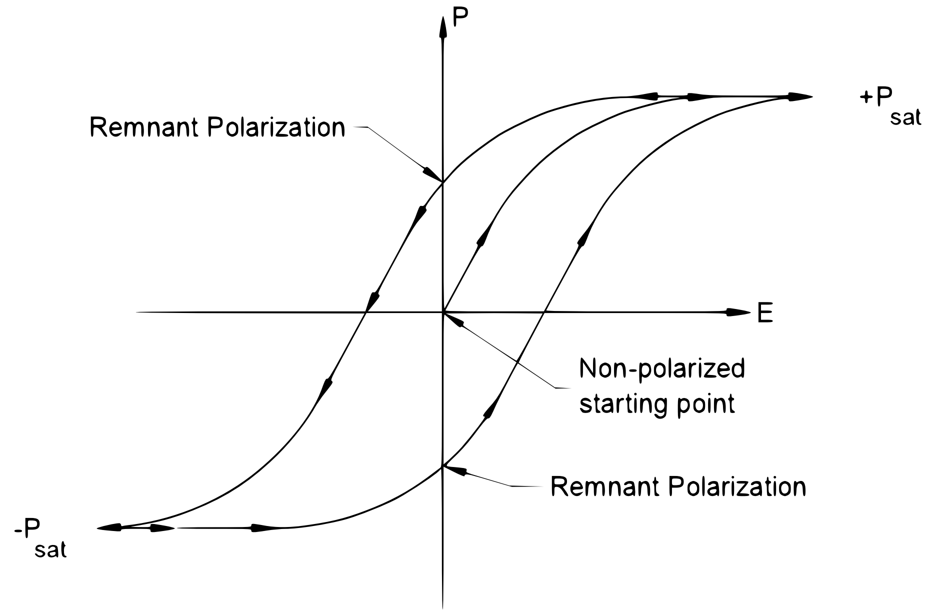

Figure 2.23: Hysteresis loop formed by polarization verses applied sinusoidal electric field

field is removed. The polarization remaining when the the electric field is reduced to zero is known as the remnant polarization. This effect is termed 'electric hysteresis' because the polarization state is dependent on the history of both the polarization state and the presently applied electric field. A sinusoidal cycle of electric field produces a hysteresis loop on a plot of **P** vs. **E**, as show in Figure 2.23.

2.3.2 Properties and Dependencies

Deriving from the case of linear materials as given by (2.30), the electric flux density is given by (2.31) where $\varepsilon_r = \chi + 1$.

$$\mathbf{D} = \varepsilon_0 \mathbf{E} + \mathbf{P} = \varepsilon_0 \varepsilon_r \mathbf{E} \tag{2.31}$$

In a plot of **D** vs. **E** from (2.31), as shown in Figure 2.24, the slope of the plot represents the relative permittivity. The slope of a plot of **P** vs. **E** will only differ from the slope of **D** vs. **E** by one. This relationship holds even when **P** is nonlinear in the case of a ferroelectric

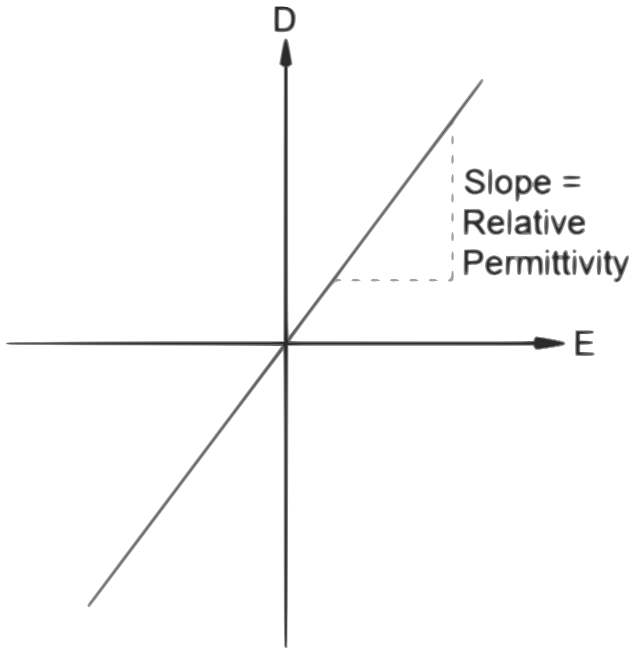

Figure 2.24: Electric flux density **D** vs. electric field **E**

material. For such materials the general relative permittivity is given as equation (2.32) as a function of the applied electric field.

$$\varepsilon_r\left(|\mathbf{E}|\right) = 1 + \frac{\partial|\mathbf{P}|}{\partial|\mathbf{E}|} \tag{2.32}$$

Thus for low values of applied electric field, the relative permittivity will be at a maximum. As the material approaches polarization saturation, the relative permittivity will asymptotically approach one. Many ferroelectric materials have very large values of low field relative permittivity $\varepsilon_r > 100$, with large variability between materials, reaching upwards of $\varepsilon_r = 10,000$ for polarizable polymers [61].

The tunable capacitor application as discussed in Section 2.3.4 gives rise to the 'tunability' (n) or more common 'relative tunability'(n_r) figures of merit for ferroelectric materials as given by (2.33) and (2.34). E_0 is a quoted value of bias field placing the material in the nonlinear polarization region.

$$n = \frac{\varepsilon\left(E_0\right)}{\varepsilon\left(0\right)} \tag{2.33}$$

$$n_r = \frac{\varepsilon\left(0\right) - \varepsilon\left(E_0\right)}{\varepsilon\left(0\right)} \tag{2.34}$$

Temperature Dependence

Many ferroelectric materials exhibit one or more phase transition temperature points. Many materials have an electric Curie point transition above which the remnant polarization is zero and no hysteresis loop is formed. Materials in this state are known as paraelectric or are said to be in paraelectric phase.

The behavior of some materials can be described by the electric form of the Curie-Weiss law as given by equation (2.35), where C_c is the material-dependent Curie constant, T is the absolute temperature in kelvin and T_0 is the Curie-Weiss temperature.

$$\varepsilon = \varepsilon_r \varepsilon_0 = \varepsilon_0 + \frac{C_c}{\left|T - T_0\right|} \tag{2.35}$$

In these materials, the relative permittivity is a maximum at the Curie-Weiss temperature, although the Curie-Weiss law fails due to the singularity very near $T = T_0$. More advanced models such as the Landau theory must be used at these temperatures [62].

Ferroelectric materials often exhibit combinations of effects, not only as functions of temperature, but also as function of lattice stress (piezoelectric effect), fabrication sintering temperature (often due to lattice imperfections), and dopants. Not all of these effects are well understood. The selection of ferroelectric materials for any given application often involves a set of complex trade offs [62]. In many cases materials with higher values of low field permittivity and higher tunability have high dielectric loss and greater temperature dependence of properties [63]. This work will concentrate on the use of Barium Strontium Titanate (BST) with the known properties and considerations outlined in Section 2.3.5.

2.3.3 Loss Mechanisms

The general intrinsic loss mechanism within ferroelectric materials involves complex collisions of the electromagnetic fields (and the associated contained energy) and thermal phonons. The exact mechanisms are combinations of multiple quantum phenomena as outlined in [62]. Extrinsic losses, such as those caused by the motion of charge inpurites and lattice defects, can also be significant. Losses are most commonly stated as either a dielectric dissipation (often as a function of frequency) (2.36) or as the loss tangent at a given frequency (2.37).

$$\varepsilon_r = \varepsilon^{'} - j\varepsilon^{''} \tag{2.36}$$

$$\tan\delta = \frac{\sigma + \omega\varepsilon^{''}}{\omega\varepsilon^{'}} \tag{2.37}$$

2.3.4 Applications

The ability to control relative permittivity of ferroelectric material by an externally applied electric field gave rise to their use for tunable microwave components. In the simplest case, a DC voltage applied across a parallel plate capacitor filled with a ferroelectric material will produce a variable small-signal AC capacitance as shown by (2.38), where A is the area of the capacitor and d is the parallel plate separation distance. Since ferroelectric materials have a large values of relative permittivity, much larger values of capacitance can be formed with microfabrication components than is possible with only a silicon substrate.

$$C(V) = \frac{\varepsilon_0\varepsilon_r(V)A}{d} \tag{2.38}$$

Ferroelectric materials can be used in place of standard dielectric in microwave components to form tunable components from designs that would normally be narrow band. Many devices rely on variable phase velocity through a biased ferroelectric, as given by (2.39) .

$$v_p(V) = \frac{c}{\sqrt{\mu\varepsilon_0\varepsilon_r(V)}} \tag{2.39}$$

Examples that utilize this effect include: A band-pass filter based on circular ferroelectric filled resonator cavities with tunable center frequency [64], a phased array lens formed by slabs of bulk ferroelectric with biasing plates between layers [65], a phase shifter formed by a coplanar transmission lines on ferroelectric substrates, thus having a tunable electrical length and phase shift [66]. Three significant obstacles are faced with many microwave device applications: high bias field requirements ($|E| \geq 1MV/m$ typical), variable impedance mismatch for planer components on ferroelectric substrates (since $Z_0 \propto 1/(\sqrt{\varepsilon_r})$, and lattice interface matching problems with common substrates such as silicon [62].

While most applications utilized the bias controllable relative permittivity, one signification application utilizes the hysteresis effect of ferroelectric materials. The remnant polarization that can be held by a ferroelectric capacitor can be used as memory cell for the fabrication of Random Access Memory (RAM) . Ferroelectric RAM or FeRAM creates a logic '1' by driving a ferroelectric capacitor with sufficient voltage to cause a retained spontaneous polarization. The memory cell is read by applying a sufficient field (known as the coercive field) to remove the remnant polarization. If the cell held a logic '1', a detectable current pulse will be produced during the polarization removal process. No pulse is produced if the cell was a logic '0'. Unlike Dynamic RAM (DRAM), FeRAM does not require periodic refreshing since it does not depend on maintaining a capacitor voltage which decays in time. The primary disadvantage of FeRAM is the low memory density compared to DRAM. To maximize the detectable current and reliability of the memory, FeRAM designs seek materials with large hysteresis loops that are nearly square [67]. This is in contrast with most microwave ferroelectric devices which work best with minimal hysteresis.

2.3.5 Properties of Barium Strontium Titanate

Barium Strontium Titanate $Ba_xSr_{x-1}TiO_3$ is a crystalline solid with a Perovskite structure. Perovskites have a crystalline form like that calcium titanium oxide ($CaTiO_3$), a naturally occurring mineral named after mineralogist L.A. Perovski. These structures take the form ABX_3, where A and B are cations of different sizes, and X is an anion, most commonly oxygen, that bonds to both cations. The oxygen atoms are found on the face centers of the crystals. The ferroelectric effect is common to almost all Perovskite materials [68]. While Barium Titanate and Strontium Titanate have been used for their ferroelectric properties independently, the ability to combine these compounds in varying fraction allows for a blending of their properties. Because the Curie point of Barium Titanate and Strontium Titanate are so vastly different ($120°C$ vs. $-269°C$ respectively), blending the two allows for widely varying control of the composite material's Curie point, as shown in Figure 2.25 [8]. For any given BST ratio, the permittivity approximately follows the Curie-Weiss law, as shown by Figure 2.26 [9]. Wei and Yao [19] found that both the permittivity and the tunability are reduced when moving away from the Curie-Weiss temperature (BST with $x = 0.8$), as shown in Figure 2.27. For a fixed temperature, slight changes in BST ratio allows control over material tunability.

The hysteresis properties of Barium Titanate and Strontium Titanate are also different. Combining the two materials allows for control of the hysteresis loop. While hysteresis effects can never be completely eliminated, BST used at an operating temperature at or above its Curie-Weiss temperature (T_0) show a small enough hysteresis loop to be considered paraelectric. Numerous studies [69–71] have confirmed this with thin-film BST ($x = 0.5$) used at room temperature. Building on the advantage for variable BST ratio, a technique has been developed to form continuously graded BST films. Tests with tunable capacitors showed 60% tunability and much lower temperture dependance compared to uniform composition films [72].

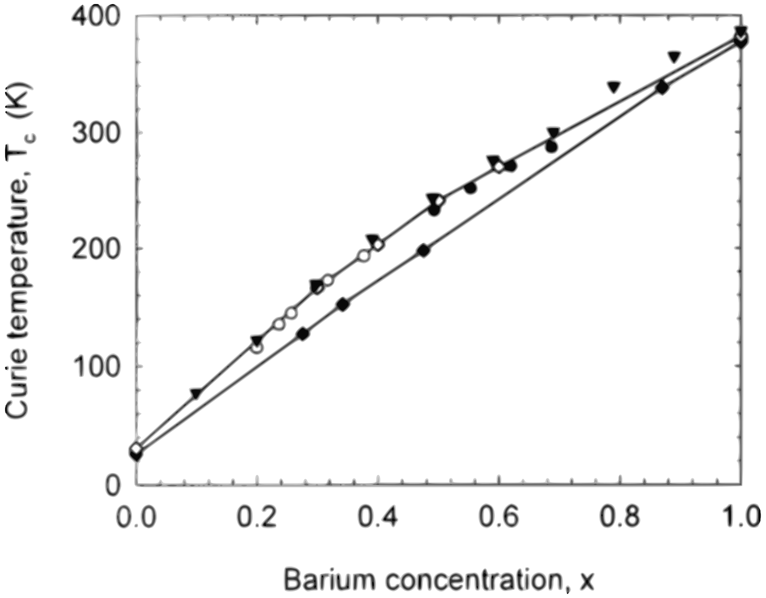

Figure 2.25: Curie point temperature vs. barium concentration [8]

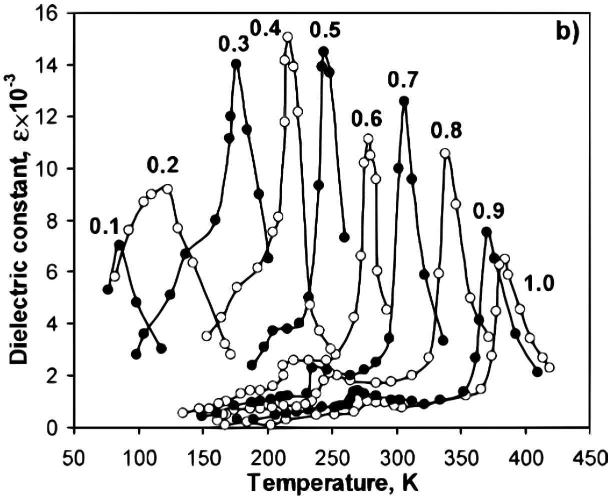

Figure 2.26: Dielectric permittivity vs. temperature for various barium-to-strontium ratios [9]

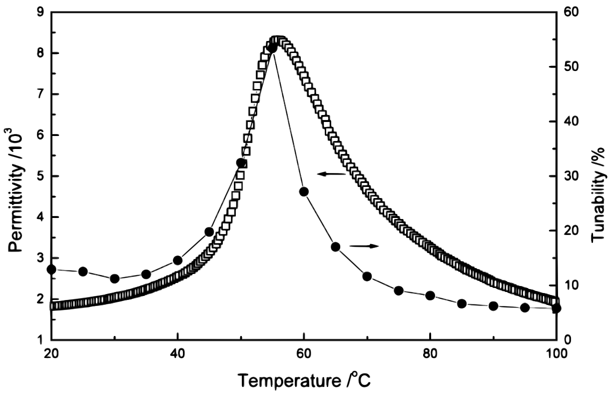

Figure 2.27: Permittivity and tunability vs. temperature for BST $x = 0.8$ [10]

While dielectric loss in BST can be attributed to the previously discussed mechanisms, the exact loss for BST in any given application is difficult to predict, due to variability as a function of BST ratio (x), layer thickness, sintering temperature, surface states, strain, etc. However, some general trends can be observed. Most loss tangent measurements of BST report values in the range $10^{-2} - 10^{-3}$, which is 1 to 2 orders of magnitude greater than the loss tangent of many polymer low-loss microwave substrates (Teflon®: $\tan\delta \sim 5 \times 10^{-4}$). High loss has been a common constraining factor from using bulk BST as tunable substrate. Thin films ($t < 5\ \mu m$) of BST have a greater loss tangent than bulk forms, but for many applications, the total loss over the film thickness is still acceptable [62]. The relatively poor loss tangent can be improved by approximately an order of magnitude with the addition of dopants such as magnesium oxide [73] or alumina [74]; however, the low-field permittivity and tunability are also reduced.

2.3.6 Modeling

Design and simulation of ferroelectric devices demands accurate and computationally efficient models of the both polarization saturation and hysteresis effects. The following discussion will present two methods of modeling the saturation effect and one common method of modeling hysteresis. In all cases the models are macroscopic in nature and assume the polarization follows the direction of the applied electric field.

Power Series

A piecewise power series expansion can represent the polarization as given by (2.40). This formulation is piecewise in that a constant value of polarization saturation is used at and above the point where an increasing electric field reaches saturation (E_{sat}). A similar situation occurs for the negative field sense. For low values of the electric field $\mathbf{E}$, the first term dominates (where the weak field permittivity is given as $\varepsilon_r = \chi_1 + 1$). Because the polarization for most materials is an odd function, the even order terms are zero. While many terms can be used, in practice, only the third order term is typically used for computational efficiency.

$$\mathbf{P} = \begin{cases} +\mathbf{P_{sat}}\frac{\mathbf{E}}{|\mathbf{E}|} & |\mathbf{E}| \geq E_{sat} \\ -\mathbf{P_{sat}}\frac{\mathbf{E}}{|\mathbf{E}|} & |\mathbf{E}| \leq E_{sat} \\ \left(\varepsilon\chi_1\mathbf{E} + \varepsilon\chi_3\mathbf{E}^3 + \cdots\right)\frac{\mathbf{E}}{|\mathbf{E}|} & Otherwise \end{cases} \tag{2.40}$$

Hyperbolic Tangent

The double asymptotic nature of polarization saturation gives rise to considering hyperbolic trigonometric functions exhibiting similar properties as polarization models. The simplest model of this type is given in the (2.41) where P_{sat} is the polarization saturation limit and E_{scale} is a scaling factor given by (2.42). ε_r is the weak field permittivity. This model works well for a relatively small tuning range; however, most materials approach polarization saturation (with increasing electric field) at a slower rate than the model predicts.

$$\mathbf{P} = P_{sat}\tanh(E_{scale}\mathbf{E})\frac{\mathbf{E}}{|\mathbf{E}|} \tag{2.41}$$

$$E_{scale} = \frac{\varepsilon_0(\varepsilon_r - 1)}{P_{sat}} \tag{2.42}$$

Vendik's Model

Vendik and Zubko [75] developed an expansion of the power series model for polarization that can be used to directly compute the effective permittivity as a function bias field and temperature. The model is given by (2.43) - (2.47), where E_0 is the bias field, T is the operating temperature, C is the Curie-Weiss constant, T_0 is the Curie-Weiss temperature, E_N is the bias field scale factor and T_V is a temperature adjustment factor.

$$\varepsilon(T, E_0) = \frac{\varepsilon_{00}}{\left[\left(\xi^2+\eta^2\right)^{1/2}+\xi\right]^{2/3}+\left[\left(\xi^2+\eta^2\right)^{1/2}-\xi\right]^{2/3}-\eta} \tag{2.43}$$

$$\varepsilon_{00} = \frac{C}{T_0} \tag{2.44}$$

$$\eta = \varepsilon_{00}\alpha\varepsilon_0 \tag{2.45}$$

$$\xi = \frac{E_0}{E_n} \tag{2.46}$$

$$\alpha = \frac{T_V}{\varepsilon_0 C}\left[\sqrt{\frac{1}{16}+\left(\frac{T}{T_V}\right)^2}-\frac{T_0}{T_V}\right] \tag{2.47}$$

Vendik and Zubko [8] subsequently developed an empirical model specific for BST as a function of the BST ratio (x), as given by (2.48) - (2.51), and the constant $T_V = 175[K]$.

$$T_0(x) = 42 + 430.37x - 95.95x^2 \tag{2.48}$$

$$C(x) = \left(0.86 + 1.1x^2\right) \times 10^5 \tag{2.49}$$

$$\varepsilon_{00}(x) = \frac{C(x)}{T_0(x)} \tag{2.50}$$

$$E_N(x) = \frac{8.4}{\left(\varepsilon_0 \left(3\varepsilon_{00}(x)\right)^{3/2}\right)} \tag{2.51}$$

Preisach Hysteron Model

Ferenc (Franz) Preisach first suggested a non-ideal relay or hysteron as a model for hysteresis. This model is defined by (2.52) where k is the output state from the prior evaluation of the input (assuming $y = 0$ at time zero). The response of the hysteron to a sinusoidal input (x) is shown in Figure 2.28

$$y = \begin{cases} 1 & x \geq \beta \\ 0 & x \leq \alpha \\ k & \alpha < x < \beta \end{cases} \tag{2.52}$$

Forming a complete hysteresis model involves evaluating many individual hysterons with different values of α and β and summing the results. An example of the hysteresis loop formed by a sinusoidal excitation is shown in Figure 2.29. Achieving a tolerable modeling error requires a fine stepping of the α and β and thus a large number of hysterons ($10^3 - 10^4$ typically). For simple systems where hysteresis can be considered a bulk effect (many tunable parallel plate capacitors for example), the computational burden of evaluating and summing thousands of hysterons is manageable. For more complex structures, such as the design presented in this work, the polarization hysteresis would have to be evaluated for each cell in the lattice. The resulting computational burden will be unmanageable for most simulations. Tsang [76] developed an adaptation of the Preisach model that can be computed without large summations, but the numerous hyperbolic functions that are used instead are also

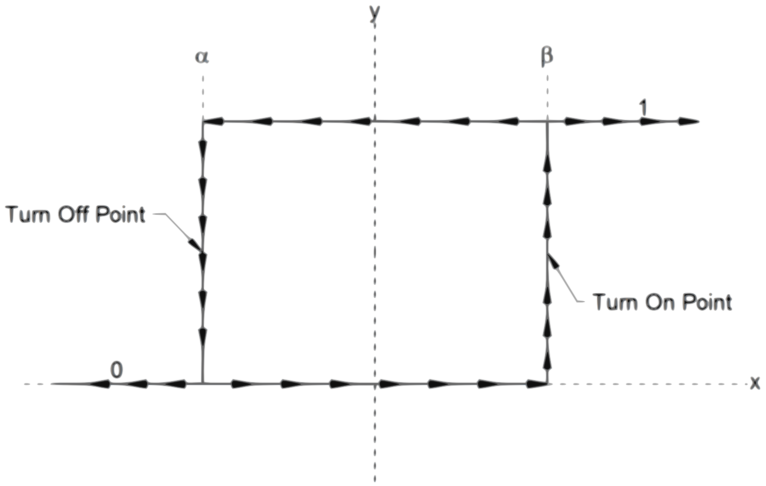

Figure 2.28: Hysteron model response to a sinusoidal input

computationally intensive. While numerous other models of hysteresis exist [77–79], all require significant additional computation for each simulation cell.

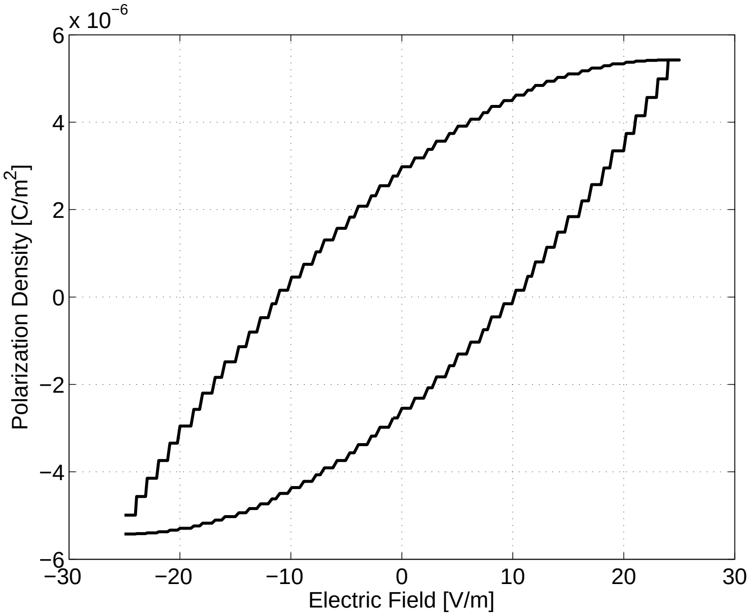

Figure 2.29: Example result of Preisach hysteresis model with 1275 hysterons

2.3.7 Characterization and Parameter Extraction

Utilizing ferroelectric materials and the previously discussed models for design and simulation requires accurate knowledge of the relative permittivity as a function of the electric field bias and the hysteresis effects. Analysis of a ferroelectric filled capacitor is the simplest form of characterization. By applying a variable DC bias (V_{DC}) across the plate and measuring the small signal AC capacitance (at a frequency of interest), the relative permittivity can be extracted by (2.53), where d is the plate separation distance, A is the plate area and the reference field $|E| = V_{DC}/d$.

$$\varepsilon_r(|E|) = \frac{Cd}{\varepsilon_0 A} \tag{2.53}$$

Hysteresis can be observed when multiple cycles of V_{DC} are plotted on ε_r vs. E, but direct extraction of the hysteresis parameters (remnant polarization and coercive field) is difficult at best. Another issue arises from maintaining a DC voltage across a capacitor with a large dissipation factor (ε_r'') (as discussed in Section 2.3.3). If the measurement is not done quickly, significant heating of the structure can significantly skew the results, especially if the measurement is in the vicinity of the Curie point.

A more complex method that allows direct extraction of the hysteresis parameters is the hysteresis bridge method. The measurement circuit, commonly known as a Sawyer and Tower circuit [80], is shown in simplified form in Figure 2.30. An arbitrary AC waveform is applied across the series combination of a ferroelectric filled capacitor (C_{DUT}) and a linear reference capacitor (C_0), thus forming a voltage divider. The voltages across the reference capacitor and test capacitor are applied to the vertical and horizontal inputs of an X-Y oscilloscope respectively. Because the retained spontaneous polarization can be represented as retained charge (and subsequently voltage), the oscilloscope will trace the hysteresis loop for a given input waveform. In practical application, some scaling (amplification) and phase

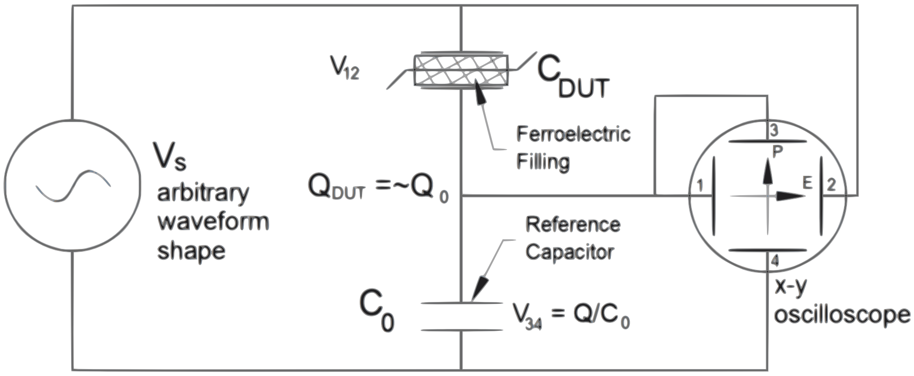

Figure 2.30: Hysteresis bridge circuit

shifting is required to form an accurate hysteresis loop [81]. Once the measurement data is obtained, curve fitting methods can be used to find model parameters.

Chapter 3

Principle Design

This work combines the prior discussed principles of substrate integrated waveguides with a new form of nonlinear transmission line based on polarization saturation in ferroelectric materials. While ferroelectric filled rectangular waveguides as a NLTLs have been suggested [24], to the best knowledge of the author, a complete practical design and simulation have never been done in prior work. The following sections outline operating principles and the design parameters that will be optimized.

3.1 Theory of Operation

In the previously discussed applications of ferroelectric materials (Section 2.3.4), phase velocity was modified using external DC bias. If a pulse or pulsed AC signal of sufficient amplitude is passed through a ferroelectric material, a portion of the material can be driven into the polarization saturation region by the pulse itself without external bias. This is identical to the basis of self-focusing nonlinear optics, as discuss in Section 2.1.3. The peak of such a pulse will result in a minimum value of ε_r and maximum phase velocity v_p. Since the leading edge of the pulse propagates slower than the peak, the peak will 'pile-up' on the leading edge causing rise time compression. This is identical to the effect of lumped element variable capacitor NLTLs, except compression is continuous over the propagation distance. Compression is only limited by dissipation, dispersion and dielectric breakdown. This concept has been tested by Branch and Smith [1] with bulk form BST in a parallel plate waveguide, as discussed in Section 2.1.1.

Initial simulations using the methods discussed in Chapter 4 compared a theoretical, BST filled WR90 sized waveguide with and without the polarization nonlinearity [82]. The

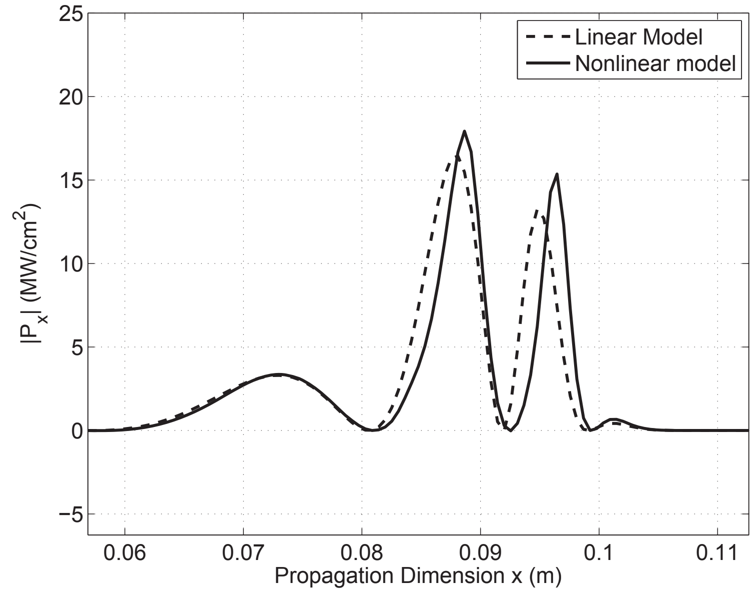

Figure 3.1: Simulation Results: $\mathbf{a}_x$ component of the Poynting vector, down the guide center

hyperbolic tangent model was used with modeling parameters taken from [83] for a BST ratio of $x = 0.24$, resulting in $\varepsilon_r(0) = 1450\, F/m$ and $P_{sat} = 74.6\, mC/m^2$. For the linear case, the relative permittivity was constant $\varepsilon_{r_{linear}} = 1450\, F/m$. Rise time compression of the injected Gaussian pulse is clearly visible in Figure 3.1. Rise time analysis, as shown in Figure 3.2, using a maximum time derivate method located a minimum 10% to 90% rise time of 251 ps, a compression (using (2.1)) of 42% from the source rise time of 433 ps.

Three conclusions were drawn from this initial study: First, the source voltage required to drive the BST into the nonlinear region within the standard waveguide with an E-probe feed is impractically large ($V \geq 10\, kV$). Secondly, given a TE_{10} mode field distribution with peak field strength in the center of the waveguide, only a small portion of the material in the center of the guide will be strongly driven into the nonlinear polarization region. Lastly, if the input pulse amplitude is large enough, the wave compresses faster than it dissipates, and power and energy density grow infinitely. Thus, the propagating wave continues to compress without bound until it is limited by discretization error based velocity dispersion inherent to the FDTD process (see Section 4.2). This 'run away' compression situation is

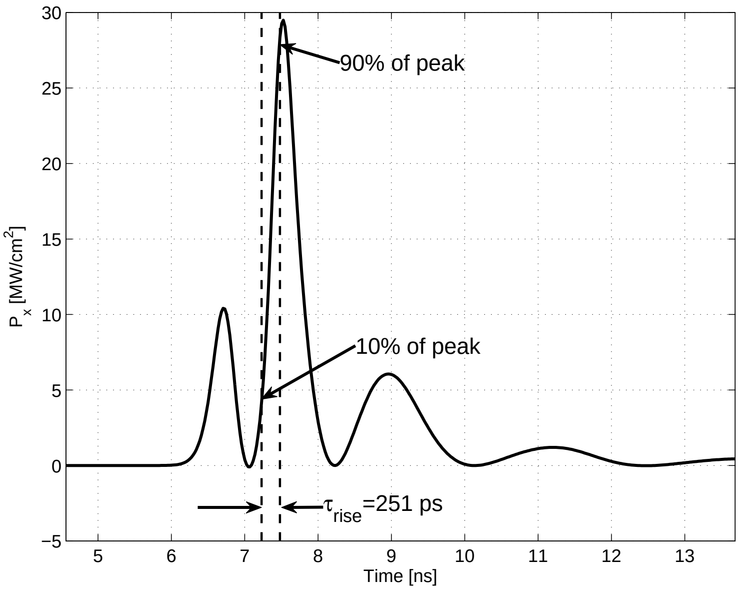

Figure 3.2: Rise time analysis: Minimum rise time as found 4.01 cm from the source plane

analogous to collapsing optical pulse, where the self-focusing phenomenon exceeds the loss and dispersion effects [39, 84, 85]. In a real fabricated structure, it is anticipated that the compression will be limited by one or more of the following effects: dissipation, Drude-Lorentz model-like frequency dispersion (relaxation), finite response time and/or dielectric breakdown. Sufficient BST characterization data was not available at the time of this work to include Drude-Lorentz dispersion or finite response time in these simulations. Static dissipation and breakdown limits are imposed as discussed is Section 3.4.

Moving from WR90 towards the design of a much smaller SIW inherently reduces the magnitude of the source voltage required to reach the necessary field strength. Achieving greater compression necessitates both driving a greater portion of the ferroelectric material within the waveguide into the nonlinear polarization region, and achieving good input and output impedance matching. The tapering nature of the TE_{10} mode field distribution suggests the use of different slabs of material with varying properties across the waveguide width. The material slab(s) are placed vertically (boundaries on the xy plane) to take advantage of continuity of electric fields when tangent to material boundaries (E_y is the dominant field component). This design has the advantage that flowing power concentrates in the slab(s) with greatest permittivity (lowest η).

The structure is similar to the classical problem of the slab filled waveguide. Such structures can be analyzed by variational techniques [32], which predict the presence of hybrid modes (not purely TE or TM) that are subject to boundary continuity conditions. These modes are complex functions of the permittivity, slab width, and slab location. As with many dielectric waveguide structures, further analytical assessment (especially with added nonlinear permittivity) becomes extremely complex and impractical [54]. A numerical simulation and optimization approach will be used instead for determining the optimal placement and width of material layers. If a number of ferroelectric materials with different properties are available, such as what would result from BST with a variable barium-to-strontium ratio for a fixed operating temperature, the design problem also includes the selection of a material for each layer.

3.2 Structure

Practical design requires constraining the optimization search space to be compliant with the fabrication limits of the LTCC substrate. The design is based on 8 layers of LTCC sheets with punched vias for the sidewall posts (further details in Section 7.1). Additional overlapping punched vias form trenches that are subsequently filled with BST by a sol-gel process (further details in Section 7.2). Some LTCC must remain between the BST layers to form trench walls of sufficient structural rigidity, so a cross section of the SIW has alternating vertical layers of ferroelectric BST and LTCC, as shown in Figure 3.3. The general layout and design rules for SIWs are given in Section 2.2.3. The fixed design parameters are summarized in Table 3.1.

The LTCC material used in the simulations was based on DuPont® GreenTape® 9k7, with $\varepsilon_r = 7.1$. Depending on the barium ratio x, pure BST has relativity permittivity of 1000 or greater and as such presents a large intrinsic impedance mismatch with the LTCC

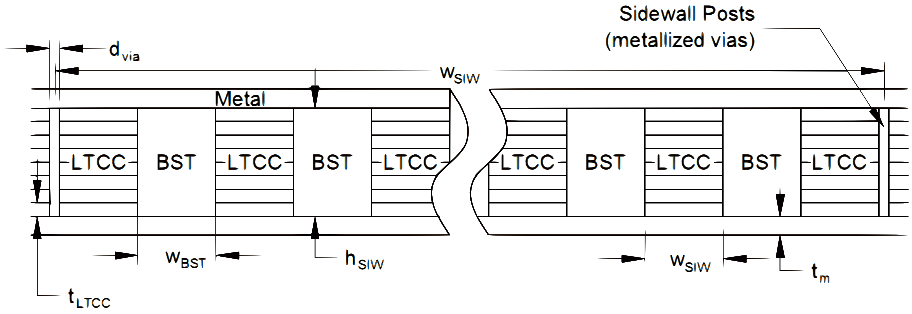

Figure 3.3: Cross section the nonlinear SIW

Parameter Name	Symbol	Value	Units
Sidewall Via Diameter	d_{via}	1.625	mm
Sidewall Via Pitch	p_{via}	2.438	mm
SIW Width between wall vias	w_{SIW}	8.58	mm
SIW Width to Height	-	~ 10	ratio
Bottom Metalization Thickness	t_m	9	μm
Top Metalization Thickness	t_m	3	μm
Fired LTCC Layer Thickness	t_{LTCC}	104	μm
Total Thickness / SIW height	h_{SIW}	832	μm
Minimum BST Layer Thickness	$t_{BST,min}$	~250	μm
Minimum LTCC between BST Layers	$t_{LTCC,min}$	~250	μm
Microstrip Width ($Z_0 = 50\,\Omega$)	w_{μ}	1.086	mm
Microstrip Taper Width ($Z_0 = 50\,\Omega$)	w_e	2.272	mm
Microstrip Taper Length ($3\lambda_{LTCC}/4$)	l_{taper}	8.58	mm
Lowest mode cutoff frequency	$f_{c_{10}}$	6.56	GHz
Standard operating band	$f_{min} - f_{max}$	8.4-12.4	GHz

Table 3.1: Fixed design parameters

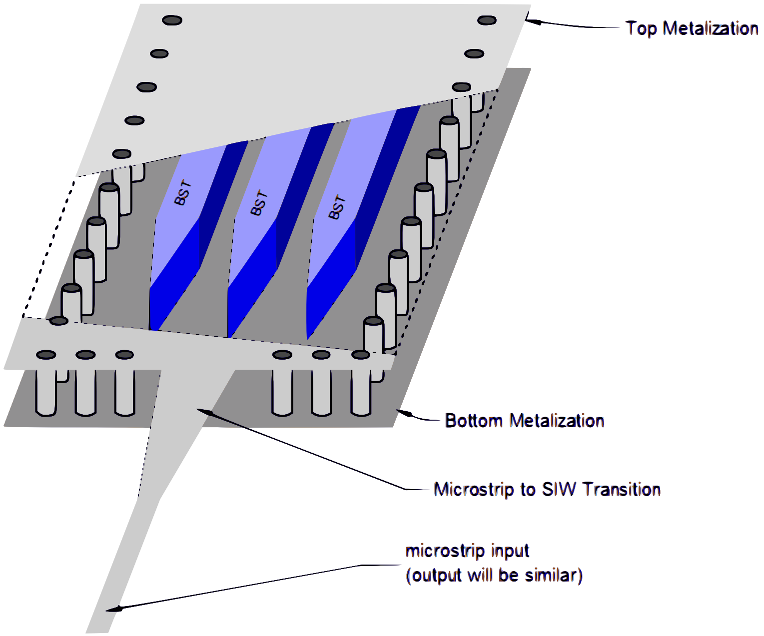

Figure 3.4: SIW design with tapered end BST layers

substrate ($\eta_{LTCC} \gg \eta_{BST}$) (see equation (2.20)). Attempting to inject energy directly into the ferroelectric layers will result in a large reflection coefficient (equation (3.1)) for waves normally incident on the material boundary.

$$|\Gamma_\perp| = \left| \frac{\eta_{BST} - \eta_{LTCC}}{\eta_{BST} + \eta_{LTCC}} \right| \geq 0.93 \tag{3.1}$$

The presented design tapers the ends of the BST layers (taper in $\hat{z}$), as shown for the input in Figure 3.4. The tapering results in gradual impedance match between the LTCC and the BST. The effect utilized is very similar to the impedance matching of horn antennas [86] and of wedge or pyramidal anechoic foam.

For simple tapered impedance matching structures, the length of the taper is usually set to odd multiples of one-quarter wavelength. Since the wavelength within the BST layers is function of the nonlinear permittivity, the optimal length of the taper can not be determined in a straight forward manner. Instead, the length of taper will be considered as another parameter for optimization.

3.3 Feed Structure

Tapered microstrip transitions, as shown in Figure 3.4, feed the designed SIW and extract energy from it, as outlined in Section 2.2.3. The optimal width is 2.272 mm, based on an empirical formulation by Deslondes [7]. The length of taper is set to an odd multiple of one-quarter wavelength (in LTCC). If the BST layers were to begin immediately at the microstrip to SIW boundary, the optimum width of the transition (w_e) could not be determined by the mode matching method described earlier due to the effects of the BST slabs. Reflections due to the transition would also be combined with reflections due to the BST impedance mismatch and the effects would be inseparable. Instead, a sufficient length of standard SIW (only LTCC and metal) acts as a buffer layer to ensure a TE_{10} mode is fully developed before the wave enters the BST layers. A similar section of standard SIW is provided between the BST and the output transition. These sections insure the mode matching method can be used and the feed structure does not have to be simulated during the optimization process. Instead, a planar TE_{10} mode wave is driven within a short buffer region, as discuss in Section 4.5.

3.4 Models and Initial Materials

While numerous studies on the parameters of BST have been published [69, 73, 74, 83, 87, 88], the conditions for measurement vary widely with predictably wide ranging results. Most studies and applications have focused on BST thin films, which have significantly lower permittivity ($\varepsilon_r \approx 150 - 300$) (due to surface interactions) than the bulk permittivity. Very limited data is available on bulk BST at microwave frequencies, which makes bounding a permittivity estimate difficult. A complete design for mass production would require testing of the BST under very similar conditions as the final application. This adds an interdependency to the design process, in that optimal layer thickness depends on permittivity and tunability, which are parameters that are themselves functions of layer thickness. The iterative design process required to work past this dilemma is beyond the scope of this work. Instead, a set of theoretical material parameters will be created based on reasonable approximations using Vendik's model [8], as discussed in Section 2.3.6.

As discussed in Section 2.3.5, precise control of the BST ratio can provide control of that material's low field permittivity ($\varepsilon_r(0)$) and tunability, assuming temperature and all other parameters remain constant. For the initial study of this work, a set of theoretical materials is created by assuming a range of BST ratios from 0.25 to 0.5 in 10 steps. BST with $x = 0.5$ exhibits a Curie-Weiss temperature ($\sim 300K$) nearest room temperature, and thus has greatest permittivity and tunability. BST with $x \leq 0.5$ are also in the paraelectric phase at room temperature. For the same operating temperature, all other material options are 'detuned' further away from their Curie-Weiss temperature and thus have lower low-field permittivity and lower tunability.

Even with the tapering structure described earlier, the large intrinsic impedance mismatch between pure BST and LTCC make efficient coupling between two materials difficult. Adding dopants (as discussed in sections 2.3.5 and 7.2) mitigates this problem by reducing the high permittivity of pure BST, at the cost of partial reduction in tunability. Permittivity can typically be reduced by a factor of 2 to 10 [73, 74, 89–91] depending on dopant concentration and minimum desired tunability. For the work, the low-field permittivity was assumed to be reduced by a factor of 10 from the values given by Vendik's model, while the tunability was reduced by 70%. The resulting material set is shown in Figure 3.5.

As with the permittivity, dielectric loss and breakdown limits are hard to predict without material testing. Vendik [92] measured average dielectric loss for thin-film single-crystal BST with $x = 0.65$ at $\tan\delta = 0.02$ at 10 GHz. The BST layers proposed in this work are unlikely to be single crystal (due to sol-gel process and sintering temperature constrains) and are thicker than 'thin-films', which suggests loss would be greater than Vendik's measurement. However, the addition of dopants reduces dielectric loss [73,74,89], so the single-crystal value

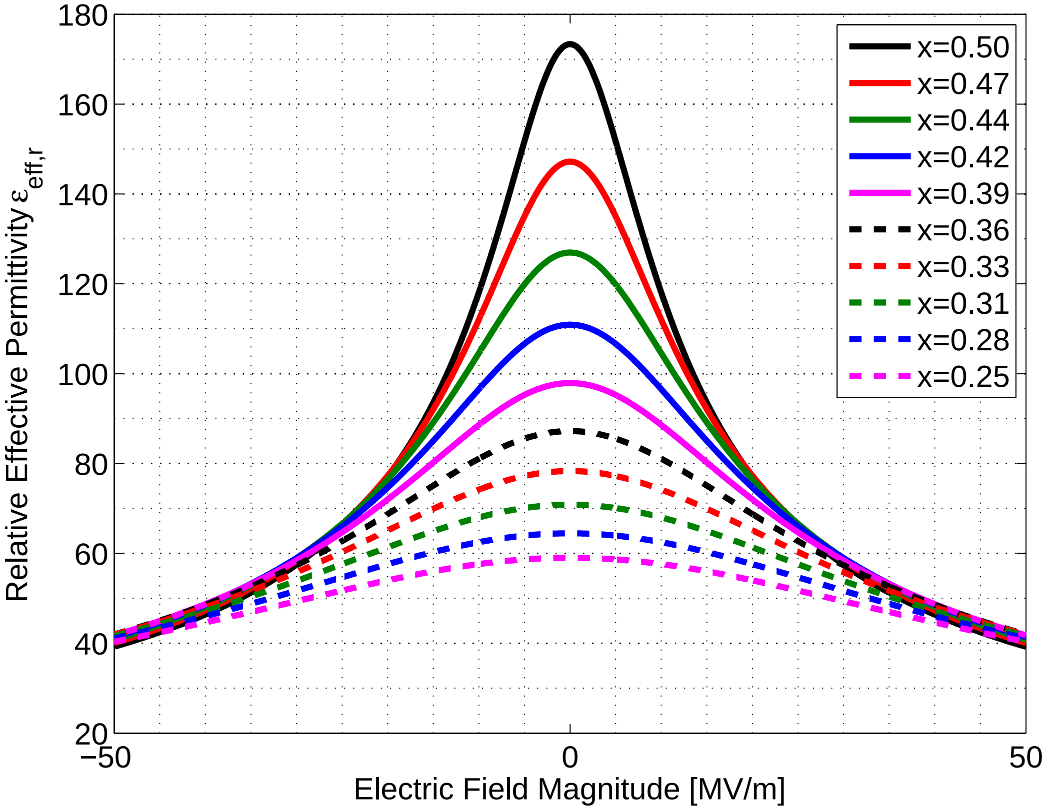

Figure 3.5: Theoretical material set

of $\tan\delta = 0.02$ will still be used for all material options. The dielectric breakdown limit was taken to be 120 MV/m for all materials [93].

Chapter 4

Computational Electromagnetics Method

Propagation of electromagnetic waves through a ferroelectric material in a waveguide involves many complex processes as described in the previous chapters. A full analytical description of the fields within the proposed structure would be cumbersome at best, if at all possible. Instead, a three dimensional numerical simulation of the fields via Maxwell's equations will act as the forward solver for optimization. The use of wideband pulses make frequency domain methods, such as method of moments or finite-element, less than ideal. The finite difference time domain (FDTD) method was selected based on the simplicity of implementation and simple integration of nonlinearities. This method has historically been limited by the large computation burden as described in Section 4.6. Advances in processor speed and techniques to bound the simulation domain have made the FDTD method practical for many small scale problems. The FDTD method used in this work is based on the development by Yee [94] and Taflove [45].

4.1 Finite Difference Time Domain Method and Maxwell's Equations

The FDTD method begins with the time domain point form of Maxwell equations as given in (4.1) and (4.2).

$$\nabla \times \mathbf{E} = \frac{\partial \mathbf{B}}{\partial t} \tag{4.1}$$

$$\nabla \times \mathbf{H} = \mathbf{J} + \frac{\partial \mathbf{D}}{\partial t} \tag{4.2}$$

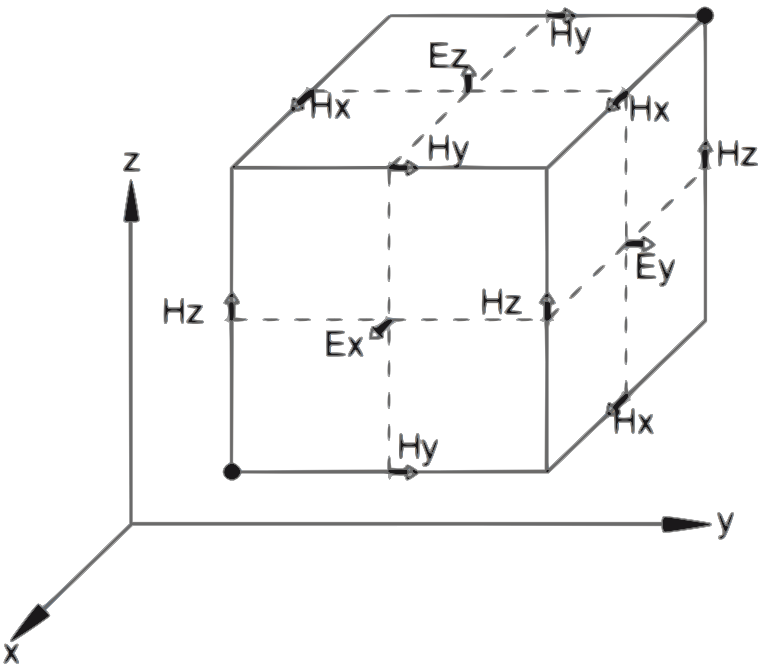

Figure 4.1: Spatial interleaving of the FDTD method

For this work a Cartesian coordinate systems will be used for the expansion of the curl operators (4.3) and (4.3).

$$\begin{aligned} \frac{\partial E_z}{\partial y} - \frac{\partial E_y}{\partial z} &= \frac{\partial B_x}{\partial t} \\ \frac{\partial E_x}{\partial z} - \frac{\partial E_z}{\partial x} &= \frac{\partial B_y}{\partial t} \\ \frac{\partial E_y}{\partial x} - \frac{\partial E_x}{\partial y} &= \frac{\partial B_z}{\partial t} \end{aligned} \tag{4.3}$$

$$\begin{aligned} \frac{\partial H_z}{\partial y} - \frac{\partial H_y}{\partial z} &= J_x + \frac{\partial D_x}{\partial t} \\ \frac{\partial H_x}{\partial z} - \frac{\partial H_z}{\partial x} &= J_y + \frac{\partial D_y}{\partial t} \\ \frac{\partial H_y}{\partial x} - \frac{\partial H_x}{\partial y} &= J_z + \frac{\partial D_z}{\partial t} \end{aligned} \tag{4.4}$$

First-order finite-difference approximations replace the spatial and time derivatives as (4.5) and (4.6) respectively, where s represents any differential direction, Δs is the spatial step and Δt is the time step.

$$\frac{\partial X}{\partial s} \rightarrow \frac{X_s - X_{s-1}}{\Delta s} \tag{4.5}$$

$$\frac{\partial X}{\partial t} \rightarrow \frac{X^n - X^{n-1}}{\Delta t} \tag{4.6}$$

Applying (4.5) and (4.6) to (4.3) and (4.4) gives the FDTD core equations (4.7) through (4.12). The error caused by the first order difference is offset by the spatial interleaving of the **E** and **H** components, as indicated by the subscript indicies and shown on the the unit cube in Figure 4.1. If the time steps are also interleaved for each component, as indicated by the superscripts in the follow equations, the resulting FDTD system will be second order accurate despite only using first order differences [45].

$$\frac{E^{n-1/2}_{z(x-1/2,y+1/2,z+1)} - E^{n-1/2}_{z(x-1/2,y+3/2,z+1)}}{\Delta y} - \frac{E^{n-1/2}_{y(x-1/2,y+1,z+1/2)} - E^{n-1/2}_{y(x-1/2,y+1,z+3/2)}}{\Delta z} = \frac{B^{n+1}_{x(x-1/2,y+1,k+1)} - B^{n}_{x(x-1/2,y+1,k+1)}}{\Delta t} \tag{4.7}$$

$$\frac{E^{n-1/2}_{x(x,y+1/2,z+1/2)} - E^{n-1/2}_{x(x,y+1/2,z+3/2)}}{\Delta z} - \frac{E^{n-1/2}_{z(x-1/2,y+1/2,z+1)} - E^{n-1/2}_{z(x+1/2,y+1/2,z+1)}}{\Delta x} = \frac{B^{n+1}_{y(x,y+1/2,z+1)} - B^{n}_{y(x,y+1/2,z+1)}}{\Delta t} \tag{4.8}$$

$$\frac{E^{n-1/2}_{y(x-1/2,y+1,z+1/2)} - E^{n-1/2}_{u(x+1/2,y+1,z+1/2)}}{\Delta x} - \frac{E^{n-1/2}_{x(x,y+1/2,z+1/2)} - E^{n-1/2}_{x(x,y+3/2,z+1/2)}}{\Delta y} = \frac{B^{n+1}_{z(x,y+1,z+1/2)} - B^{n-1}_{z(x,y+1,z+1/2)}}{\Delta t} \tag{4.9}$$

$$\frac{H^{n}_{z(x,y+1,z+1/2)} - H^{n}_{z(x,y,z+1/2)}}{\Delta y} - \frac{H^{n}_{y(x,y+1/2,z+1)} - H^{n}_{y(x,y+1/2,z)}}{\Delta z} + J^{n}_{x(x,y+1/2,z+1/2)} = \frac{D^{n+1/2}_{x(x,y+1/2,z+1/2)} - D^{n-1/2}_{x(x,y+1/2,z+1/2)}}{\Delta t} \tag{4.10}$$

$$\frac{H^n_{x(x-1/2,y+1,z+1/2)} - H^n_{x(x-1/2,y+1,z-1/2)}}{\Delta z} - \frac{H^n_{z(x,y+1,z+1/2)} - H^n_{z(x-1,y+1,z+1/2)}}{\Delta x} + J^n_{y(x-1/2,y+1,z+1/2)} = \frac{D^{n+1/2}_{y(x-1/2,y+1,z+1/2)} - D^{n-1/2}_{y(x-1/2,y+1,z+1/2)}}{\Delta t} \tag{4.11}$$

$$\frac{H^n_{y(x,y+1/2,z+1)} - H^n_{y(x-1,y+1/2,z+1)}}{\Delta x} - \frac{H^n_{x(x-1/2,y+1,z+1)} - H^n_{x(x-1/2,y,z+1)}}{\Delta y} + J^n_{z(x-1/2,y+1/2,z)} = \frac{D^{n+1/2}_{z(x-1/2,y+1/2,z)} - D^{n-1/2}_{z(x-1/2,y+1/2,z)}}{\Delta t} \tag{4.12}$$

Allowing for conducting materials to be simulated requires the current density term $\mathbf{J}$ be broken into a source current density ($\mathbf{J}_{source}$) and a conduction current given by (4.13). The source current term has been omitted from all subsequent equations for simplicity.

$$\mathbf{J}_c = \sigma \mathbf{E}^n \tag{4.13}$$

Since the electric fields are updated at one-half offset time steps, the electric field used to compute the conduction current is approximated by the semi-implicit method as shown in (4.14).

$$\mathbf{E}^n = \frac{\mathbf{E}^{n+1/2} - \mathbf{E}^{n-1/2}}{2} \tag{4.14}$$

The next step in forming the update equations of the FDTD method involves relating the electric and magnetic flux densities $\mathbf{D}$ and $\mathbf{B}$ to the field quantities. These are initially assumed to be linear functions of the fields, related by permittivity and permeability respectively, as given in (4.15) and (4.16).

$$\mathbf{D} = \varepsilon \mathbf{E} = \varepsilon_0 \varepsilon_r \mathbf{E} \tag{4.15}$$

$$\mathbf{B} = \mu \mathbf{H} = \mu_0 \mu_r \mathbf{H} \tag{4.16}$$

In the final step, the permittivity, permeability and conductivity are all allowed to be functions of space with finite boundaries along the same lattice as the field components. Since the field component are computed at either the face centers or the lattice edges, the constitutive parameters must be averaged across the material boundaries. The parameter(s) aligned with components on the face center must be treated as two values in parallel ($X_{ave} = (X_1 \times X_2)/(X_1 + X_2)$. The parameter(s) aligned with the components at the lattice edges is simply the arithmetic mean of the four surrounding values. The unit cube in Figure 4.1 displays one convention of spatial interleaving, with **E** components on face centers and **H** components on edges; however a dual convention exists where **H** components are on face centers, **E** components are on edges, and the constitutive parameters are averaged accordingly. The averaging operation produces a side effect that single cell perturbations in the constitutive parameters cannot be accurately modeled and thus must be avoided through choice of geometry and lattice spacing [95].

The discrete form curl equations (4.7) through (4.12) are now rearranged into the update equations (4.17)-(4.22) and material specific coefficients (4.23) - (4.26). These coefficients are specific to and collocated with their associated field terms using the previously discussed averaging. The associated spatial indicies are omitted for simplicity.

$$\begin{aligned} E^{n+1/2}_{x(x,y+1/2,z+1/2)} &= C_a E^{n-1/2}_{x(x,y+1/2,z+1/2)} \\ &\quad + C_b \left(H^n_{z(x,y+1,z+1/2)} - H^n_{z(x,y,z+1/2)} - H^n_{y(x,y+1/2,z+1)} + H^n_{y(x,y+1/2,z)} \right) \end{aligned} \tag{4.17}$$

$$\begin{aligned} E^{n+1/2}_{y(x-1/2,y+1,z+1/2)} &= C_a E^{n-1/2}_{y(x-1/2,y+1,z+1/2)} \\ &+ C_b \left(H^n_{x(x-1/2,y+1,z+1/2)} - H^n_{x(x-1/2,y+1,z-1/2)} - H^n_{z(x,y+1,z+1/2)} + H^n_{z(x-1,y+1,z+1/2)} \right) \end{aligned} \tag{4.18}$$

$$\begin{aligned} E^{n+1/2}_{z(x-1/2,y+1/2,z)} &= C_a E^{n-1/2}_{z(x-1/2,y+1/2,z)} \\ &+ C_b \left(H^n_{y(x,y+1/2,z+1)} - H^n_{y(x-1,y+1/2,z+1)} - H^n_{x(x-1/2,y+1,z+1)} + H^n_{x(x-1/2,y,z+1)}\right) \end{aligned} \tag{4.19}$$

$$\begin{aligned} &H^{n+1}_{x(x-1/2,y+1,k+1)} = D_a H^n_{x(x-1/2,y+1,k+1)} \\ &+ D_b \left(E^{n-1/2}_{z(x-1/2,y+1/2,z+1)} - E^{n-1/2}_{z(x-1/2,y+3/2,z+1)} - E^{n-1/2}_{y(x-1/2,y+1,z+1/2)} + E^{n-1/2}_{y(x-1/2,y+1,z+3/2)}\right) \end{aligned} \tag{4.20}$$

$$\begin{aligned} &H^{n+1}_{y(x,y+1/2,z+1)} = D_a * H^n_{y(x,y+1/2,z+1)} \\ &+ D_b \left(E^{n-1/2}_{x(x,y+1/2,z+1/2)} - E^{n-1/2}_{x(x,y+1/2,z+3/2)} - E^{n-1/2}_{z(x-1/2,y+1/2,z+1)} + E^{n-1/2}_{z(x+1/2,y+1/2,z+1)}\right) \end{aligned} \tag{4.21}$$

$$\begin{aligned} &H^{n+1}_{z(x,y+1,z+1/2)} = D_a H^n_{z(x,y+1,z+1/2)} \\ &+ D_b \left(E^{n-1/2}_{y(x-1/2,y+1,z+1/2)} - E^{n-1/2}_{y(x+1/2,y+1,z+1/2)} - E^{n-1/2}_{x(x,y+1/2,z+1/2)} + E^{n-1/2}_{x(x,y+3/2,z+1/2)}\right) \end{aligned} \tag{4.22}$$

$$C_a = \frac{\left(1 - \frac{\sigma \Delta t}{2\varepsilon}\right)}{\left(1 + \frac{\sigma \Delta t}{2\varepsilon}\right)} \tag{4.23}$$

$$C_b = \frac{\left(\frac{\Delta t}{\varepsilon \Delta s}\right)}{\left(1 + \frac{\sigma \Delta t}{2\varepsilon}\right)} \tag{4.24}$$

$$D_a = \frac{\left(1 - \frac{\sigma * \Delta t}{2\mu}\right)}{\left(1 + \frac{\sigma * \Delta t}{2\mu}\right)} \tag{4.25}$$

$$D_b = \frac{\left(\frac{\Delta t}{\mu \Delta s}\right)}{\left(1 + \frac{\sigma * \Delta t}{2\mu}\right)} \tag{4.26}$$

In the FDTD process, all the components of **E** are solved across the entire lattice for a single time step n based on the prior value of **E** and **H**. Then all the values of **H** are solved across the lattice for the next half offset time step $n + 1/2$. This pattern of solving all **E** and then all **H** and repeating is known as leapfrogging in time. It must be noted that the first order differences cannot compute all the fields at the edge of the spatial domain. Because of this, the E-field components tangent to the edges are not computed and will always remains at the initial value of zero. This has the effect of placing perfect electric conductors (PEC's) at the boundaries. Since PEC's are purely reflective, energy injected into the FDTD lattice can never escape through loss-less propagation, and is therefore dissipated only by conduction currents. Thus accurately simulating any system that has propagating electromagnetic fields requires special absorbing boundary conditions (ABC's) adjacent to the inherent PEC's. The ABC's selected for this work and their implementation are described in Section 4.3.

4.2 FDTD Parameter Considerations

The FDTD method requires the space be divided into a finite lattice. The phase velocity error caused by finite division can be kept manageable ($< 0.5\%$) if each cell represents no more than $1/20^{th}$ of a wavelength in any direction at the shortest wavelength of interest. For single mode operation in a waveguide, the lattice spacing (Δs) must be set to (at most) the wavelength of the next highest order mode cutoff $f_{c_{20}}$. Accurately representing pulse compression (and associated higher frequency content) demands an even finer lattice spacing. Additionally, the wavelengths are smaller within the BST by a factor of $\sqrt{\varepsilon_{LTCC}/\varepsilon_{BST}}$, which

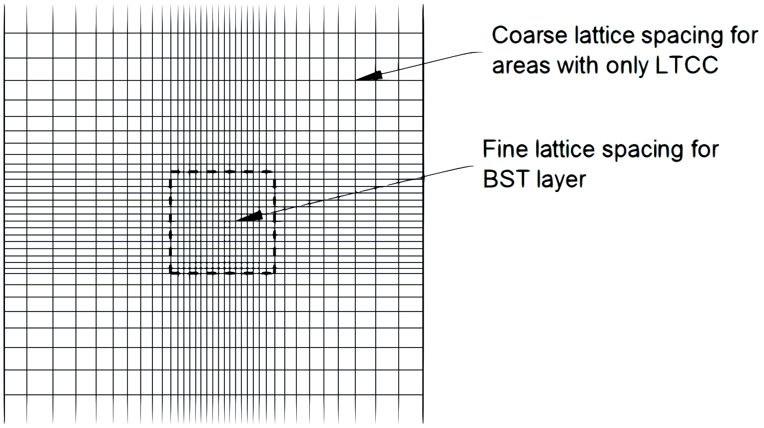

Figure 4.2: Nonuniform FDTD lattice

is approximately ~ 0.2 for the largest permittivity material option ($\varepsilon_r \approx 173$). Applying a uniform grid that would be sufficiently fine for accurate simulation of the BST layers would result in an extremely large number of cells ($10^8 - 10^9$), which results in impractically large memory requirements and simulation times.

A nonuniform grid, as shown in Figure 4.2, can be used to mitigate the additional computational burden. Monk and Süli [96, 97] examined the nonuniform FDTD grid and have shown that the change in cell size does produce some localized first-order error, but is still globally second-order accurate (known as 'supra-convergence'). The local first-order error can be minimized by making the difference in adjacent cell sizes small ($\leq 15\%$ typically). This method was implemented in two dimensions, $\hat{x}$ and $\hat{z}$, while the cell size in waveguide height dimension $\hat{y}$ remained constant. The cell size Δx and Δy within the BST layers was set to $\Delta_{min} = \lambda_{min}/10$ where λ_{min} is the wavelength in $\varepsilon_r = 173$ at a frequency four times the input pulse center frequency ($4f_{cent}$) (see Section 4.5). Moving away from the BST layers within the LTCC, Δx and Δy are increased by 10% per cell until a maximum spacing of $\Delta_{max} = \lambda_{LTCC}/10$ at $f = 4f_{cent}$ is reached. Memory limits preclude a smaller cell spacing.

Since the waveguide width-to-height ratio $a/b \approx 10$ in this work, the first higher order vertical mode (TE_{n1}, one half-wavelength in $\hat{y}$) has a cutoff frequency 10 times that of the fundamental TE_{10} mode. Using the same selected maximum frequency of interest $f = 4f_{cent}$,

Δt	321 fs (95% of Courant Limit)
Δx_{min}	57 um
Δy_{min}	114 um
Δz_{min}	57 um
c_{max}	$1.126 * 10^8$ m/s

Table 4.1: FDTD simulation parameters

the waveguide height represents at small fraction of a wavelength . As such, Δ_y can be 2 times larger than Δ_z, which further reduces the size of the spatial domain.

The time step is regulated by the Courant-Friedrichs-Lewy condition (or simple Courant condition) as given by (4.27), where c_{max} is the maximum phase velocity encountered with the simulation space. The condition is a necessary condition of all finite difference algorithms that involve time stepping solutions to partial differential equations. Simply stated, the time step can be at most the amount of time a complete wave cycle takes to travel from one lattice point to the nearest adjacent point. In most simulations the spatial step is uniform in all three dimensions, however this is not required. The Courant condition can be expanded for nonuniform spacing as given in by (4.28). The parameters are summarized in Table 4.1.

$$\Delta t_{min} \leq \frac{\Delta s}{c_{max}\sqrt{3}} \tag{4.27}$$

$$\Delta t_{min} \leq \frac{1}{c_{max}\sqrt{\frac{1}{(\Delta x_{min})^2} + \frac{1}{(\Delta y_{min})^2} + \frac{1}{(\Delta z_{min})^2}}} \tag{4.28}$$

If high frequency content of a transient causes cell size to significantly exceed $\lambda_{min}/10$, error due to the finite spatial difference will cause non-physical effects. One such effect can be observed as the lattice erroneously appearing to generate energy during propagation in a lossy media (based on time integration of flowing power). This problem is exacerbated by a high contrast in material permittivity and the nonlinearity within a nonuniform grid: For a given time step, the maximum representable frequency is defined as $f_{max} = 1/(2\Delta_t)$. A minimum representable wavelength in defined at Δ_{max}, where Δ_{max} is the largest cell dimension. The FDTD algorithm operating at or near these limits is stable but displays poor accuracy. In this work, the time step must be set based on the smallest cell size and fasted phase velocity (lowest permittivity), which occurs in the LTCC for the cells adjacent to the BST. Within the LTCC, the maximum representable frequency and the minimum representable wavelength correspond closely. This does not hold for the BST, as the maximum representable frequency is much higher than the frequency that corresponds to the minimum representable wavelength within the BST. This situation allows high frequency noise, caused by discretization error, constitutive parameter averaging, numerical round off, etc., to start up within the BST where it can be represented temporally, but not spatially ($\lambda \ll 2\Delta$). This in turn leads to erroneous local increase in energy. A search of current literature on FDTD methods failed to reveal any suggested solution to this problem.

By careful examination of simulations, the majority of high frequency noise within the BST appears to be caused by rapidly changing permittivity (due to nonlinearity) at the output interface between the BST and LTCC. The large time derivative of permittivity would likely be nonphysical in a fabricated structure, since most dielectrics (including ferroelectric materials) have finite response time limits on polarization beginning in the $1/(10^9 - 10^{11}\,Hz)$ range. To mitigate this issue, a low-pass filter was applied to the electric field magnitude ($|\mathbf{E}|$) that is used to evaluate the permittivity (see Section 4.4). Applying a moving average to $|\mathbf{E}|$ effectively causes low-pass filtering with minimal computational burden. The number of time steps in the moving average controls the filter bandwidth, which is set to suppress spectral content of $|\mathbf{E}|$ that corresponds to a wavelength shorter than the minimum representable wavelength. For this work, 20 time steps are used. Because this approach is only a mitigation step and the final compression effects cannot be predetermined for any given solution, the total energy within the waveguide from all solutions must be checked to insure significant discretization error has not occurred (see Section 4.6).

4.3 Absorbing Boundary Conditions

In order to simulate the designed structure as an “in-line” device, special conditions must be setup at the edges of the simulation domain to make the input and output structure appear to be of infinite length. This effectively isolates the structure from source and load reflections, and allows simple measurements of insertion and return losses. These special conditions absorb virtually all energy incident on the computational boundary without reflection and are thus known as absorbing boundary conditions (ABC’s).

The absorbing boundary condition used in this work is a modified form of Berenger’s Perfectly Matched Layer (PML) [98]. Limitations of the original PML in discrete space for grazing angles of incidence and low frequencies resulted in the development of the complex frequency shifted (CFS) tensor modification [99]. Roden and Gedney developed an efficient method of implementing the CFS-PML using recursive convolution [100], thus known as the Convolutional PML or CPML . This method was added to the FDTD algorithm as outlined by Tavlove [45]. While a complete development of the CPML can be found in the above references, a brief summary of the the changes made to the FDTD update equations follows.

The CPML is implemented by the addition of auxiliary split-field PML terms (Ψ) to the update equations for each field term. Each of the six field terms has two ψ terms for the two orthogonal fields. For example, the update equations of E_x require the computation of $\Psi^n_{E_{x,y}}$ and $\Psi^n_{E_{x,z}}$. The second subscript direction indicates the operating PML boundary: $\Psi^n_{E_{x,y}}$ is the PML field term used to update E_x due to the PML on the $\hat{y}$ boundaries of the simulation space and $\Psi^n_{E_{x,z}}$ is the PML field term used to update E_x due to the PML on the $\hat{z}$ boundaries of the simulation space. These terms are updated based on the prior time step value (due to single point recursive convolution) and the immediately prior calculated magnetic field terms, as given by equation (4.29) (4.30)

$$\Psi^n_{E_{x,y}} = b_y(y)\Psi^{n-1}_{E_{x,y}} + c_y(y)\left(\frac{H^n_z - H^n_z}{\Delta y}\right) \tag{4.29}$$

Parameter	Value
a_{max}	0.005
κ_{max}	15
PML order (m)	3
$\sigma_{max} = \sigma_{opt}$	$\frac{0.8(m+1)}{\eta\delta_s} = 80.4$

Table 4.2: Maximum values for PML parameters, based on experimental findings in [11]

$$\Psi^n_{E_{x,z}} = b_z(z)\Psi^{n-1}_{E_{x,z}} + c_z(z)\left(\frac{H^n_y - H^n_y}{\Delta z}\right) \tag{4.30}$$

The spatial indicies of the Ψ terms always coincide with the indicies of the primary field term to be updated (E_x in this case) and have been omitted for simplicity in the above equations. The Ψ terms for the remaining 5 field terms and PML's are similar. Great care must be taken in coding these terms to insure correct vector directions and indexing. The coefficients for the above terms are as follows for general vector direction $\hat{w}$:

$$b_w = e^{-\left[\frac{\sigma_w}{\varepsilon_o\kappa_w} + \frac{a_w}{\varepsilon_0}\right]\Delta t} \tag{4.31}$$

$$c_w = \frac{\sigma_w}{\sigma_w\kappa_w + \kappa_w^2 a_w}\left[b_w - 1\right] \tag{4.32}$$

Where the PML loss parameters a_w, σ_w and κ_w are given by a polynomial grading scheme as given by [101]:

$$\sigma_w = \left[\frac{w}{d}\right]^m \sigma_{w,max} \tag{4.33}$$

$$\kappa_w = 1 + \left[\kappa_{w,max} - 1\right]\left[\frac{w}{d}\right]^m \tag{4.34}$$

$$a_w = \begin{cases} a_{w,max}\left[\frac{d-w}{d}\right]^m & 0 \le w \le d \\ 0 & otherwise \end{cases} \tag{4.35}$$

where d is the pml thickness, and the maximum value factors are set based on the experience of prior studies as listed in Table 4.2.

Finally, the Ψ terms modify the field update equations (E_x for example) as follows

$$E^{n+1/2}_{x(x,y+1/2,z+1/2)} = C_a E^{n-1/2}_{x(x,y+1/2,z+1/2)} + C_b \times$$
$$\left(\frac{H^n_{z(x,y+1,z+1/2)} - H^n_{z(x,y,z+1/2)}}{\kappa_y \Delta y} - \frac{H^n_{y(x,y+1/2,z+1)} + H^n_{y(x,y+1/2,z)}}{\kappa_z \Delta z} + \Psi_{E_{x,y}} - \Psi_{E_{x,z}} \right) \quad (4.36)$$

The split field method requires the multiplier κ to be applied to the spatial step independently in each direction ($\kappa = 1$ except within the PML's). As a result, the Δs term is moved back to the update equations and is removed from the coefficients C_b and D_b as shown in (4.37) and (4.38).

$$C_b = \frac{\left(\frac{\Delta t}{\varepsilon}\right)}{\left(1 + \frac{\sigma \Delta t}{2\varepsilon}\right)} \quad (4.37)$$

$$D_b = \frac{\left(\frac{\Delta t}{\mu}\right)}{\left(1 + \frac{\sigma * \Delta t}{2\mu}\right)} \quad (4.38)$$

The efficiency of the CPML relies on three properties: First, after the computation of the PML coefficients, the computation of the Ψ update terms is very straight forward and requires on five arithmetic operations per Ψ term per cell. Second, the coefficients (c_w and b_w) and the Ψ terms outside of the PML's are always zero. Spatial `for` loop based FDTD codes benefit from conditional implementation of the PML, where calculations are only performed when the stepping variables are within the PML's. Finally, the CPML does not have to be implemented in all three vector directions. In this work, PML's are used at the the $\hat{x}$ boundary (waveguide length) and sometimes at the $\hat{y}$ boundary (waveguide height), but not for the $\hat{z}$ boundary.

4.4 Ferroelectric Material Modeling

Vendik's model, as discussed in Section 2.3.6 and 3.4, is used for material modeling within the FDTD algorithm using equations (2.43) - (2.51). The core equation (4.39) (repeated here for convenience) uses the electric field vector magnitude $|\mathbf{E}|$ at each cell in place of the bias field term E_0 in ξ (see equation (2.46)). All fixed coefficients are calculated before time stepping begins, leaving only ξ and (4.39) to be computed at each time step.

$$\varepsilon_{eff}(T, E_0) = \frac{\varepsilon_{00}}{\left[(\xi^2 + \eta^2)^{1/2} + \xi\right]^{2/3} + \left[(\xi^2 + \eta^2)^{1/2} - \xi\right]^{2/3} - \eta} \tag{4.39}$$

This formulation causes an interdependence between ε_{eff} and the electric field magnitude. Several methods have been proposed and tested for solving this nonlinearity including iterative methods and auxiliary differential equation methods [102]. In this work, a simple Newton iteration approach is used for solving for ε_{eff} in the discrete time domain: ε_{eff} is first evaluated on the prior time step value of the electric field magnitude, then E_x, E_y, E_z and $|\mathbf{E}|$ are calculated, then ε_{eff} is evaluated based on the new electric field magnitude, then the field components are evaluated again. This process is repeated a few times on the same time step (all while continuing to use the $\mathbf{E}^{n-1/2}$ terms in the update equations). The iterations add significant computational burden [103]; however, numerous studies [45] have found 2 iterations to achieve sufficient accuracy. This is the approach used in this work.

Since hysteresis effects in BST with ratio near $x = 0.5$ are minimal at room temperature, hysteresis is not modeled. Dielectric losses are accounted for by manipulation of the loss tangent equation to create an effective conductivity, as given by (4.40), where $\sigma \ll \omega\varepsilon''$.

$$\sigma_{eff} = \sigma + \omega\varepsilon'' = (\tan\delta)\omega\varepsilon' \tag{4.40}$$

4.5 Source Pulse

Most NLTL studies use a Gaussian pulse for excitation and testing. The wideband nature of the Gaussian pulse in a waveguide is subject to multi-mode and cutoff frequency effects, as discussed in Section 2.2.1. In a real structure, attempting to inject energy with spectral content below the TE_{10} cutoff would result in a large reflection back down the input transmission line. In an FDTD simulation, if a $\mathbf{J}_{source}$ term or forced field terms (hard source) injects energy into the waveguide instead of another transmission line, any energy with spectral content below the TE_{10} cutoff will be reactive and linger near the source. This erroneous lingering energy is subject to the discretization error inherent to the FDTD process, which causes some energy to be transformed into a very slowly propagating wave. Energy injected at or slightly above the TE_{10} cutoff, while real and physically realizable, will also be very slow to leave the source since group velocity approaches zero at f_{c10} [45]. Since all waveguide structures act as high pass filters anyway, band limiting the signal to between $f_{c_{10}}$ and $f_{c_{20}}$ prevents the lingering energy issue. A cosine-modulated Gaussian pulse, as defined by (4.41) and shown in Figure 4.3, meets the requirement for a finite bandwidth, approximately finite time source. The center frequency f_{cent} is set exactly between $f_{c_{10}}$ and $f_{c_{20}}$ and Gaussian width τ is adjusted to keep the voltage of spectral content outside the desired band to less than 1% of the peak voltage V_0. The time offset t_0 is adjusted to insure the initial value $V_s(1)$ is at a waveform zero.

$$V_s(n) = V_0 \cos\left(2\pi f_{cent} t\right) e^{-\left(\frac{(t-t_0)^2}{\tau^2}\right)}; \tag{4.41}$$

The source pulse is fed into the FDTD lattice as an assumed TE_{10} mode field distribution. E_y components are set with a source drive plane ($x = x_{dr}$) with a cosine taper across the guide width ($\hat{z}$), as given by (4.42) and shown in Figure 4.4. z_{cent} represents the cell index at the middle of the guide, z_{segs} represents the number of cell across the guide width

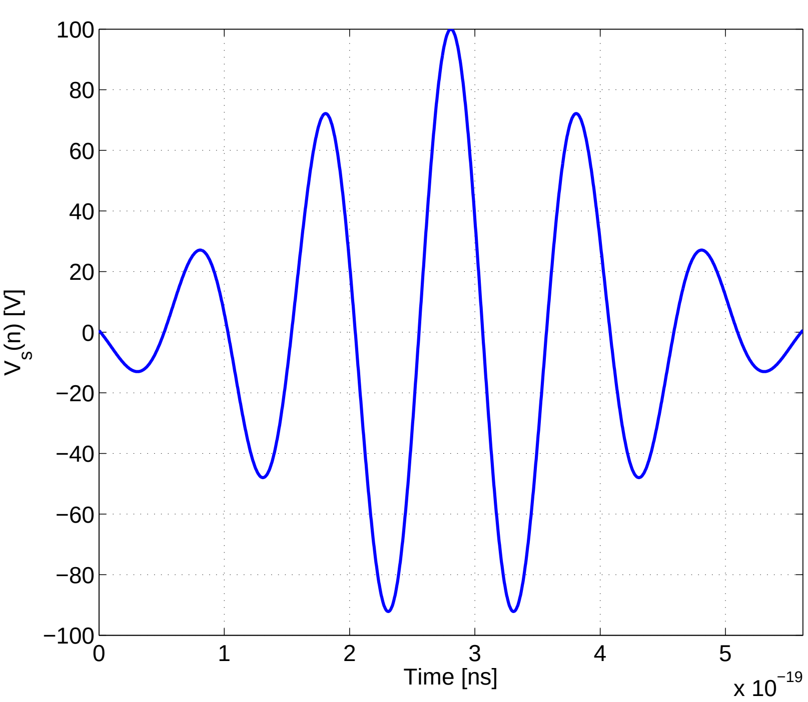

Figure 4.3: Cosine modulated Gaussian source pulse

and b represents the SIW height. The drive plane x_{dr} is located near 5 cells from the end PML, within the buffer layers as discussed in Section 3.3.

$$E^n_{y(x_{dr},y,z)} = E^n_{y(x_{dr},y,z)} + \frac{V_s(n)}{b}\cos\left(\frac{\pi}{2}\frac{z - z_{cent}}{z_{segs}/2}\right) \tag{4.42}$$

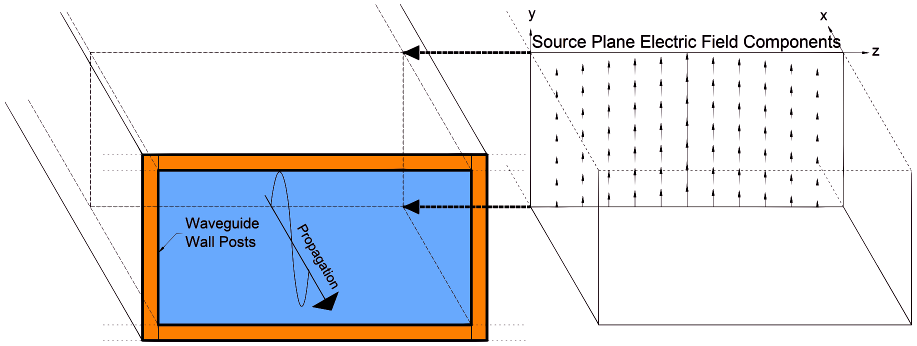

Figure 4.4: Field distribution for TE_{10} mode source

4.6 Computer Implementation and Requirements

The FDTD algorithm can be implemented in any programming language; however a language with native matrix processing vastly simplifies the programming process. MATLAB (version R2009a) was chosen based on its matrix processing and graphics capabilities. While a MATLAB implementation will be slower than a complied code such Fortran based FDTD, the rapid prototyping capability of MATLAB outweighs the reduction in speed. MATLAB Profiler was used extensively to reduced the overall run time by minimizing both redundant computations and the use of overly generalized built-in functions. Additionally, the nonlinear effective permittivity computation requires numerous calculations beyond the standard FDTD algorithm including computing the electric field magnitude and the recalculation of coefficients C_a and C_b. To limit the addition computation burden, the necessary operations are only carried out inside the nonlinear materials.

Further reduction of the simulation time is achieve by carefully limiting the computation domain and memory requirements. The standard FDTD algorithm requires the computation and holding of the electric and magnetic field values for three dimensions over the entire simulation space. For an elongated simulation domain such as a waveguide, if the source is placed at one end, a large portion of the simulation space far from the source will be have zero fields for many of the initial time steps. A large amount of time would be wasted if the entire waveguide was computed when most field terms are zero. In this work, a moving computational window was implemented to ensure only the region of the waveguide with meaningful fields would be computed, as shown in Figure 4.5. As the input pulse propagates down the waveguide, the computational window is steadily expanded to accommodate the pulse. The leading edge is advanced by one cell for each time step that electric field magnitude two cells from the leading edge exceeds $10^{-7}V_0$. After the source has sufficiently died out, the trailing edge of the computational window is conditionally advanced. Directly switching off the computation of cells that have small, but non-zero fields would result in spurious transients contaminating the simulation space. To overcome this problem, the conductivity

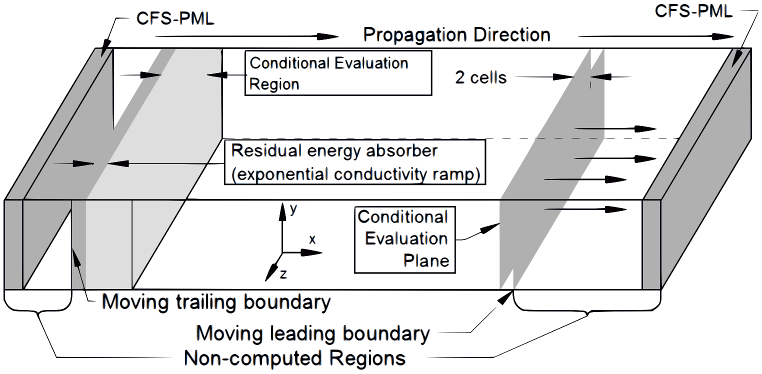

Figure 4.5: Moving computational window components

is exponentially ramped up for the 15 cells in front of the trailing edge of the computational window. This effectively dissipates any small remnant fields as conduction current. The trailing edge is conditionally advanced only when the electric field magnitude in a region 10 cells in front of the conductivity ramp has decreased to less than $10^{-8}V_0$. The trailing edge advance is not used anytime reflected fields are anticipated or observed to occur within any particular simulation.

Memory requirements must be carefully considered in any FDTD code. The simulations done in this work use $\sim 10^6$ cells and are carried out for 4,000 - 10,000 times steps. The six field terms alone occupy $\sim$ 50 megabytes of memory (8 bytes per double precision value) for single a time step with one million cells. Axillary terms, including the averaged material parameters, update coefficients, PML Ψ terms and associated coefficients, can easily double the memory requirement. While this requirement for a single time step is relatively modest by today's memory standards, attempting to recording all field terms for each time step is clearly not feasible. Fortunately, a smaller planar-cut sample of the dominant electric field (E_y) vector and/or the poynting vector taken every 10^{th} to 20^{th} time step is sufficient to observe the simulation results. Since power flowing down the waveguide is of greatest interest, calculation of the $\hat{x}$ poynting vector (4.43) is worth the added computation burden. Integrating the poynting vector over the planes transverse to the direction of propagation gives the total power flowing down the guide at any given location in $\hat{x}$ for any given time step. The equivalent discrete space integration is given by (4.44). The poynting vector and derived flowing power are extremely useful for observing discontinuities and impedance mismatch reflection. Incident power (leaving the source) appears as a positive P_x or $P_{f,x}$ and reflected power is negative for both, allowing for easy distinction when both incident and reflected wave are present. The total energy that has passed through a plane is found by integrating (summing) the power flowing through the plane over time, as shown in (4.45)

$$P_x = E_y \times H_z - E_z \times H_y \tag{4.43}$$

$$P_{f,x}(x) = \sum_{y=0}^{h} \sum_{z=0}^{w} P_x(x, y, z) \Delta y \Delta z \tag{4.44}$$

$$W(x, n) = \sum_{1}^{n} P_{f,x}(x, t) \delta t \tag{4.45}$$

At the conclusion of each time step, two key parameter checks are performed: First, the maximum electric field magnitude is found for all cells within the lattice. If a value greater than breakdown threshold $|\mathbf{E}|_{max} = 120MV/m$ is detected, the simulation is halted and the GA is instructed to consider the solution invalid. Second, the spatial derivative of total energy $\partial W(x, n)/\partial x$ down the guide evaluated. A positive value of this derivative anywhere away from the source region indicates excessive computational error has occurred causing erroneous increasing energy (see discussion is Section 4.2). Solutions exhibiting this behavior are also considered invalid by the GA.

4.7 Validation

The core FDTD algorithm (without nonlinearity) was validated by simulation of a SIW using the microstrip input and output lines and tapered transitions (see Section 2.2.3). This simulation structure was identical to the fabricated structure in Chapter 8. Using a band limited source, a very small loss ($\sim 0.6dB$ reduction in power) was observed from input to output. Simulations using a wide-band source (Gaussian pulse) agreed the expected high pass filtering effect of the SIW and the limited operational bandwidth of the transition. Further details of this validation study can be found in appendix B.

Chapter 5

Genetic Algorithm Optimization

Given the complexity of the design and nonlinear effects, a broad search was desired to find the optimal design parameters for maximum pulse compression. Genetic Algorithm (GA) optimization has be shown to be particularly useful for electromagnetic problems [104–107] and was selected for use in this work. The following sections outline the GA method and the implementation used in this work.

5.1 Process Outline

In the GA method, each design parameter is known as a gene. Binary (integer) or decimal coding can be used for the genes; the choice is mostly at the preference of the programmer. The collection of all genes represents one complete solution to the design. A random number generator fills an initial population of solutions at the start of the GA. A forward solver evaluates each solution to determine a how well it satisfies the goal of the problem and assigns a fitness value. All solutions are then ranked by their fitness value. Processes of retention, selection, cross over and mutation probabilistically create the next generation of solutions (child solutions) in a way that tends to track the best solutions while still searching globally. The process repeats with the new generation of solutions and continues to repeat until a convergence condition has been detected. A generic process outline is shown in Figure 5.1.

5.2 Genes

Integer codes was chosen to represent the genes for this work. Only during the process of crossover and mutation are the integer values converted to the binary using the `dec2bin`

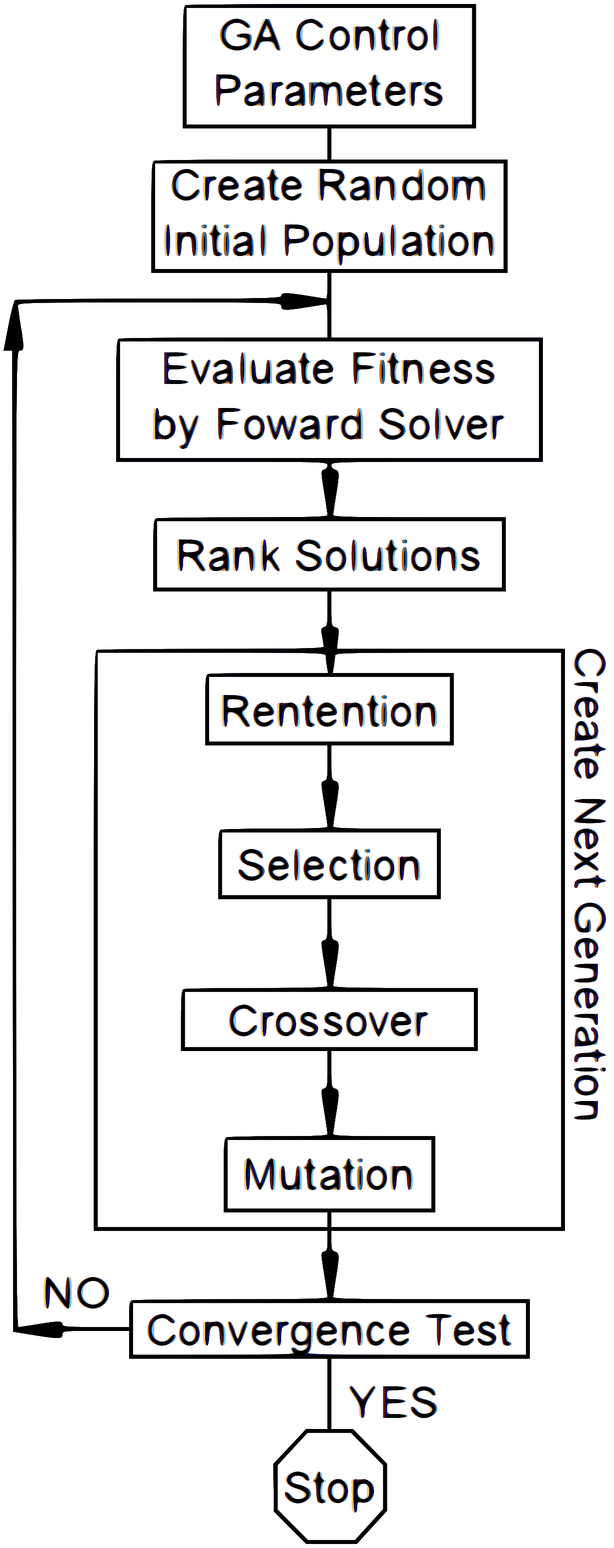

Figure 5.1: Basic genetic algorithm flow chart

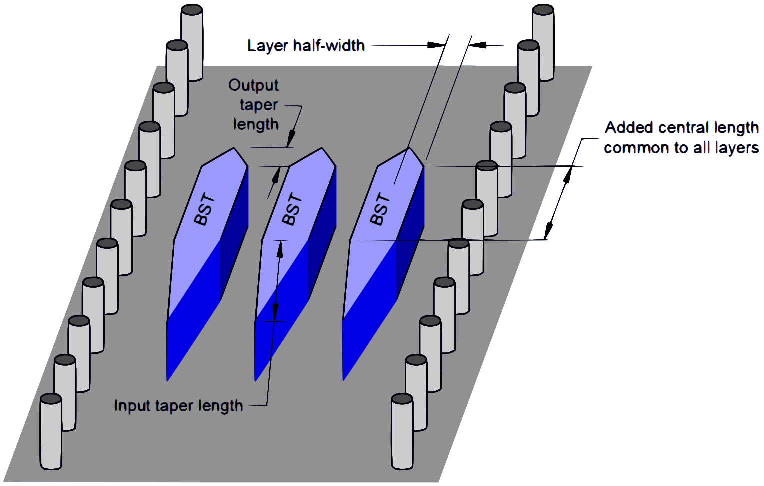

Figure 5.2: Desgin parameters controlled by the GA

command. Binary values are held as character arrays by MATLAB and must be processed as such for logical tests and setting of values. Once mutation is complete, the `bin2dec` command converts the genes back to integer form. The structure was broken into optimization parameters as follows: N_L layers of BST were established with their centers (in $\hat{z}$) evenly divided across the width of the SIW. Each layer is allowed to be one of the 14 material options and have a variable thickness, input taper length and output taper length. The layer thickness is specified as the half-thickness on each side of the center point, from 3 to 50 cells. This results in a total thickness of 6 to 100 cells respectively. The input and output taper length can vary from 1 cell to 63 cells, representing a range several wavelengths in the BST. The total length of the SIW to be simulated is variable based on the combined longest taper lengths, plus an additional gene used to represent an added center length. Finally, since the response is dependent on the the amplitude of the input pulse, a gene was assign for control of this amplitude from 300V to 6,300V in 100V steps. Figure 5.2 and Table 5.1 summarizes the genes used.

Parameter	Possible Values	Bits
Material ID number	1-10	$4N_L$
Input Taper Length	1-63 cells	$6N_L$
Input Taper Length	1-63 cells	$6N_L$
Layer Half-width	3-50 cells	$4N_L$
Additional Length of BST Layers	1-63 cells	6
Source Voltage Amplitude V_0	$(1-63)\times 100$	6

Table 5.1: Optimization parameters

5.3 Initial Population and Parallel Processing

The choice of initial population size (P) involves several key trade offs: A larger initial population size results in a more complete search of the entire solution space, but after a few generations, much time may be wasted evaluating bad solutions. A smaller initial population may run faster at the expense of possibly converging to a local maximum instead of the global best solution. Research has shown an initial population of 5 to 6 times the number of bits (for a binary GA) is a good starting point [108]. This suggests an initial population of 500 to 600.

The solution time of the forward solver must also be considered. In this case, the FDTD simulation takes 20-30 minutes per solution. Sequential simulation is impractical because even a modest initial population of 50 takes $\geq$ 16 hours to complete a single generation, up to a month if 50 generations are required. Computing many of the solutions for each population in parallel using a high performance computer cluster drastically reduces the overall run time. The available computer cluster allowed direct implementation of MATLAB's `parfor` parallel execution loop across up to 80 processors. The time related to overhead communication between processors and nodes typically means a smaller number of processors is actually optimal. Typical simulations were carried out in this work using either 32 or 64 processors.

The processes of creating each new generation of child solutions tends to produce many individuals (parameter sets) that have already be simulated and have a recorded fitness value. Redundant calculation is prevented by storing a matrix of all solved individuals with their fitness values, comparing all new children against that list, and copying any previously computed fitness value. If the size of the population were matched to the available paralleled processors, all generations after the first would have numerous processors sitting idle as a result of the redundant solution check. The use of resources can be maximized by expanding the initial population size to 1.2-2 times the number of parallel processors. For the first (or first few) generations, each processor computes multiple solutions, but for each subsequent generation it becomes less likely that a processor will compute more than one unique solution. This system allows for a larger initial population size without drastically increasing the run time.

5.4 Forward Solver and Fitness Function

The FDTD simulation, covered in Chapter 4, serves as the forward solver for this problem. All solutions are simulated with an similar pulse shape, but with varying amplitude and total waveguide length. The fitness function measures the pulse compression effect of each solution. Two fitness function options were examined in this work: Pulse compression can be calculated by finding the maximum power flowing through a plane at the output of the waveguide for all time steps. Reflections and limited transmission due to impedance mismatch cause problems with this formulation. Preliminary results revealed that the GA selected solutions that minimized the amount of nonlinear BST and thus reduced reflection loss, but had no measurable rise time compression. An alternative fitness function was developed to directly measure rise time compression. Since shorter rise times result in a greater time derivative, the new fitness function given by (5.1) finds the maximum time derivative of power flowing through a plane at the output. A 5 time step moving average filter is applied to prevent noise cause by discretization error from resulting in the greatest fitness function value. Since the input voltage (and slew rate) is variable, the fitness function is normalized to the maximum time derivative of power leaving the source (10 cells away from the source).

$$f(p) = \frac{\max_{t=1:N}\left(\frac{\sum_{n=t-2}^{t+2}\frac{\partial P_f(p,x_{fit},n)}{\partial t}}{5}\right)}{\max_{t=1:N}\left(\frac{\sum_{n=t-2}^{t+2}\frac{\partial P_f(p,x_{dr}+10,n)}{\partial t}}{5}\right)} \tag{5.1}$$

In (5.1), t is the discrete time step, N is the maximum number of time steps, p is the solution number within the generation, and x_{fit} is the fitness evaluation location, which is 5 cells from the front edge of the far PML.

The nonlinear nature of these simulations makes it difficult to predict the number of time steps necessary for energy to completely propagate through a structure. For simulated structures with poor performance (little to no rise time compression), multiple reflections can lead to significant fields with the structure for tens of thousands of time steps. All simulations were thus subject to a time step limit of 5000. Simulations for structures that demonstrated significant rise time compression were truncated 300 times steps after the peak of the pulse had passed through the output evaluation plane. For many solutions, this operation reduced the number of time steps to less than 3500, resulting in significant reduction in computaional time.

5.5 Ranking and Retention

All individuals in the population are ranked by their fitness value. The process of crossover and mutations creates a possibility that the best individual (highest fitness value) from the current generation is lost in the creation of the next generation. To avoid this situation, an operation known as 'elitism' directly copies the best individual to the next generation without mutation.

5.6 Selection

After the population has been ranked, 'parent' solutions from the current generations must be selected to create the next generation through crossover. The top 10% of solutions are directly selected to insure the next generation shows strong influence from the best solutions. The roulette wheel method selects the remaining parents. In this method, each solutions fitness value represents it's effective density on a roulette wheel. The sum of all fitness values (for the present generation) gives the total size of the wheel, as given by (5.2).

$$W_{total}(p) = \sum_{p=1}^{P} f(p) \tag{5.2}$$

Each solutions fitness values is divided by the wheel size, giving the portion of the wheel that each solution occupies, as given by (5.3). The cumulative sum of these values produces a vector of index points between 0 and 1, as given by (5.4).

$$W_{weights}(p) = \frac{f(p)}{W_{total}} \tag{5.3}$$

$$W_{index}(p) = \sum_{1}^{p} W_{weights}(p) \tag{5.4}$$

For each parent solution to be selected, a random number between 0 and 1 is generated and subtracted from the index array W_{index}. The absolute value of this result gives the absolute numerical distance from the random number to each point in the index array. The MATLAB `min` function applied to this result finds the index closest to the random number. This index identifies the selected parent. The process repeats until P parents are selected.

5.7 Crossover

Each pair of selected parent solutions create two child solutions. Crossover of genes from the parents occurs probabilistically, with a rate of 60% selected for this work. If crossover is not selected, the genes are copied directly from parent 1 to child 1 and from parent 2 to child 2. If the crossover process is selected, a random integer crossover point x_{cross} is generated from 1 to the total number of genes N. The crossover operation is carried out as given by (5.5), with the genes in binary form and the gene indicies given in parentheses.

$$\begin{aligned} Child_1 &= [Parent_1(1 : x_{cross})\ Parent_2(x_{cross} + 1 : N)] \\ Child_2 &= [Parent_2(1 : x_{cross})\ Parent_1(x_{cross} + 1 : N)] \end{aligned} \tag{5.5}$$

5.8 Mutation

All child solutions, except for the 'elite' solution from each generation, are subject to probabilistic mutation or bit flipping. The mutation process helps ensure coverage of the entire solution space and helps avoid local maximum trapping. A series of nested `for` loops steps through each bit of each child solution. For each bit, if a randomly generated number between 0 and 1 is less than the mutation rate, that bit will be flipped. A mutation rate of 2% was selected for this work.

5.9 Termination Conditions

The termination of the GA cannot be predetermined due to the complexity of the problem and the probabilistic operations. However, apparent convergence can be determined by tracking the best solution over multiple generations. In this work, the GA is terminated when no better solution (higher fitness value) has been found after 10 consecutive generations. Because access time on the computer cluster is limited, a hard limit of 50 generations is also imposed.

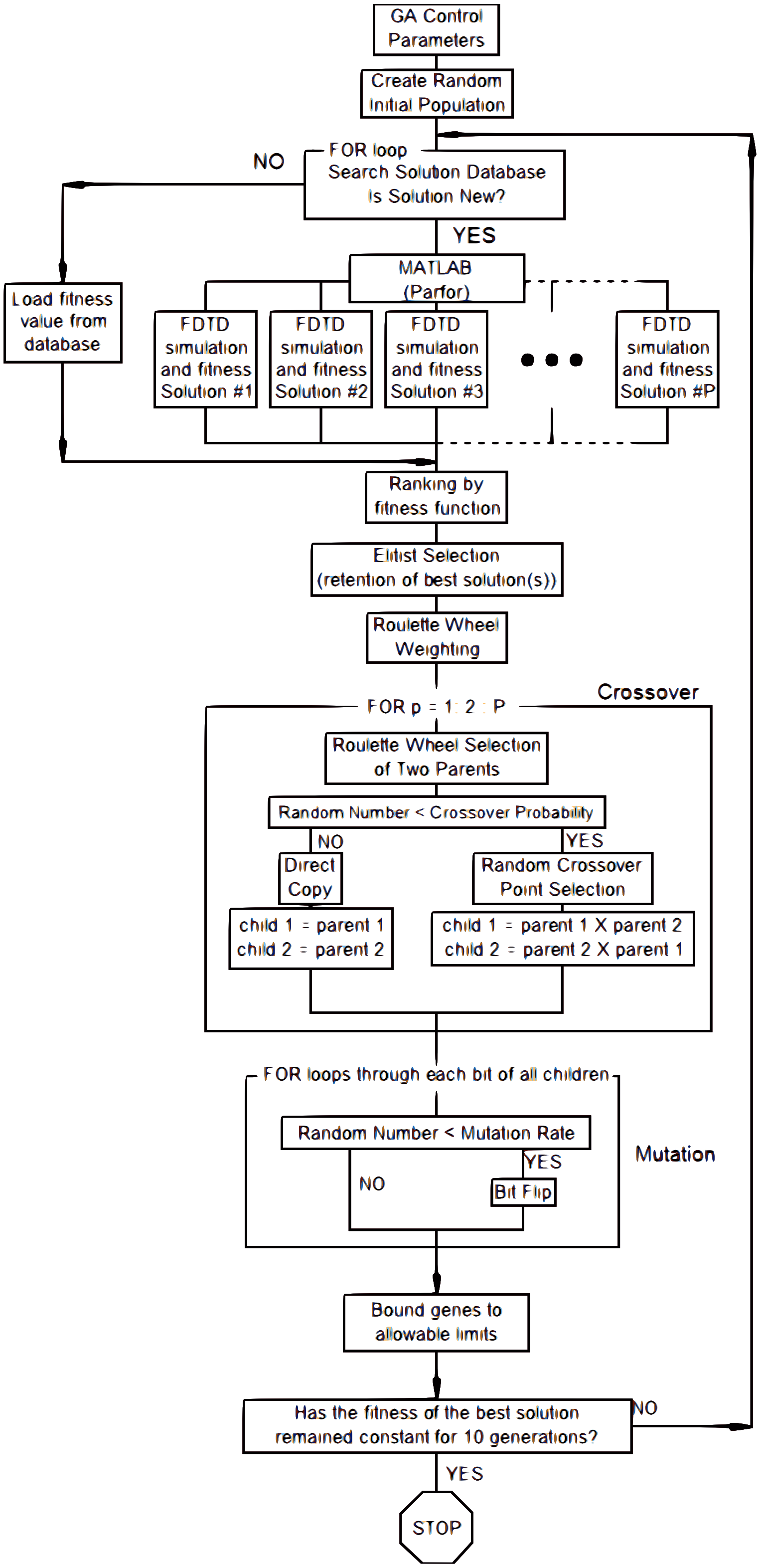

Figure 5.3: Detailed flow chart for genetic algorithm

Chapter 6

Simulation Results

Initial simulations with the GA used 5 layers of BST ($N_L = 5$), where the GA was allowed to control the material option for each layer independently. Observations of fields from the best solution revealed that only a single layer was causing the dominant pulse observed at the output. Since the different material options have a wide range of low-field permittivity (59-173) and thus a wide range of propagation velocity, the waves propagating through each layer arrive at the output at different times. The layer with highest low-field permittivity and greatest tunability was driven furtherest into the nonlinear polarization region, and thus had greatest compression and produced the large peak flowing power at the output. All other layers had lower peak flowing power, if compression was even present at all. This result suggests that multiple layers with different material properties would not be beneficial over a simpler structure. Additionally, the large spatial domain required for multiple layers caused very long run times. As a result, the GA was halted by run time limits on the computer cluster before a sufficient number of generations had been computed.

6.1 Simulation Cycle 1

A single central layer, with the GA selecting the material, input and output taper lengths, width, added central length and pulse amplitude, was then considered. Figure 6.1 shows the fitness function of the best solution after each generation. Though the GA terminated on the maximum number of generations before reaching a converged state, the rate of change in the best fitness function was small for the last 9 generations.

The structure of the best solution at the GA termination is shown in Figure 6.2 and is given by the parameter is Table 6.1. Limits set to prevent single cell widths of BST at the

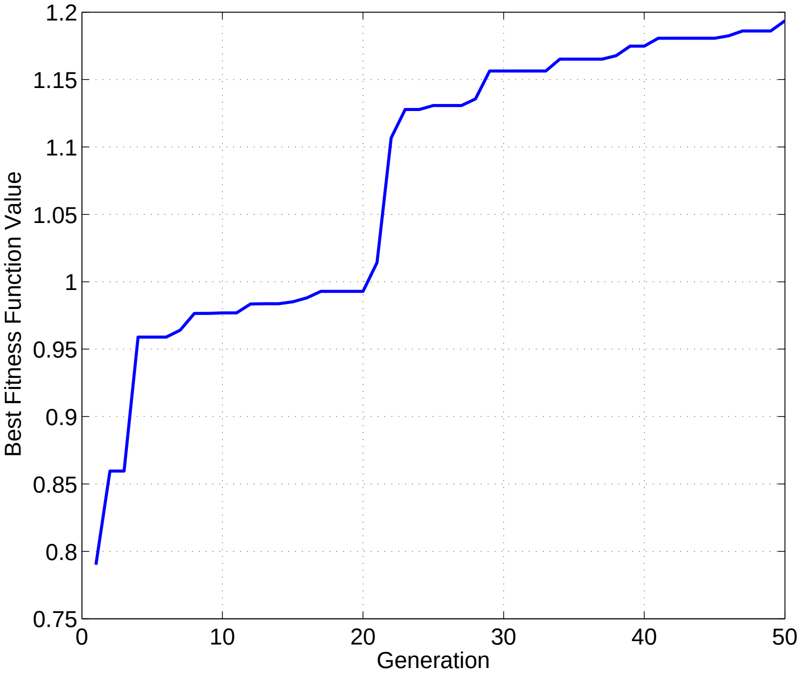

Figure 6.1: Simulation cycle 1: Best fitness function for each generation

tips of the input and output tapers reduced the actual length of the tapered sections by 15 cells. While a large number of cells were used in the propagation dimension ($\hat{x}$), the thin structure is coarsely represented in the transverse dimension ($\hat{z}$), as shown by Figure 6.3. Power flowing through input and output planes (as defined in Figure 6.2) is shown in Figure 6.4 and the spectral content shown in Figure 6.5. Analysis of input and output rise times (10% to 90%) shows rise time compression of 58.4%. The conversion of propaging energy to heat within the BST, due to the large loss tangent, is evident from Figure 6.6.

Parameter	Gene Value	Physical value
Material	2	$x = 0.47$, $\varepsilon_r(\lvert\mathbf{E}\rvert = 0) = 147.2$
Input Taper	55 cells	3.1* mm
Output Taper	63 cells	3.6* mm
Total Width (2×Half-width)	6 cells	342 μm
Added length	1 cells	57 μm
Pulse amplitude	63	6300 V
Fitness function	1.1936	
τ_{rise} input (10%-90%)	15.4 ps	
τ_{rise} output (10%-90%)	6.4 ps	
% Compression	58.4%	
Input energy	3.77 mJ	
Output energy	1.65 mJ	
Generations	50	
Processors	64	
GA Run Time	20.17 hours	
*Actual length reduced by limits that preventing single cell width structures		

Table 6.1: Simulation cycle 1: Genetic algorithm simulation results

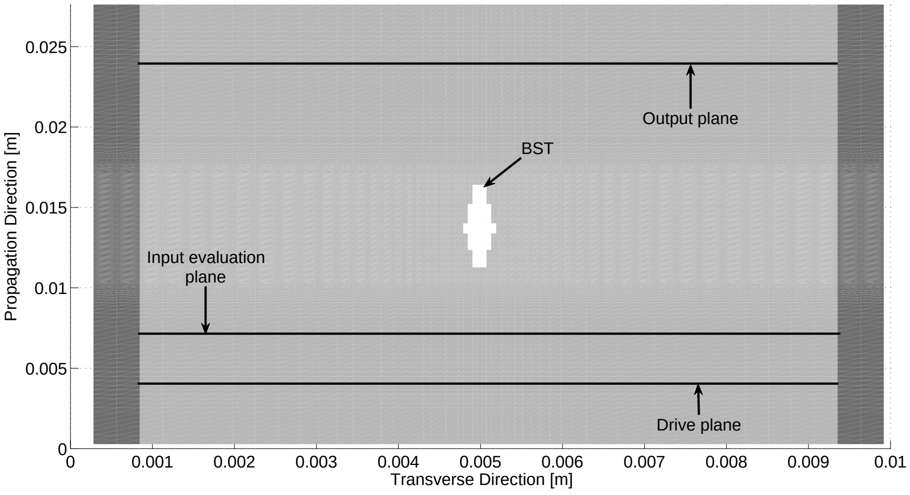

Figure 6.2: Simulation cycle 1: Optimized structure, top view

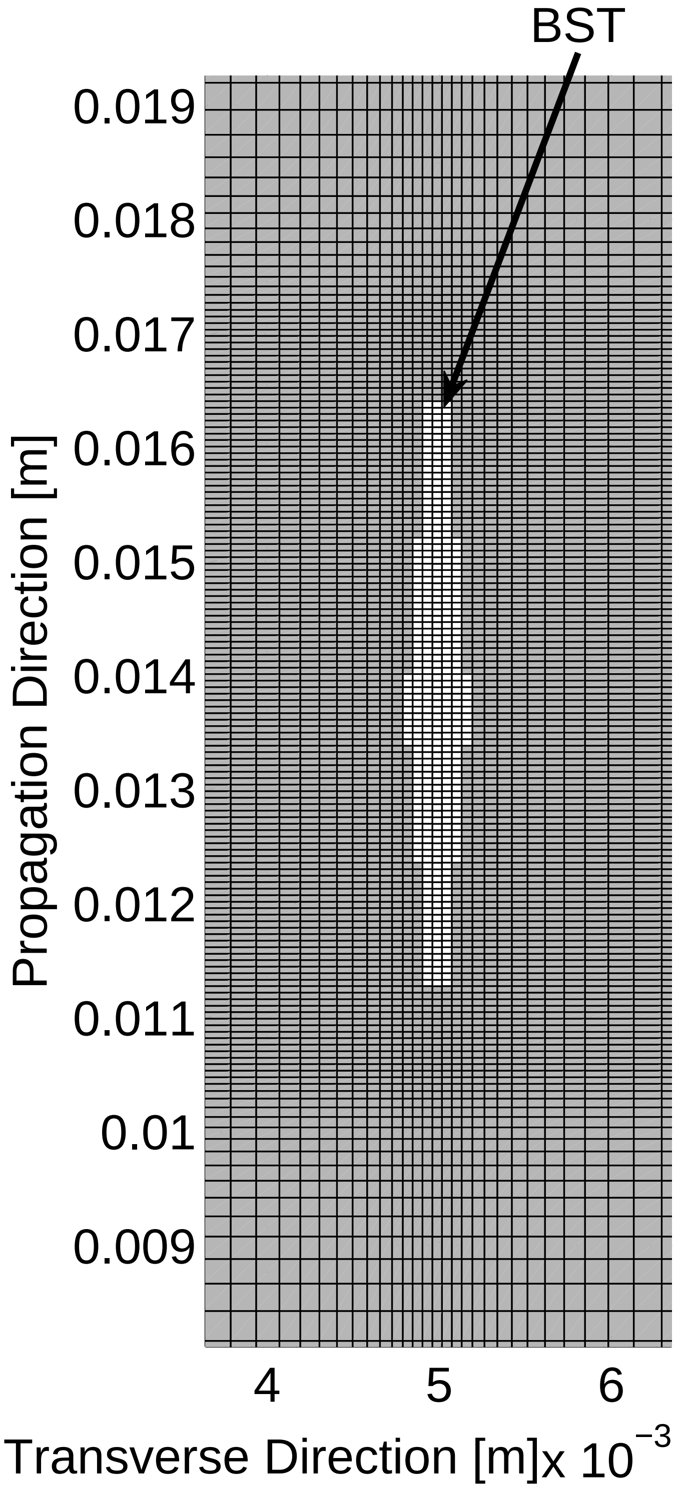

Figure 6.3: Simulation cycle 1: Structure detailed top view

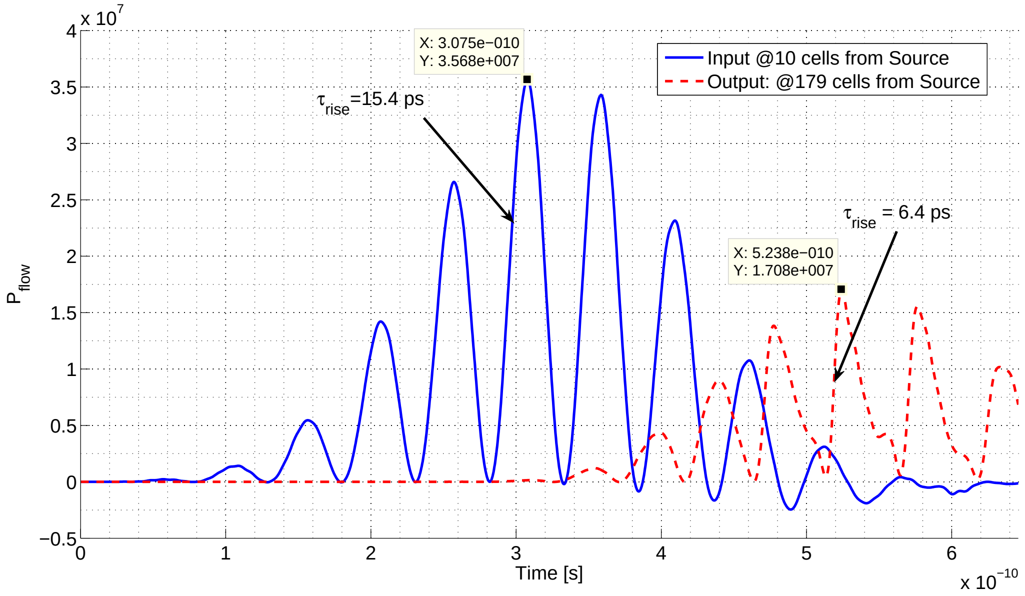

Figure 6.4: Simulation cycle 1: Input and output flowing power

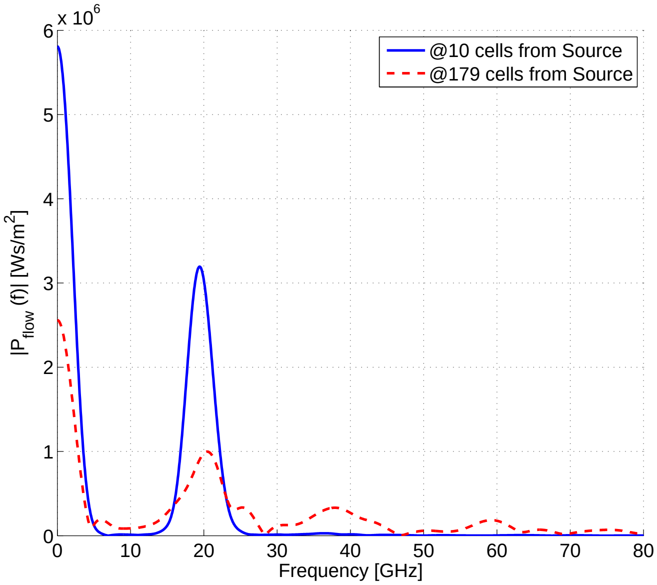

Figure 6.5: Simulation cycle 1: Input and output flowing power spectrum

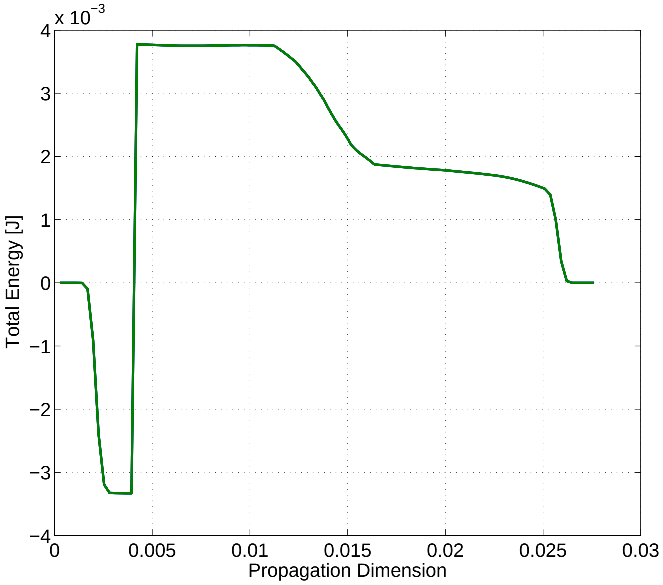

Figure 6.6: Simulation cycle 1: Total energy within the waveguide for all time

While the fitness function in this work only considers the overall rise time compression, it is interesting to note that a local examination of the poynting vector (P_x) shows localized increased power density both within the BST and within the LTCC as the wave exits the BST. This is shown in Figure 6.7, along with the initially elliptical wavefront that propagates away. Further reduction in rise time may be possible using changes to the SIW structure (width, height, etc.) to take advantage of the localized increase in energy and\or the elliptical wavefront.

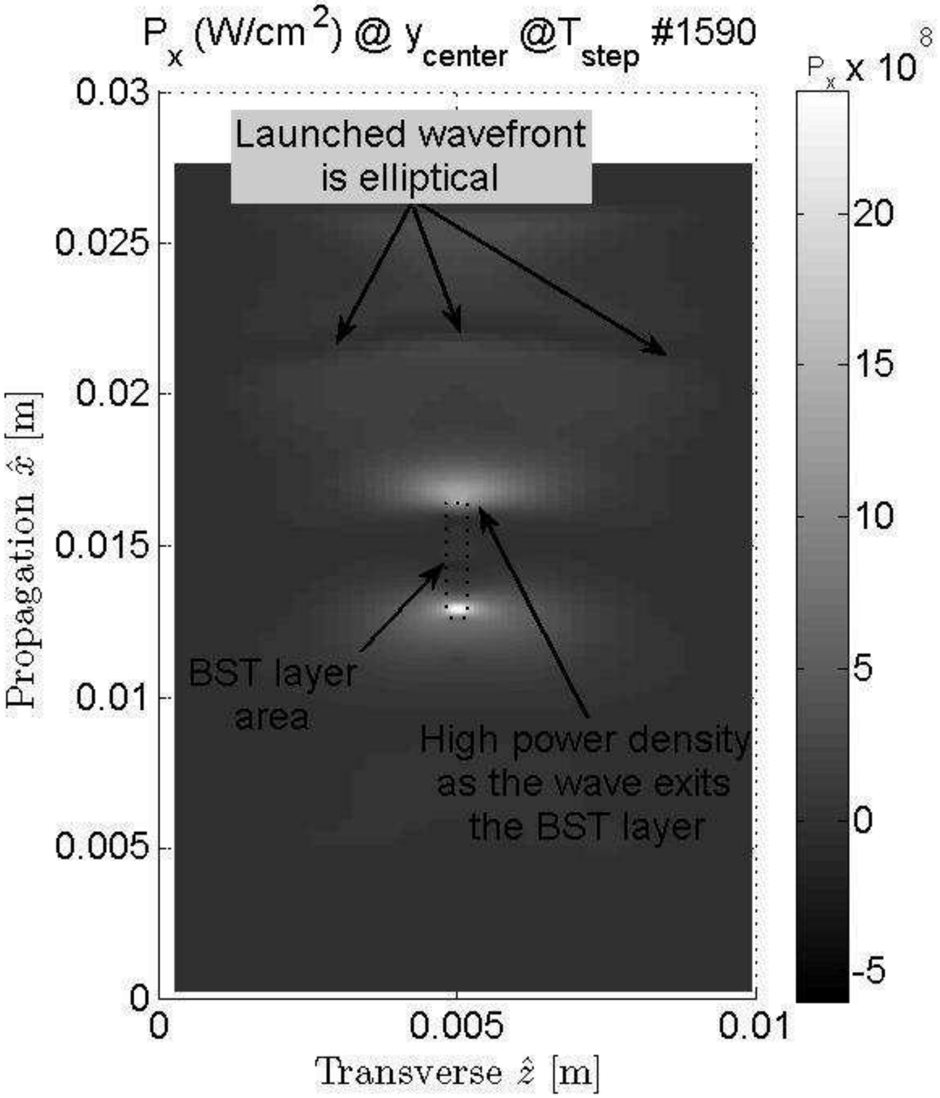

Figure 6.7: Simulation cycle 1: Planar cut of poynting vector

6.2 Simulation Cycle 2

Some the parameters of the best solution from simulation cycle 1 were at the maximum value allowed within the GA, which suggests expanding the range of allow values might yield better rise time compression. One additional bit was added for genes controlling input taper length, output taper length, added central length and voltage, thus allowing these parameter to take on values between 1 and 127. Additional, the structure width in simulation cycle 1 was small, resulting in a relatively coarse stair-stepping approximation of the input and output taper sections. This observation suggests a smaller minimum cell size (lattice spacing) might yield better results. For simulation cycle 2, the cell size was reduced by a factor of 2, such that $\Delta_{min} = \lambda_{min}/20$, considering the same maximum frequency of interest. The time step was reduced accordingly and the source pulse was adapted to insure the same band-limited spectral content of the source pulse. The increased spatial resolution also required a smaller window of 8 times steps for the moving average operation discussed in Section 4.2. All other parameters were unchanged from simulation cycle 1.

The much larger spatial domain (total number of cells) and greater number of required time steps resulted in much longer simulation times for each solution. The GA was halted at 17 generations based on access time limitations on the computer cluster; however, the best solution fitness function value had remained constant for the last 7 generations. The results for simulation cycle 2 are shown in Table 6.2.

Parameter	Gene Value	Physical value
Material	1	$x = 0.5$, $\varepsilon_r(\lvert\mathbf{E}\rvert = 0) = 173$
Input Taper	66 cells	1.9^{*1} mm
Output Taper	6 cells	0.171^{*1} mm
Total Width (2×Half-width)	70 cells	2 mm
Added length	43 cells	1.2 mm
Pulse amplitude	46	4600 V
Fitness function	2.3225	
τ_{rise} input (10%-90%)	15.4 ps	
τ_{rise} output (10%-90%)	2.4^{*2} ps	
% Compression	84.4%	
Input energy	1.5 mJ	
Output energy	0.271 mJ	
Generations	17^{*3}	
Processors	64	
GA Run Time	50 hours^{*3}	
^{*1}Actual length reduced by limits that preventing single cell width structures		
^{*2}Output rise time was extrapolated for the portion of the pulse with largest positive time derivative, as shown in Figure 6.11		
^{*3}GA halted after 17 generations due to access time restrictions on computer cluster		

Table 6.2: Simulation cycle 2: Genetic algorithm simulation results

The structure of the best solution, as shown in Figure 6.8, is much wider than the structure in simulation cycle 1. The wider structure appears to give rise to a more complex higher-order hybrid mode (multiple half-sine variations). Figure 6.9 shows the Poynting vector (P_x) patterns of wave compression within the BST and the launching of these compressed waves out of the BST. Power flowing through input and output planes (as defined in Figure 6.8) is shown in Figure 6.10 and the spectral content shown in Figure 6.12. Output rise time was difficult to measured due to the complexity of the output power vs. time signature. An equivalent 10% to 90% rise time was calculated at 2.4 *ps* based on an linear extrapolation, as shown in Figure 6.11. This estimate results in a rise time compression of 84.4%. While greater rise time compression is achieved, it comes at the cost of greater reflection of the input energy and higher dielectric losses. Energy loss from input to output (neglecting reflections) is estimated at 82%.

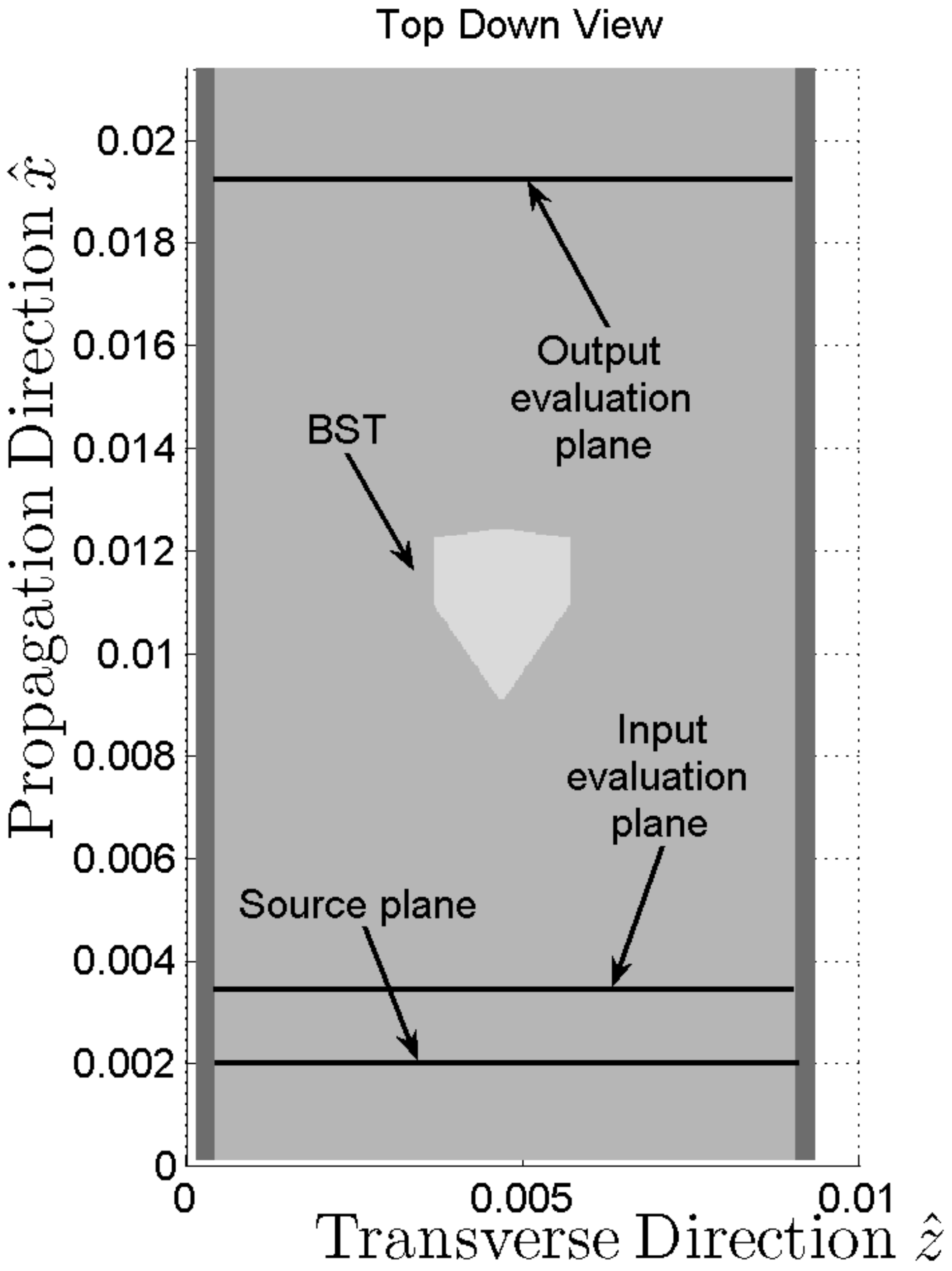

Figure 6.8: Simulation cycle 2: Optimized structure, top view

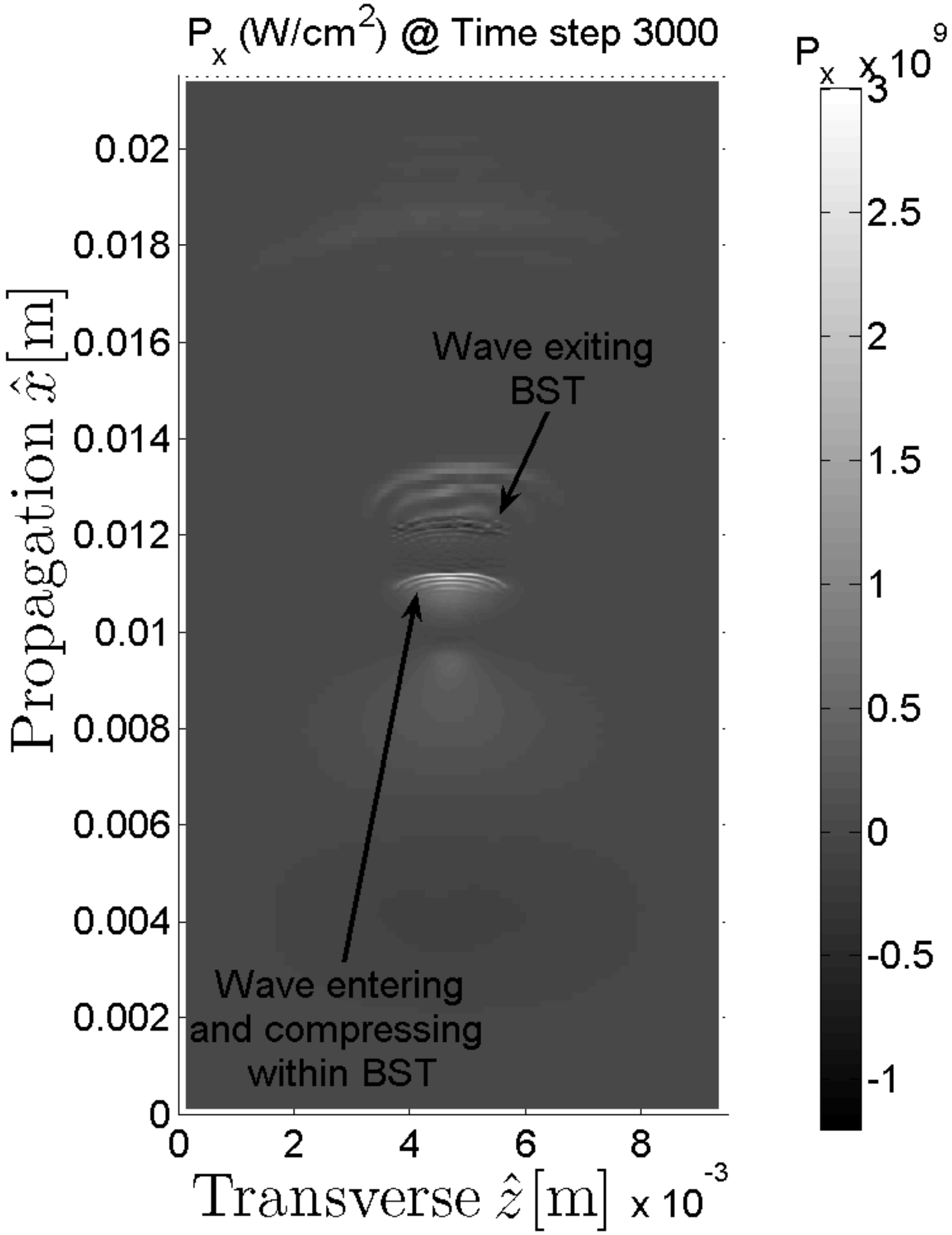

Figure 6.9: Simulation cycle 2: Planar cut of poynting vector at SIW center (vertical)

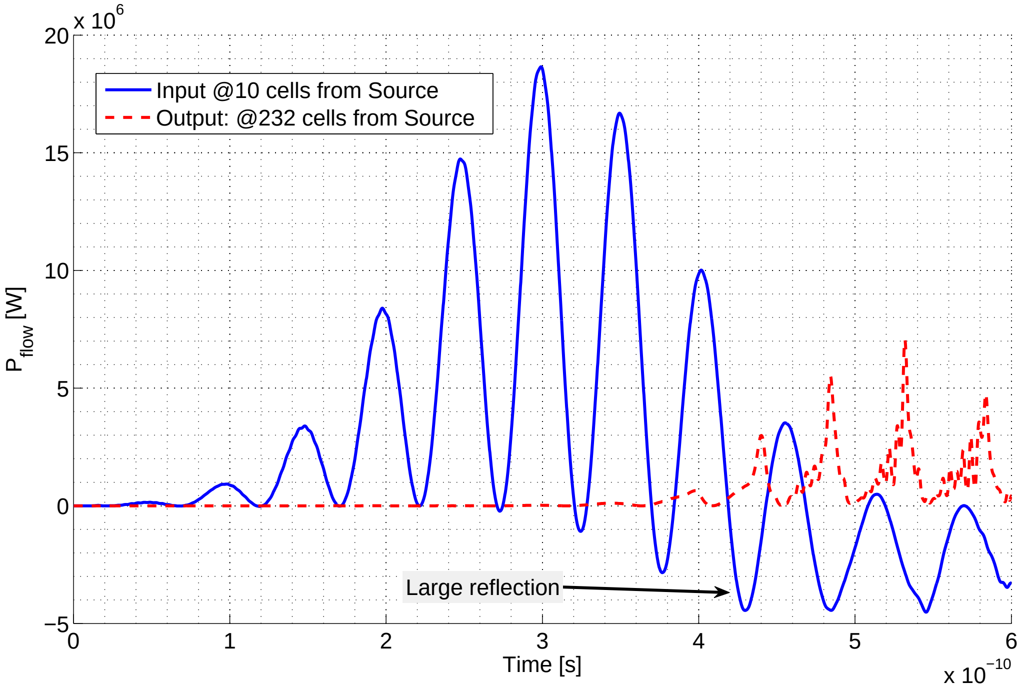

Figure 6.10: Simulation cycle 2: Input and output flowing power

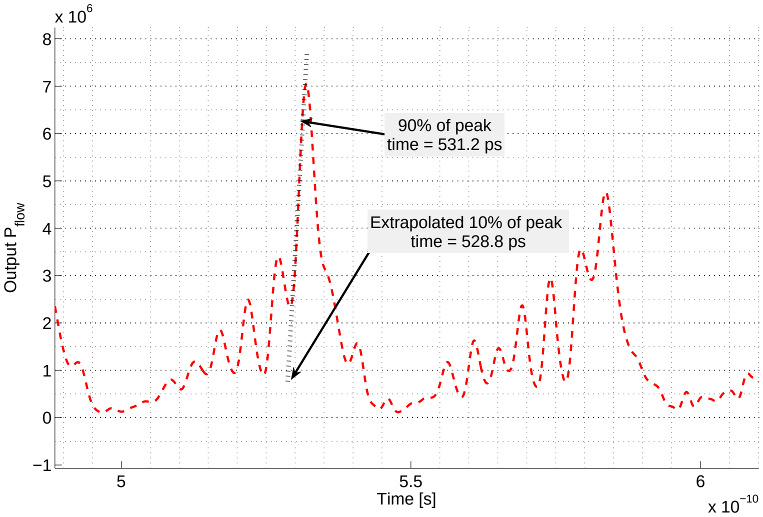

Figure 6.11: Simulation cycle 2: Output rise time calculation detail

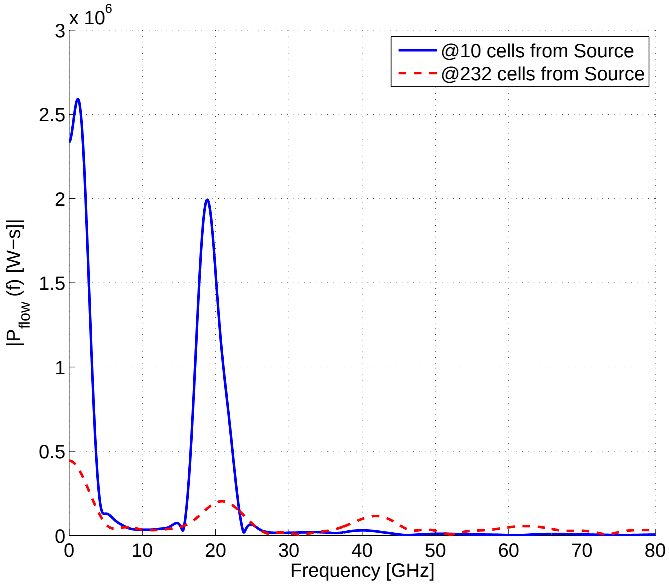

Figure 6.12: Simulation cycle 2: Input and output flowing power spectrum

Chapter 7

Fabrication Process

The presented design of this work was based on fabrication compatibility in LTCC. At the time of defense of this work, funding was not available to proceed with full fabrication. A simple linear SIW was constructed and tested in LTCC as discussed in Chapter 8. The following sections detail the fabrication process and anticipated challenges, should funding become available for complete fabrication.

7.1 LTCC Fabrication

An LTCC circuit board begins as a proprietary ceramic slurry of crystallizable glass, alumina, and volatile solvent. This slurry is tape cast into sheets onto a carrier film. Holes are mechanically punched through the sheets to form vias. A screen printing process fills the vias with metal (silver or gold) and prints traces and/or planes on top of the sheets. Because shrinking occurs during the firing process due to the remove of the volatile solvent, the metal pastes used for printing must be matched to the shrinkage factor of the ceramic. The vias, traces and planes make up integrated components such as resistors, capacitors, inductors and transmission lines. The integrated components and the raw (unfired) sheets are stacked and fired together (known thus as 'co-fired'). Each type of LTCC material has a specific firing time-temperature profile that is designed to achieve the best properties in terms of structural strength and low dielectric loss. Once a complete circuit design or transmission line layout has been simulated, it must be translated to individual layer layouts for fabrication in LTCC. A software package such as Agilent Technologies Advance Design System (ADS) is well suited for this task.

Dielectric Permittivity ε_r	7.1
Loss Tanget	0.001 @ 9 GHz
Unfired layer thickness	5 mils (104) μm
x-y (in plane) shrinkage	9.1% ±0.3%
z (layer height) shrinkage	11.8% ±0.5%
Typical maximum board size	8in. x 8in.
Typical maximum number of layers	20

Table 7.1: Properties of DuPont® GreenTape® 9k7 [12]

The LTCC chosen for this work was DuPont® GreenTape® 9k7. Key properties of interest to this work are given in Table 7.1. In this work, the SIW can be fabricated using periodically spaced vias as the side walls and metalized planes as the top and bottom walls. Overlapping the punched vias can be used to from arbitrary shaped cavities [109], such as the regions to be filled with BST as specified by this work. These cavities or trenches will have a jagged edge due to the nature of overlapping circular punched vias. The bottom wall, sidewall vias and cavities can all be fabricated in the unfired tape layers, but the microstrip lines, input\output tapered traces and top SIW wall can only be screen printed after the cavities are filled with BST.

7.2 Sol-gel Process

While a number of methods exist and have been tested for the deposition of BST onto substrates, the solvent-gel or sol-gel process is believed to be the best fit for this design. Methods such as Metal Organic Chemical Vapor Deposition (MOCVD) and RF sputtering were considered, but these methods are best suited for forming precisely controlled thin layers. Forming the bulk layers of this design would be impractical in terms of time and cost.

The sol-gel process works by deposition of solvent-suspended precursor particles onto a substrate that is then heated to drive off (pyrolyze) the solvent, leaving only the desired particles. An example of this process for BST as used by Lahiry et al. [110] is described here: Barium-ethylhexanoate and strontium-ethyl-hexanoate are combined in an ethanol solution by mole fraction to control the BST ratio. Titanium(IV)-isopropoxide is then added stoichiometrically to the solution. A small amount of acetone and formamide are added to improve the stability of the solution and limit the rate of pyrolysis respectively. The final solution is filtered and then applied to a substrate (such as platinum coated silicon) using a spin coating system. The coated substrate is heated to $350°C$ to pyrolyze the ethanol solvent. On planar substrates, this process forms very thin layers ($< 0.2\mu m$), but thicker structures can be fabricated by repeating the spin coat and heating process. The cavities created for this design should trap the solution and form thicker layers much faster.

Once the desired thickness is achieved, a final heat treatment is applied to sinter the precursor particles together. In the work by Lahiry et al., this sintering was carried out at between $500 - 700°C$, although other studies suggest much a higher temperature ($1100°C$ in [73] and $1300°C$ in [69]) results in a better crystalline structure and subsequently higher permittivity and tunability. This may pose some challenges to forming high performance BST layers in LTCC, which are typically limited to firing (or refiring) temperatures of $< 950°C$ due to the melting point of silver metalization. Valant and Suvorov [89] examined this problem and found the addition of a small amount ($< 1wt\%$) of Li_2O reduced the sintering temperature to $900°C$ while maintaining good tunability. As an added benefit, the shrinkage rate of the applied BST is reduced to rate similar to that of the LTCC. Palukuru et al. [111] used this method to fabricate a thick-film screen-printed phase shifter on LTCC that achieved 34% tunability at $5V/\mu m$. Tick et al. [112] also considered the LTCC constraints and found pressure assisted sintering to successfully produce high quality BST films.

7.3 Testing

Testing of any fabricated design would require a control case, such as a standard microstrip line and a standard linear SIW of identical length to the nonlinear SIW. These structures allow confirmation of the microstrip, transition, and SIW designs. The microstrip lines on LTCC can be connected to test equipment with solder-on SMA or 2.4mm test connectors, such as Amphenol® #132343 [113]. Given the anticipated high frequency content of the output pulse, the 2.4mm connector with $F_{max} = 50GHz$ would likely be the best choice. Traditional tests such as S-parameter testing are useful for standard SIW structures, but are not significantly applicable for the presented design, since these parameter are dependent on input amplitude. Additionally, driving the BST into the nonlinear region requires higher voltages than commonly available from an S-parameter test set. Instead, a pulsed microwave source or switched capacitor voltage pulse could be used to the feed the structure and the output measured with a high-frequency oscilloscope or time domain reflectometer. Rise time compression can be measured by comparing time-shifted input and output voltage waveforms. Parasitic reactance must be kept to a minimum to avoid having the apparent rise time reduced by the measurement equipment.

Chapter 8

Basic Fabricated SIW

A simple linear SIW was designed and fabricated for X-band operation ($f_{c_{10}} = 6.56\ GHz$) in 8 layers of DuPont® GreenTape® 9k7 LTCC using silver metalization. The design included the tapered microstrip transitions as discussed in section 2.2.3, and shown in Figure 8.1. The tapered transitions are $3\lambda_{LTCC}/4$ at 10 GHz. The structure was simulated before fabrication using HFSS to confirm proper design. Figures 8.2 and 8.3 show the simulated reflection coefficient (S_{11} and S_{22}) and insertion loss (S_{21} and S_{12}) respectively. As expected, a passband is observed from $\sim 8 - 10.25\ GHz$ where $S_{11} \leq -15\ dB$ and $S_{21} \geq -0.6\ dB$. The microstrip taper transition is most likely the limiting factor on the bandwidth of the passband. The results are also in agreement with the validation study of the FDTD code given in appendix B.

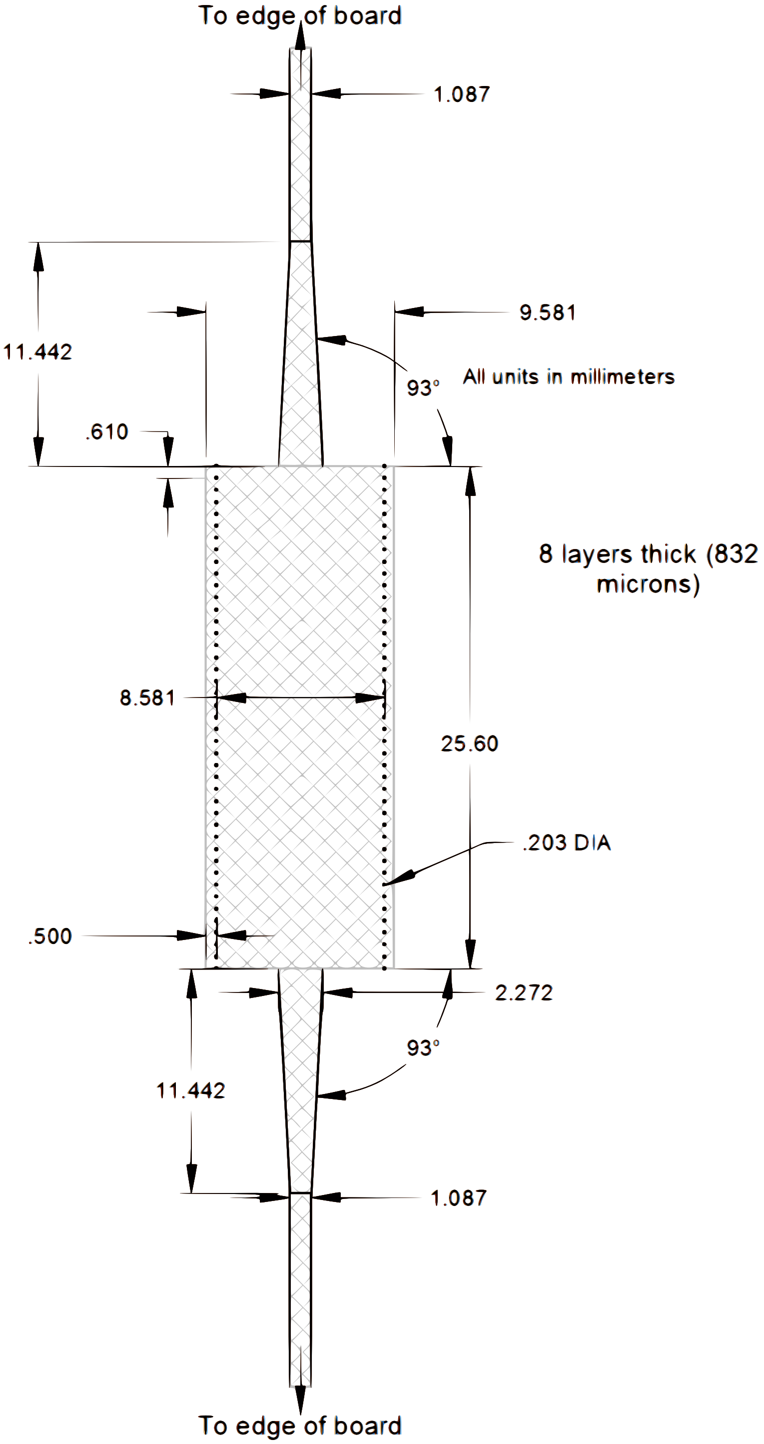

Figure 8.1: Standard SIW and feed structure layout for 8 layers of LTCC

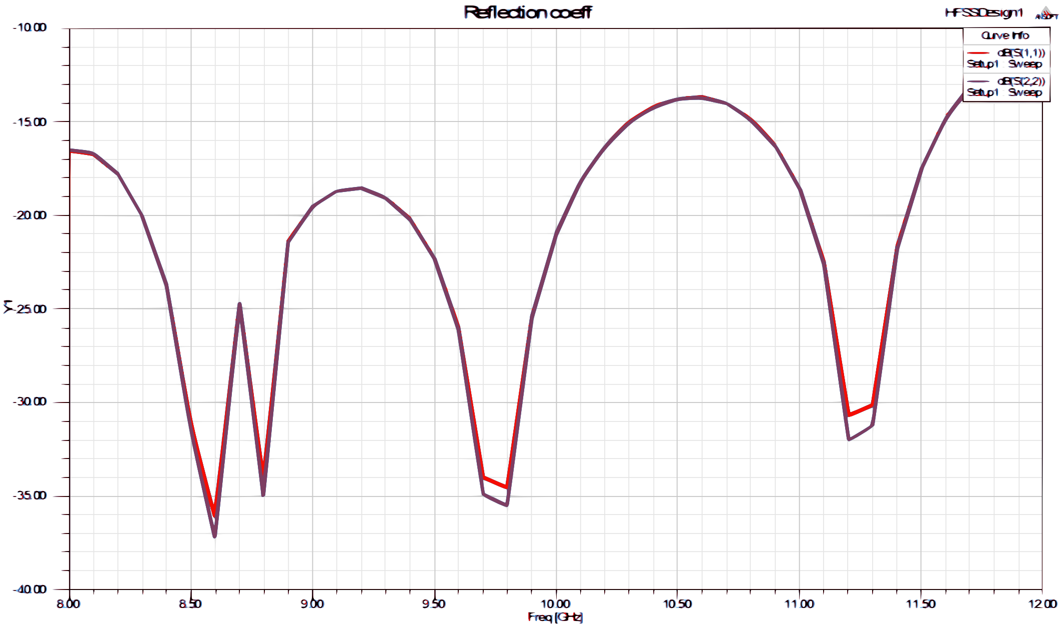

Figure 8.2: Simulation of fabricated standard SIW: S_{11} vs. frequency

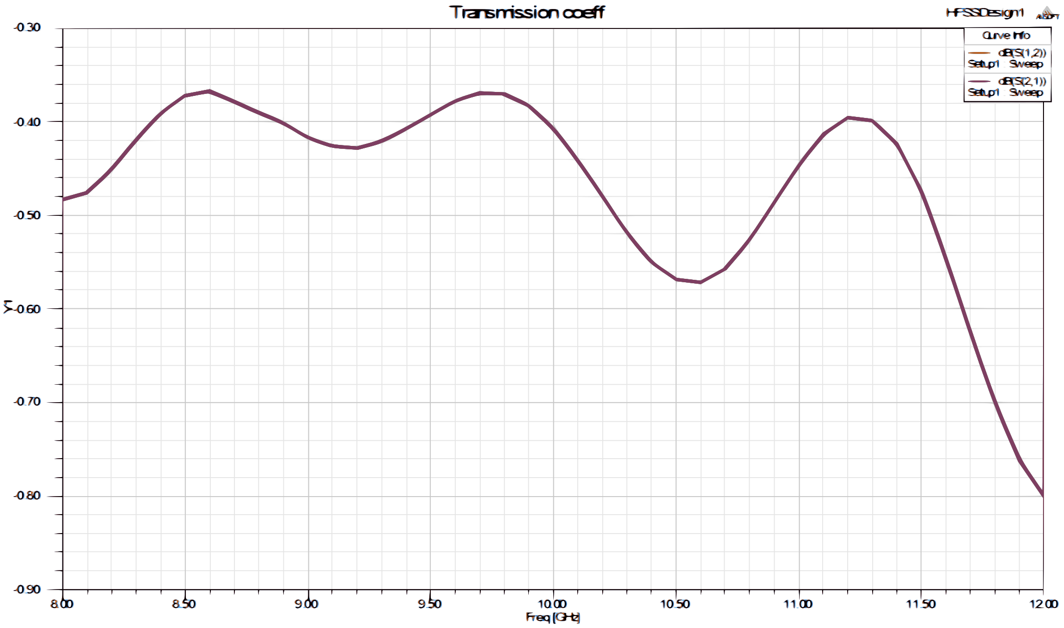

Figure 8.3: Simulation of fabricated standard SIW: S_{21} vs. frequency

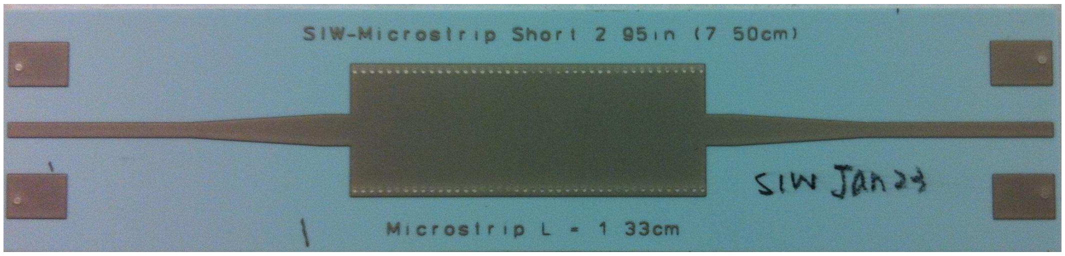

Figure 8.4: Fabricated standard SIW

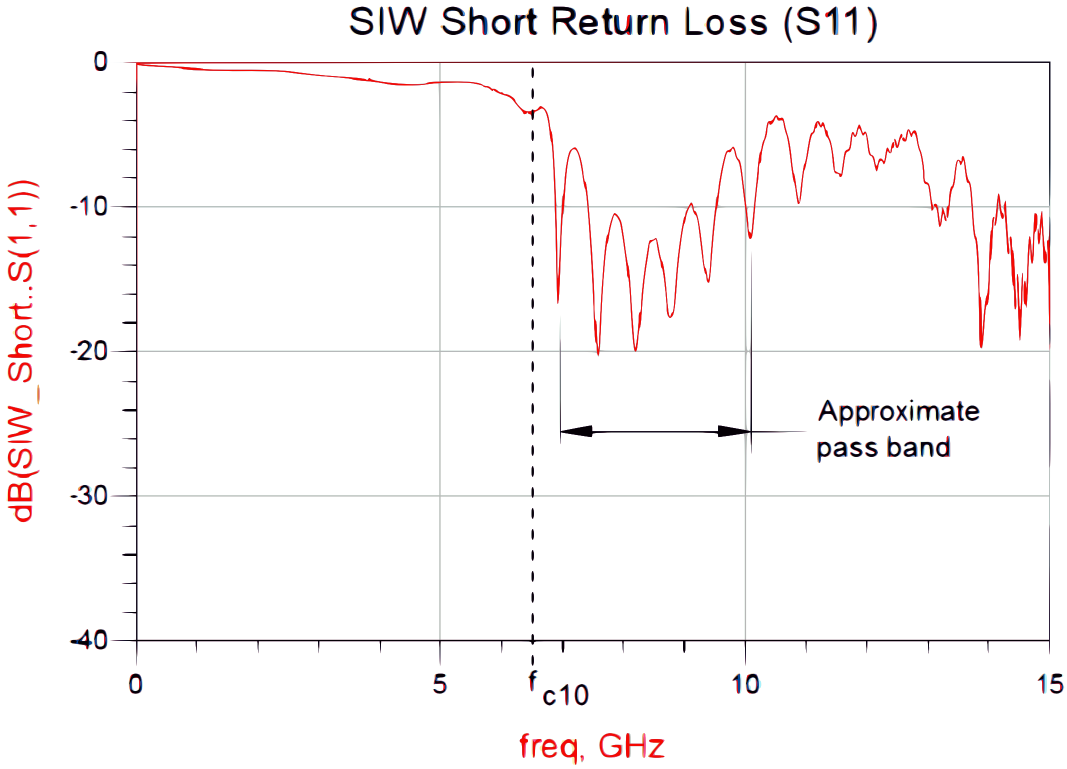

Figure 8.5: Fabricated standard SIW: S_{11} vs. frequency

A picture of the fabricated structure is given in Figure 8.4. SMA edge connectors were soldered to the microstrip lines for connection to a two-port vector network analyzer. Figures 8.5 and 8.6 show the measured S_{11} and S_{21} parameters respectively. The cutoff frequency is observable by the rapid drop in S_{21} below $\sim 6.8GHz$, and the waveguide clearly acts as a high pass filter. A flat pass band where $|S_{21}| \leq\sim 3\ dB$ can be observed from $7-10\,GHz$. While the cutoff frequency and passband range are in good agreement with the simulations, the losses are greater. The additional loss is most likely due to the end-launch SMA connectors which were not included in the simulation.

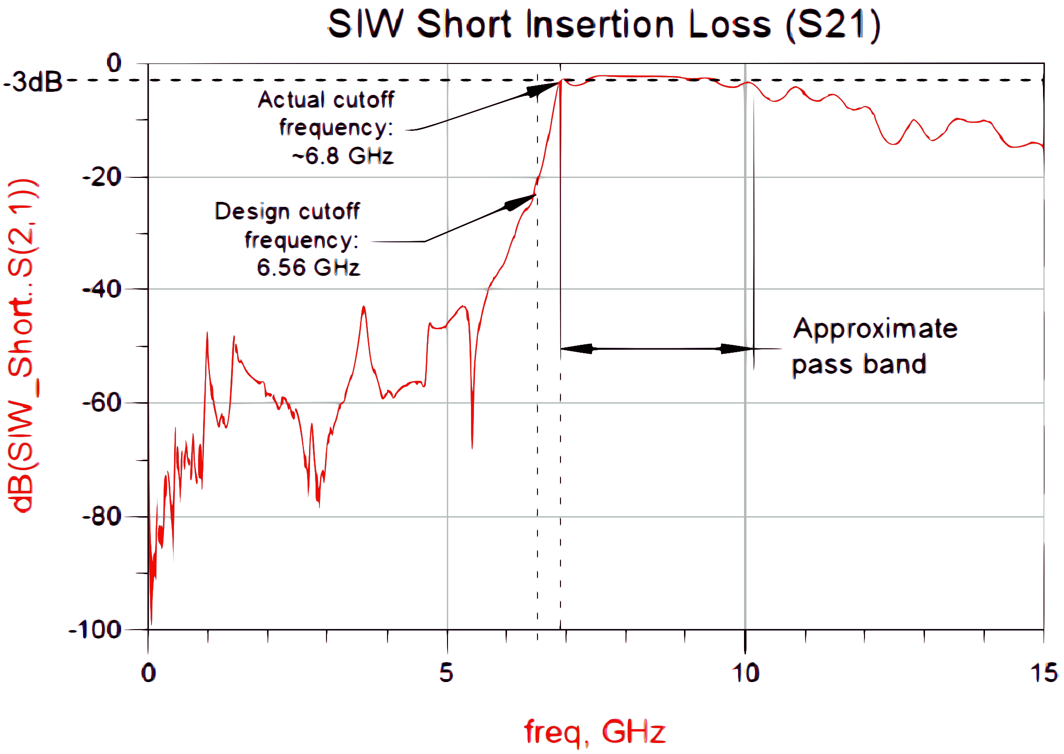

Figure 8.6: Fabricated standard SIW: S_{21} vs. frequency

Chapter 9

Conclusions

This work has presented an new form of pulse compression device based on nonlinear ferroelectric materials in a substrate integrated waveguide. The design operates based on the nonlinear permittivity of the ferroelectric material BST. A GA with a nonlinear three-dimensional FDTD forward solver was used to find the optimal structure, material and input voltage to produce maximum rise time compression. The rise time of the optimized solution is reduced from the input at 15.4 ps to the output at 6.4 ps, for a compression of 58%. Significant broadening of the pulse spectrum including the generation of higher order harmonics was also observed. High loss within the BST resulted in the loss of 57% of input energy to heating. A second simulation cycle with finer lattice spacing found greater compression could be achieved (84%) with wider structure, but at the cost of much higher losses (82%). The GA implemented on a computer cluster provided an efficient means of finding the optimal solution given the complex trade-offs involved.

Several challenges were encountered during the course of design work: First, simulating nonlinear structures in three-dimensions with good accuracy requires fine spatial division and as such, long run times. Applying advances in the FDTD implementation, such as graphics processor unit (GPU) programming, has the potential to drastically reduce run times. A shorter incremental run time (run time per cell per time step), would allow for more complex geometries to be studied in a reasonable time. Next, input and output coupling between the BST and LTCC has proven difficult due to the large impedance mismatch. A lower permittivity ferroelectric material using dopants was shown to be beneficial for solving this problem. However, this option comes with a significant reduction in tunability and thus requires higher field strength to drive the material into deep polarization saturation when compared to pure BST. Lastly, limited data is available on BST characterization in bulk form using high field strength AC signals. Design of a ferroelectric nonlinear transmission line will become simpler as more accurate models of BST under varying conditions become available.

Bibliography

[1] G. Branch and P. W. Smith, “Fast-rise-time electromagnetic shock waves in nonlinear, ceramic dielectrics,” *Journal of Physics D: Applied Physics*, vol. 29, no. 8, pp. 2170–2178, Aug. 1996. [Online]. Available: http://iopscience.iop.org/0022-3727/29/8/017

[2] J. E. Dolan, “Simulation of shock waves in ferrite-loaded coaxial transmission lines with axial bias,” *Journal of Physics D: Applied Physics*, vol. 32, no. 15, pp. 1826–1831, Aug. 1999. [Online]. Available: http://iopscience.iop.org/0022-3727/32/15/310

[3] P. Stenius and B. York, “On the propagation of transients in waveguides,” *IEEE Antennas and Propagation Magazine*, vol. 37, no. 2, pp. 39 –44, Apr. 1995.

[4] D. Deslandes and K. Wu, “Accurate modeling, wave mechanisms, and design considerations of a substrate integrated waveguide,” *IEEE Transactions on Microwave Theory and Techniques*, vol. 54, no. 6, pp. 2516 –2526, Jun. 2006.

[5] T.-H. Yang, C.-F. Chen, T.-Y. Huang, C.-L. Wang, and R.-B. Wu, “A 60GHz LTCC transition between microstrip line and substrate integrated waveguide,” in *Microwave Conference Proceedings, 2005. APMC 2005. Asia-Pacific Conference Proceedings*, vol. 1, Dec. 2005, p. 3 pp.

[6] F. Taringou and J. Bornemann, “New substrate-integrated to coplanar waveguide transition,” in *Microwave Conference (EuMC), 2011 41st European*, Oct. 2011, pp. 428 –431.

[7] D. Deslandes, “Design equations for tapered microstrip-to-substrate integrated waveguide transitions,” in *Microwave Symposium Digest (MTT), 2010 IEEE MTT-S International*, May 2010, pp. 704 –707.

[8] O. G. Vendik and S. P. Zubko, “Ferroelectric phase transition and maximum dielectric permittivity of displacement type ferroelectrics (BaxSr1xTiO3),” *Journal of Applied Physics*, vol. 88, no. 9, pp. 5343–5350, Nov. 2000. [Online]. Available: http://jap.aip.org/resource/1/japiau/v88/i9/p5343_s1

[9] G. A. Smolenskii and V. A. Isupov, “Segnetoelektricheskie svoistva tverdykh rastvorov stannata bariya v titanate bariya,” *Zhurnal Tekhnicheskoi Fiziki*, vol. 24, pp. 1375–1386, 1954.

[10] X. Wei and X. Yao, “Nonlinear dielectric properties of barium strontium titanate ceramics,” *Materials Science and Engineering: B*, vol. 99, no. 13, pp. 74–78, May 2003. [Online]. Available: http://www.sciencedirect.com/science/article/pii/S0921510702004233

[11] S. D. Gedney, "An anisotropic perfectly matched layer-absorbing medium for the truncation of FDTD lattices," *IEEE Transactions on Antennas and Propagation*, vol. 44, no. 12, pp. 1630–1639, Dec. 1996.

[12] DuPont Microcircuit Materials, "Dupont GreenTape 9k7: Design and layout guidelines," 2009. [Online]. Available: http://www2.dupont.com/MCM/en_US/assets/downloads/prodinfo/GreenTape_Design_Layout_Guidelines.pdf

[13] R. Landauer, "Shock waves in nonlinear transmission lines and their effect on parametric amplification," *IBM J. Res. Dev.*, vol. 4, no. 4, p. 391401, Oct. 1960. [Online]. Available: http://dx.doi.org/10.1147/rd.44.0391

[14] V. V. Rostov, N. M. Bykov, D. N. Bykov, A. I. Klimov, O. B. Kovalchuk, and I. V. Romanchenko, "Generation of subgigawatt RF pulses in nonlinear transmission lines," *Plasma Science, IEEE Transactions on*, vol. PP, no. 99, pp. 1–5, 2010. [Online]. Available: 10.1109/TPS.2010.2048722

[15] J. Thorpe, D. Steenson, and R. Miles, "Harmonic generation using soliton effects on nonlinear transmission lines," in *High Frequency Postgraduate Student Colloquium, 1997*, 1997, pp. 87–92. [Online]. Available: 10.1109/HFPSC.1997.651663

[16] J. S. Russell, "Report on waves," in *Rep. 14th Meeting of the British Association for the Advancement of Science*, 1845.

[17] N. J. Zabusky and M. D. Kruskal, "Interaction of "Solitons" in a collisionless plasma and the recurrence of initial states," *Physical Review Letters*, vol. 15, no. 6, pp. 240–243, Aug. 1965. [Online]. Available: http://link.aps.org/doi/10.1103/PhysRevLett.15.240

[18] M. J. Ablowitz, G. Biondini, and L. A. Ostrovsky, "Optical solitons: Perspectives and applications," *Chaos: An Interdisciplinary Journal of Nonlinear Science*, vol. 10, no. 3, pp. 471–474, Sep. 2000. [Online]. Available: http://chaos.aip.org/resource/1/chaoeh/v10/i3/p471_s1

[19] P. Wang, G. Pei, and E. Kan, "Pulsed wave interconnect," *Very Large Scale Integration (VLSI) Systems, IEEE Transactions on*, vol. 12, no. 5, pp. 453 –463, May 2004.

[20] E. Afshari and A. Hajimiri, "Nonlinear transmission lines for pulse shaping in silicon," *Solid-State Circuits, IEEE Journal of*, vol. 40, no. 3, pp. 744–752, 2005. [Online]. Available: 10.1109/JSSC.2005.843639

[21] C. Wilson, M. Turner, and P. Smith, "Pulse sharpening in a uniform LC ladder network containing nonlinear ferroelectric capacitors," *IEEE Transactions on Electron Devices*, vol. 38, no. 4, pp. 767 –771, Apr. 1991.

[22] J. M. Sanders, Y.-H. Lin, R. Ness, A. Kuthi, and M. Gundersen, "Pulse sharpening and soliton generation with nonlinear transmission lines for producing RF bursts," in *Power Modulator and High Voltage Conference (IPMHVC), 2010 IEEE International.* IEEE, May 2010, pp. 604–607.

[23] F. Benson and J. Last, “Nonlinear-transmission-line harmonic generator,” *Proceedings of the Institution of Electrical Engineers*, vol. 112, no. 4, pp. 635 –643, Apr. 1965.

[24] S. K. Mullick, “Propagation of signals in nonlinear transmission lines,” *IBM Journal of Research and Development*, vol. 11, no. 5, pp. 558 –562, Sep. 1967.

[25] R. H. Freeman and A. E. Karbowiak, “An investigation of nonlinear transmission lines and shock waves,” *Journal of Physics D: Applied Physics*, vol. 10, no. 5, pp. 633–643, Apr. 1977. [Online]. Available: http://iopscience.iop.org/0022-3727/10/5/005

[26] C. Wilson, M. Turner, and P. Smith, “Pulse sharpening in a uniform LC ladder network containing nonlinear ferroelectric capacitors,” in *Power Modulator Symposium, 1990., IEEE Conference Record of the 1990 Nineteenth*, Jun. 1990, pp. 204 –207.

[27] S. Ibuka, K. Abe, T. Miyazawa, A. Ishii, and S. Ishii, “Fast high-voltage pulse generator with nonlinear transmission line for high repetition rate operation,” *Plasma Science, IEEE Transactions on*, vol. 25, no. 2, pp. 266 –271, Apr. 1997.

[28] J.-M. Duchamp, P. Ferrari, M. Fernandez, A. Jrad, X. Melique, J. Tao, S. Arscott, D. Lippens, and R. Harrison, “Comparison of fully distributed and periodically loaded nonlinear transmission lines,” *Microwave Theory and Techniques, IEEE Transactions on*, vol. 51, no. 4, pp. 1105–1116, 2003. [Online]. Available: 10.1109/TMTT.2003.809621

[29] G. Zhao, R. Joshi, S. Rogers, E. Schamiloglu, and H. Hjalmarson, “Simulation studies for nonlinear-transmission-line based ultrafast rise times and waveform shaping for pulsed-power applications,” *Plasma Science, IEEE Transactions on*, vol. 36, no. 5, pp. 2618 –2625, Oct. 2008.

[30] W. H. Bostick, V. Nardi, and O. S. F. Zucker, *Energy Storage, Compression, and Switching.* Basic Books, 1976.

[31] N. S. Kuek, A. C. Liew, E. Schamiloglu, and J. O. Rossi, “Circuit modeling of nonlinear lumped element transmission lines including hybrid lines,” *Plasma Science, IEEE Transactions on*, vol. PP, no. 99, pp. 1 –12, 2012.

[32] R. F. Harrington, *Time-harmonic electromagnetic fields.* McGraw-Hill, 1961.

[33] J. Dolan, H. Bolton, and A. Shapland, “Analysis of ferrite line pulse sharpeners,” in *Nineth IEEE International Pulsed Power Conference*, vol. 1. IEEE, 1993, p. 308.

[34] P. Norgard and R. Curry, “PSpice simulations of nonlinear transmission lines based on ferroelectric dielectrics,” in *2011 IEEE Pulsed Power Conference (PPC)*, Jun. 2011, pp. 162 –166.

[35] G. Agrawal, *Nonlinear Fiber Optics.* Academic Press, Oct. 2012.

[36] L. L. F. Mollenauer and J. P. Gordon, *Solitons in Optical Fibers: Fundamentals and Applications.* Academic Press, Feb. 2006.

[37] A. Hasegawa and M. Matsumoto, *Optical Solitons in Fibers.* Springer, Dec. 2002.

[38] E. Garmire, R. Y. Chiao, and C. H. Townes, “Dynamics and characteristics of the self-trapping of intense light beams,” *Physical Review Letters*, vol. 16, no. 9, pp. 347–349, Feb. 1966. [Online]. Available: http://link.aps.org/doi/10.1103/PhysRevLett.16.347

[39] Y. Silberberg, “Collapse of optical pulses,” *Optics Letters*, vol. 15, no. 22, pp. 1282–1284, Nov. 1990. [Online]. Available: http://ol.osa.org/abstract.cfm?URI=ol-15-22-1282

[40] R. I. Miller and T. G. Roberts, “Laser self-focusing in the atmosphere,” *Applied Optics*, vol. 26, no. 21, pp. 4570–4575, Nov. 1987. [Online]. Available: http://ao.osa.org/abstract.cfm?URI=ao-26-21-4570

[41] M. Fujii, M. Tahara, I. Sakagami, W. Freude, and P. Russer, “High-order FDTD and auxiliary differential equation formulation of optical pulse propagation in 2-d kerr and raman nonlinear dispersive media,” *IEEE Journal of Quantum Electronics*, vol. 40, no. 2, pp. 175– 182, Feb. 2004.

[42] Z. Lubin, J. Greene, and A. Taflove, “FDTD computational study of ultra-narrow TM non-paraxial spatial soliton interactions,” *IEEE Microwave and Wireless Components Letters*, vol. 21, no. 5, pp. 228 –230, May 2011.

[43] M. Fujii, N. Omaki, M. Tahara, I. Sakagami, C. Poulton, W. Freude, and P. Russer, “Optimization of nonlinear dispersive APML ABC for the FDTD analysis of optical solitons,” *IEEE Journal of Quantum Electronics*, vol. 41, no. 3, pp. 448 – 454, Mar. 2005.

[44] A. A. Sukhorukov, Y. S. Kivshar, H. S. Eisenberg, and Y. Silberberg, “Spatial optical solitons in waveguide arrays,” *IEEE Journal of Quantum Electronics*, vol. 39, no. 1, pp. 31– 50, Jan. 2003.

[45] A. Taflove and S. C. Hagness, *Computational electrodynamics: the finite-difference time-domain method.* Artech House, Jun. 2005.

[46] G. C. Southworth, *Principles and applications of wave-guide transmission.* Van Nostrand, 1966.

[47] T. Anderson, “Rectangular and ridge waveguide,” *IRE Transactions on Microwave Theory and Techniques*, vol. 4, no. 4, pp. 201 –209, Oct. 1956.

[48] S. M. Wentworth, *Fundamentals of Electromagnetics with Engineering Applications.* John Wiley & Sons, Jul. 2006.

[49] A. Karbowiak, “Propagation of transients in waveguides,” *Proceedings of the IEE - Part C: Monographs*, vol. 104, no. 6, pp. 339 –348, Sep. 1957.

[50] C. R. Paul, *Introduction to Electromagnetic Compatibility.* John Wiley & Sons, Jan. 2006.

[51] P. Pleshko and I. Palcz, "Experimental observation of sommerfeld and brillouin precursors in the microwave domain," *Physical Review Letters*, vol. 22, no. 22, pp. 1201–1204, Jun. 1969. [Online]. Available: http://link.aps.org/doi/10.1103/PhysRevLett.22.1201

[52] S. Dvorak, "Exact, closed-form expressions for transient fields in homogeneously filled waveguides," *IEEE Transactions on Microwave Theory and Techniques*, vol. 42, no. 11, pp. 2164 –2170, Nov. 1994.

[53] G. Kristensson, "Transient electromagnetic wave propagation in waveguides," *Journal of Electromagnetic Waves and Applications*, vol. 9, no. 5-6, pp. 645–671, 1995. [Online]. Available: http://www.tandfonline.com/doi/abs/10.1163/156939395X00866

[54] R. E. Collin, I. A. Society, and Propagation, *Field theory of guided waves.* IEEE Press, 1991.

[55] F. Xu and K. Wu, "Guided-wave and leakage characteristics of substrate integrated waveguide," *IEEE Transactions on Microwave Theory and Techniques*, vol. 53, no. 1, pp. 66 – 73, Jan. 2005.

[56] X.-P. Chen and K. Wu, "Low-loss ultra-wideband transition between conductor-backed coplanar waveguide and substrate integrated waveguide," in *Microwave Symposium Digest, 2009. MTT '09. IEEE MTT-S International*, Jun. 2009, pp. 349 –352.

[57] G. Kompa, "About the frequency-dependent characteristics of a microstrip-waveguide transition," *International Journal of Electronics and Communications*, vol. 35, pp. 69–71, 1984.

[58] K. Lu, "An efficient method for analysis of arbitrary nonuniform transmission lines," *IEEE Transactions on Microwave Theory and Techniques*, vol. 45, no. 1, pp. 9 –14, Jan. 1997.

[59] J. Xu, Z. N. Chen, X. Qing, and W. Hong, "140-GHz planar broadband LTCC SIW slot antenna array," *IEEE Transactions on Antennas and Propagation*, vol. 60, no. 6, pp. 3025 –3028, Jun. 2012.

[60] A.-C. Bunea, M. Lahti, D. Neculoiu, A. Stefanescu, and T. Vaha-Heikkila, "Investigation of substrate integrated waveguide in LTCC technology for mm-wave applications," in *Microwave Conference Proceedings (APMC), 2011 Asia-Pacific*, Dec. 2011, pp. 395 –398.

[61] H. A. Pohl, "Giant polarization in high polymers," *Journal of Electronic Materials*, vol. 15, no. 4, pp. 201–203, Jul. 1986. [Online]. Available: http://link.springer.com/article/10.1007/BF02659632

[62] A. Tagantsev, V. Sherman, K. Astafiev, J. Venkatesh, and N. Setter, "Ferroelectric materials for microwave tunable applications," *Journal of Electroceramics*, vol. 11, no. 1, pp. 5–66, 2003. [Online]. Available: http://www.springerlink.com/content/q432r02g75367330/abstract/

[63] N. Alford, S. Penn, A. Templeton, X. Wang, J. Gallop, N. Klein, C. Zuccaro, and P. Filhol, "Microwave dielectrics," in *No: 1997/317), IEE Colloquium on Electrotechnical Ceramics - Processing, Properties and Applications (Ref*, Nov. 1997, pp. 9/1 –9/5.

[64] A. Deleniv, A. Eriksson, and S. Gevorgian, "Design of narrow-band tunable band-pass filters based on dual mode SrTiO3 disc resonators," in *Microwave Symposium Digest, 2002 IEEE MTT-S International*, vol. 2, 2002, pp. 1197 –1200.

[65] J. Rao, D. Patel, and V. Krichevsky, "Voltage-controlled ferroelectric lens phased arrays," *IEEE Transactions on Antennas and Propagation*, vol. 47, no. 3, pp. 458 –468, Mar. 1999.

[66] A. Kozyrev, V. Osadchy, A. Pavlov, and L. Sengupta, "Application of ferroelectrics in phase shifter design," in *Microwave Symposium Digest. 2000 IEEE MTT-S International*, vol. 3, 2000, pp. 1355 –1358 vol.3.

[67] J. F. Scott, *Ferroelectric Memories.* Springer, Jun. 2000.

[68] M. D. Graef and M. E. McHenry, *Structure of Materials: An Introduction to Crystallography, Diffraction and Symmetry.* Cambridge University Press, Aug. 2007.

[69] B. Su, J. Holmes, C. Meggs, and T. Button, "Dielectric and microwave properties of barium strontium titanate (BST) thick films on alumina substrates," *Journal of the European Ceramic Society*, vol. 23, no. 14, pp. 2699–2703, 2003. [Online]. Available: http://www.sciencedirect.com/science/article/pii/S0955221903001717

[70] N. Sbrockey, T. Kalkur, M. Luong, and G. Tompa, "MOCVD growth of tunable dielectrics for RF devices," *Vacuum Technology & Coating*, vol. 12, no. 1, pp. 40–44, Jan. 2011.

[71] G. Vlu, G. Houzet, L. Burgnies, J. C. Carru, A. Marteau, K. Blary, D. Lippens, P. Mounaix, M. Tondusson, and E. Nguma, "Electrical characterizations of paraelectric BST thin films up to 1 THz: realization of microwave phaseshifters," *Ferroelectrics*, vol. 353, no. 1, pp. 29–37, 2007. [Online]. Available: http://www.tandfonline.com/doi/abs/10.1080/00150190701367036

[72] T. Kalkur, N. Sbrockey, M. Loung, M. Cole, and G. Tompa, "Tunable RF filters with graded-composition, MOCVD-deposited BST capacitors," in *Applications of Ferroelectrics (ISAF/PFM), 2011 International Symposium on and 2011 International Symposium on Piezoresponse Force Microscopy and Nanoscale Phenomena in Polar Materials*, Jul. 2011, pp. 1 –4.

[73] M. Jain, S. B. Majumder, R. S. Katiyar, D. C. Agrawal, and A. S. Bhalla, "Dielectric properties of solgel-derived MgO:Ba0.5Sr0.5TiO3 thin-film composites," *Applied Physics Letters*, vol. 81, no. 17, pp. 3212–3214, Oct. 2002. [Online]. Available: http://apl.aip.org/resource/1/applab/v81/i17/p3212$_$s1

[74] H.-D. Wu and F. S. Barnes, "Doped Ba0.6Sr0.4TiO3 thin films for microwave device applications at room temperature," *Integrated Ferroelectrics*, vol. 22, no. 1-4, pp. 291–305, 1998. [Online]. Available: http://www.tandfonline.com/doi/abs/10.1080/10584589808208050

[75] O. G. Vendik and S. P. Zubko, "Modeling the dielectric response of incipient ferroelectrics," *Journal of Applied Physics*, vol. 82, no. 9, pp. 4475–4483, Nov. 1997. [Online]. Available: http://jap.aip.org/resource/1/japiau/v82/i9/p4475_s1

[76] C. H. Tsang, C. K. Wong, and F. G. Shin, "Modeling saturated and unsaturated ferroelectric hysteresis loops: An analytical approach," *Journal of Applied Physics*, vol. 98, no. 8, pp. 084 103–084 103–9, Oct. 2005. [Online]. Available: http://jap.aip.org/resource/1/japiau/v98/i8/p084103_s1

[77] P. Sain, M. Sain, and B. Spencer, "Models for hysteresis and application to structural control," in *American Control Conference, 1997. Proceedings of the 1997*, vol. 1, Jun. 1997, pp. 16 –20 vol.1.

[78] J. Yuan, *Numerical Simulation of Hysteresis Effects in Ferromagnetic Material with the Finite Integration Technique.* Cuvillier Verlag, 2005.

[79] A. Visintin, *Differential Models of Hysteresis.* Springer, Feb. 1995.

[80] C. B. Sawyer and C. H. Tower, "Rochelle salt as a dielectric," *Physical Review*, vol. 35, no. 3, pp. 269–273, Feb. 1930. [Online]. Available: http://link.aps.org/doi/10.1103/PhysRev.35.269

[81] H. Diamant, K. Drenck, and R. Pepinsky, "Bridge for accurate measurement of ferroelectric hysteresis," *Review of Scientific Instruments*, vol. 28, no. 1, pp. 30–33, Jan. 1957. [Online]. Available: http://rsi.aip.org/resource/1/rsinak/v28/i1/p30_s1

[82] B. Caudle, M. Baginski, H. Kirkici, and M. Hamilton, "Three-dimensional FDTD simulation of nonlinear ferroelectric materials in rectangular waveguide," *IEEE Transactions on Plasma Science (In Press)*, vol. 41, no. 2, 2013.

[83] K. Abe and S. Komatsu, "Epitaxial growth and dielectric properties of $ba_{0.24}sr_{0.76}tio_3$ thin film," *Japanese Journal of Applied Physics*, vol. 33, no. Part 1, No. 9B, pp. 5297–5300, Sep. 1994. [Online]. Available: http://jjap.jsap.jp/link?JJAP/33/5297

[84] P. L. Kelley, "Self-focusing of optical beams," *Physical Review Letters*, vol. 15, no. 26, pp. 1005–1008, Dec. 1965. [Online]. Available: http://link.aps.org/doi/10.1103/PhysRevLett.15.1005

[85] G. Bellanca, R. Semprini, and P. Bassi, "FDTD modelling of spatial soliton propagation," *Optical and Quantum Electronics*, vol. 29, no. 2, pp. 233–241, Feb. 1997. [Online]. Available: http://link.springer.com/article/10.1023/A%3A1018510323541

[86] W. L. Stutzman and G. A. Thiele, *Antenna theory and design.* J. Wiley, 1998.

[87] M. Ouaddari, S. Delprat, F. Vidal, M. Chaker, and K. Wu, “Microwave characterization of ferroelectric thin-film materials,” *IEEE Transactions on Microwave Theory and Techniques*, vol. 53, no. 4, pp. 1390– 1397, Apr. 2005.

[88] A. Giere, P. Scheele, Y. Zheng, and R. Jakoby, “Characterization of the field-dependent permittivity of nonlinear ferroelectric films using tunable coplanar lines,” *IEEE Microwave and Wireless Components Letters*, vol. 17, no. 6, pp. 442–444, Jun. 2007.

[89] M. Valant and D. Suvorov, “Low-temperature sintering of (Ba0.6Sr0.4)TiO3,” *Journal of the American Ceramic Society*, vol. 87, no. 7, p. 12221226, 2004. [Online]. Available: http://onlinelibrary.wiley.com/doi/10.1111/j.1151-2916.2004.tb07716.x/abstract

[90] E. Ngo, P. C. Joshi, M. W. Cole, and C. W. Hubbard, “Electrophoretic deposition of pure and MgO-modified Ba0.6Sr0.4TiO3 thick films for tunable microwave devices,” *Applied Physics Letters*, vol. 79, no. 2, pp. 248–250, Jul. 2001. [Online]. Available: http://apl.aip.org/resource/1/applab/v79/i2/p248$_$s1

[91] L. Sengupta and S. Sengupta, “Novel ferroelectric materials for phased array antennas,” *IEEE Transactions on Ultrasonics, Ferroelectrics and Frequency Control*, vol. 44, no. 4, pp. 792 –797, Jul. 1997.

[92] O. G. Vendik, E. K. Hollmann, A. B. Kozyrev, and A. M. Prudan, “Ferroelectric tuning of planar and bulk microwave devices,” *Journal of Superconductivity*, vol. 12, no. 2, pp. 325–338, Apr. 1999. [Online]. Available: http://link.springer.com/article/10.1023/A%3A1007797131173

[93] B.-H. Tsao, S. Heidger, and J. Weimer, “Sputtered barium titanate and barium strontium titanate films for capacitor applications,” in *Proceedings of the 2000 12th IEEE International Symposium on Applications of Ferroelectrics, 2000. ISAF 2000*, vol. 2, 2000, pp. 837 –840 vol. 2.

[94] K. Yee, “Numerical solution of initial boundary value problems involving maxwell’s equations in isotropic media,” *IEEE Transactions on Antennas and Propagation*, vol. 14, no. 3, pp. 302–307, May 1966.

[95] A. Elsherbeni and V. Demir, *The Finite Difference Time Domain Method for Electromagnetics: With MATLAB Simulations.* SciTech Publishing, 2009.

[96] P. Monk and E. Sli, “A convergence analysis of yees scheme on nonuniform grids,” *SIAM Journal on Numerical Analysis*, vol. 31, no. 2, pp. 393–412, Apr. 1994. [Online]. Available: http://epubs.siam.org/doi/abs/10.1137/0731021

[97] P. Monk and E. Suli, “Error estimates for yee’s method on non-uniform grids,” *IEEE Transactions on Magnetics*, vol. 30, no. 5, pp. 3200 –3203, Sep. 1994.

[98] J.-P. Berenger, “A perfectly matched layer for the absorption of electromagnetic waves,” *Journal of Computational Physics*, vol. 114, no. 2, pp. 185–200, Oct. 1994. [Online]. Available: http://www.sciencedirect.com/science/article/pii/S0021999184711594

[99] M. Kuzuoglu and R. Mittra, "Frequency dependence of the constitutive parameters of causal perfectly matched anisotropic absorbers," *IEEE Microwave and Guided Wave Letters*, vol. 6, no. 12, pp. 447 –449, Dec. 1996.

[100] J. A. Roden and S. D. Gedney, "Convolution PML (CPML): an efficient FDTD implementation of the CFSPML for arbitrary media," *Microwave and Optical Technology Letters*, vol. 27, no. 5, p. 334339, 2000. [Online]. Available: http://onlinelibrary.wiley.com/doi/10.1002/1098-2760(20001205)27:5⟨334::AID-MOP14⟩3.0.CO;2-A/abstract

[101] J.-P. Berenger, "Perfectly matched layer for the FDTD solution of wave-structure interaction problems," *IEEE Transactions on Antennas and Propagation*, vol. 44, no. 1, pp. 110 –117, Jan. 1996.

[102] I. S. Maksymov, A. A. Sukhorukov, A. V. Lavrinenko, and Y. S. Kivshar, "Comparative study of FDTD-Adopted numerical algorithms for kerr nonlinearities," *IEEE Antennas and Wireless Propagation Letters*, vol. 10, pp. 143–146, 2011.

[103] R. W. Ziolkowski and J. B. Judkins, "Full-wave vector maxwell equation modeling of the self-focusing of ultrashort optical pulses in a nonlinear kerr medium exhibiting a finite response time," *Journal of the Optical Society of America B*, vol. 10, no. 2, pp. 186–198, Feb. 1993. [Online]. Available: http://josab.osa.org/abstract.cfm?URI=josab-10-2-186

[104] F. Villegas, T. Cwik, Y. Rahmat-Samii, and M. Manteghi, "A parallel electromagnetic genetic-algorithm optimization (EGO) application for patch antenna design," *IEEE Transactions on Antennas and Propagation*, vol. 52, no. 9, pp. 2424 – 2435, Sep. 2004.

[105] J. Kim, T. Yoon, J. Kim, and J. Choi, "Design of an ultra wide-band printed monopole antenna using FDTD and genetic algorithm," *IEEE Microwave and Wireless Components Letters*, vol. 15, no. 6, pp. 395 – 397, Jun. 2005.

[106] D. Faircloth, M. Baginski, S. Rao, S. Wentworth, and M. Deshpande, "A novel procedure for design and synthesis of waveguide filters using the genetic algorithm," in *IEEE Antennas and Propagation Society International Symposium 2006*, Jul. 2006, pp. 2075 –2078.

[107] R. L. Haupt and D. H. Werner, *Genetic Algorithms in Electromagnetics.* John Wiley & Sons, Apr. 2007.

[108] Y. Rahmat-Samii and E. Michielssen, *Electromagnetic optimization by genetic algorithms.* J. Wiley, Jul. 1999.

[109] L. Khoong, Y. Tan, and Y. Lam, "Overview on fabrication of three-dimensional structures in multi-layer ceramic substrate," *Journal of the European Ceramic Society*, vol. 30, no. 10, pp. 1973–1987, Aug. 2010. [Online]. Available: http://www.sciencedirect.com/science/article/pii/S0955221910001391

[110] S. Lahiry, V. Gupta, K. Sreenivas, and A. Mansingh, "Dielectric properties of sol-gel derived barium-strontium-titanate (ba/sub 0.4/Sr/sub 0.6/TiO/sub 3/) thin films," *IEEE Transactions on Ultrasonics, Ferroelectrics and Frequency Control*, vol. 47, no. 4, pp. 854 –860, Jul. 2000.

[111] V. K. Palukuru, J. Perntie, M. Komulainen, T. Tick, and H. Jantunen, "Tunable microwave devices using low-sintering-temperature screen-printed barium strontium titanate (BST) thick films," *Journal of the European Ceramic Society*, vol. 30, no. 2, pp. 389–394, Jan. 2010. [Online]. Available: http://www.sciencedirect.com/science/article/pii/S0955221909003586

[112] T. Tick, J. Perntie, S. Rentsch, J. Mller, M. Hein, and H. Jantunen, "Co-sintering of barium strontium titanate (BST) thick films inside a LTCC substrate with pressure-assisted sintering," *Journal of the European Ceramic Society*, vol. 28, no. 14, pp. 2765–2769, Oct. 2008. [Online]. Available: http://www.sciencedirect.com/science/article/pii/S095522190800201X

[113] Amphenol, "132343 - SMA end launch jack for 0.032 inch PCB, 50 ohm, round post contact - amphenol connex," http://www.amphenolconnex.com/132343.html, 2011. [Online]. Available: http://www.amphenolconnex.com/132343.html

Appendix A: MATLAB Code

The flow and connection of MATLAB codes (`.m` files) used in this work is shown in Figure 1.

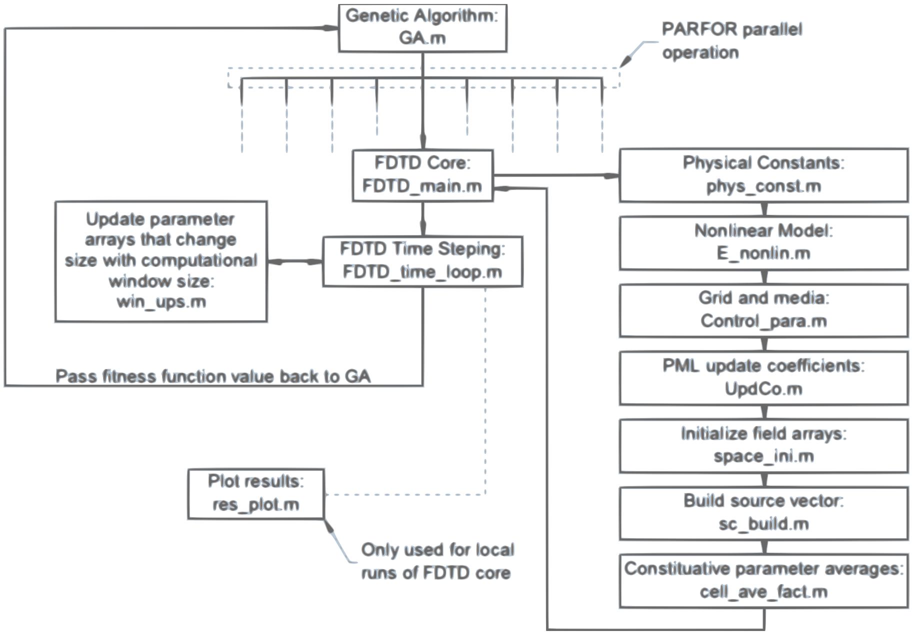

Figure 1: Code flow chart

.1 GA.m

```
clc; clear all; close all;

matlabpool open

isMPopen=matlabpool('size');

if isMPopen>0

    tic

    gens=50; %maximum number of generations

    pop_ini=64; %inital population

    max_l=309+1;

    N=6; %number of genes

    mats=10;%number of distinct material types

    gene_exp=6; %number of bits per gene

    gene_steps=2^gene_exp; %number of steps per gene

    direct_select=floor(pop_ini*0.1);

    %fraction of population directly copied

    cross_prob=0.6; %Probability of crossover

    mute_rate=0.02; %mutation rate

    fit_list=zeros((N+1),1); %Initialize solution database

    reused_sols=0; %Counter for the number of reused solution

    pop_data=zeros(N+1,pop_ini); %the '+1' index is the fitness value


    %initial population fill

    for p=1:pop_ini

        pop_data(1,p)=randi([1 mats],1,1); %material ID

        pop_data(2:3,p)=randi([1 gene_steps-1],2,1); %input and ouput taper

        pop_data(4,p)=randi([3 50],1,1); %layer half-width

        pop_data(5:6,p)=randi([1 gene_steps-1],2,1); %added central length
```

```
    %and voltage step
end


%%
for gen=1:gens
    %fitness function evaluation
    parfor p=1:pop_ini
        gen_sol_new(p)=true;
        for ps=2:size(fit_list,2) %search for a prior computed solution
            if all(pop_data(1:N,p)==fit_list(1:N,ps))
                reused_sols=reused_sols+1;
                gen_sol_new(p)=false;
                Pfit(p)=fit_list(N+1,ps);
            end
        end
        if gen_sol_new(p)
            fprintf('\nComputing solution %1.0i in gen %1.0i\n',...
                p,gen)
            mat_vect=pop_data(1,p)+5; %material index vector
            t_in=pop_data(2,p); %Input taper
            t_out=pop_data(3,p); %Output taper
            lay_half_thick=pop_data(4,p);
            lay_length=pop_data(5,p);
            V_scale=pop_data(6,p);
            [Pfit(p),unstable(p)]=...
                FDTD_main(mat_vect,t_in,t_out,lay_half_thick,...
                lay_length,V_scale);
```

```
    end
end


for p=1:pop_ini %add generated fitness solutions
 %to fit_list database
    if gen_sol_new(p)
        fit_list=[fit_list [(pop_data(1:N,p)); Pfit(p)]];
    end
end



pop_data(N+1,:)=Pfit;
[fit_order,pop_order]=sort(pop_data(N+1,:),2,'descend');
%sort fitness function


for p=1:pop_ini %sort individuals by fitness
    pop_data_temp(:,p)=pop_data(:,pop_order(p));
end


%Elitism Operation
if gen>1 && pop_data_temp(N+1,1)<=gen_best(N+1,gen-1)
    pop_data_temp(:,1)=gen_best(:,gen-1);
end


if any(unstable) %Report unstable solutions
    unst_count=sum(unstable);
    fprintf('FDTD instability failure on %i NEW solutions',...
```

```
        unst_count)
end

%Roulette wheel parameters
wheel_size=sum((pop_data_temp(N+1,:)));
wheel_space=cumsum((pop_data_temp(N+1,:)));
wheel_prob=wheel_space./wheel_size;

%direct copy to next generation
pop_data(:,(1:direct_select))=pop_data_temp(:,(1:direct_select));

for p=direct_select+1:2:(pop_ini-1)
    [p1temp,par1(p)]=min(abs(rand(1)-wheel_prob));
    [p2temp,par2(p)]=min(abs(rand(1)-wheel_prob));

    chr1=dec2bin([pop_data_temp(1:N,par1(p));(2^gene_exp-1)]);
    chr2=dec2bin([pop_data_temp(1:N,par2(p));(2^gene_exp-1)]);
    if rand(1)<cross_prob %if random value exceeds crossover
        %probability, then crossover
        cross_pointhold(gen,p)=randi(N);
        cross_point=cross_pointhold(gen,p);

        pop_data(1:N,p)=bin2dec([chr1(1:cross_point,:);...
            chr2(cross_point+1:N,:)]);
        pop_data(1:N,p+1)=bin2dec([chr2(1:cross_point,:);...
            chr1(cross_point+1:N,:)]);
    else
```

```
        pop_data(:,p)=pop_data_temp(:,par1(p));
        pop_data(:,p+1)=pop_data_temp(:,par2(p));
    end
end

for p=2:pop_ini %mutation
    child_chr=dec2bin([pop_data(1:N,p);(2^gene_exp-1)]);
    for g=1:N
        for b=1:gene_exp
            if b<4 || g>1 %prevent mutation of layer id bits
                if rand(1)<=mute_rate
                    if child_chr(g,b)=='0'
                        child_chr(g,b)='1';
                    else
                        child_chr(g,b)='0';
                    end
                end
            end
        end
    end
    pop_data(1:N,p)=bin2dec(child_chr(1:N,:));
    pop_data(1,p)=min((mats)*ones(1,1),(pop_data(1,p)));
    %clamp to maximum material id #

    pop_data(4,p)=min(50,(pop_data(4,p)));
    %clamp to maximum layer half-thickness
```

```
        pop_data(4,p)=max(3,(pop_data(4,p)));
        %clamp layer thickness to minimum value

        pop_data(1:N,p)=max(ones(N,1),(pop_data(1:N,p)));
        %clamp all to minimum value of 1
    end

    bar(pop_data_temp(N+1,:))
    title(sprintf('Sorted fitness for generation: %3.0i',gen-1))
    drawnow

    fprintf('Generation %1.0i complete, reused %3.0i solutions\n',...
        gen,(pop_ini-sum(gen_sol_new)));
    if gen>10 && gen_best(N+1,gen)==gen_best(N+1,gen-10)
        fprintf('\nSimulation halted on appearent convergence \n')
        gen_best(:,gen)
        break
    end

end

matlabpool close
t_end=toc/60
cl_data=clock;
data_fl=['GA14_' num2str(cl_data(2)) '_' num2str(cl_data(3)),...
    '_' num2str(cl_data(4)) 'h' num2str(cl_data(5)) 'm'];
save(data_fl);
```

```
else
    fprintf('\nMATLABpool failed to start')
end
```

.2 FDTD_main.m

```
function [sol_fit,unstable]=FDTD_main(mat,NL_taper_in,NL_taper_out,...
    lay_hthick,lay_length,V_scale)
int_plot=false; %controls the generation of internal test plots
int_diag=false; %controls the generation of internal diagnostics
if int_diag
    tic;
end

%% Setup parameters and coefficients
phsy_const; %physical constants
max_N=5000; frame_step=30; %time steps and frame step
E_nonlin; %Non-linear permitivitty
Control_Para; %Control Parameters
UpdCo; %Update Coefficients and CPML
space_ini; %intialize the field space
sc_build; %Source setup
cell_ave_fact; %Averaging of constituative parameters
if int_diag
t_setup=toc; %Measure setup time
end
%% Main FDTD run
sim_run=true; unstable=false; %Booleans to control simulation stop
```

```
%on instability or high computational error
sol_fit=0; %initialize fitness function
FDTD_time_loop;%Main FDTD time marching loop
if int_diag
    t_end=toc; %run time for the simulation run
    tic
    res_plot
end
end
```

.3 phys_const.m

```
%Physical Constants
ep0=8.854e-12; %free space permittivity
mu0=4*pi*1e-7; %free space permeability
c=1/sqrt(mu0*ep0); %speed of light
eta0=sqrt(mu0/ep0); %free space intrinsic impedance
```

.4 E_nonlin.m

```
%Nonlinear material modeling parameters
dl_mats=10; %number of material options
BSTx=linspace(0.5,0.25,dl_mats); %setup material set BST ratio's
T=300; %operating temperature in K
T_V=175;
for diel=1:dl_mats;
        T_0(diel)=42+439.37*BSTx(diel)-95.95*BSTx(diel)^2;
        C(diel)=(0.86+1.1*BSTx(diel)^2)/(10^-5);
        ep00(diel)=C(diel)/T_0(diel);
```

```
        alpha(diel)=(T_V/(ep0*C(diel)))*(sqrt((1/16)+(T/T_V)^2)-...
            (T_0(diel)/T_V));
        eta(diel)=ep00(diel)*alpha(diel)*ep0;
        E_N(diel)=(1/(1-0.7))*8.4/(ep0*(3*ep00(diel))^(3/2));
        ep_0bias(diel)=1/(alpha(diel)*ep0)./10; %divided by 10 due to dopant
        %reduced of permittivity
end
```

.5 Control_para.m

```
%Control Parameters for 8 layer 9k7 LTCC SIW
pulse_amp=V_scale*100;
ep_min_dt=7.1; %mimimum permittivity used for time step calculation
fill_permH=1; %permeability scale factor
an_rate=0.03;%frame delay in results animation
%%parameters / dimensions / spacing
a_dim=0.008581; %SIW width
b_dim=832e-6; %SIW hieght
L_pad=0.75e-2; %Length of SIW on each end of the BST layer
wall_thick_z=2; %wall thickness # of segments
wall_thick_y=2; %wall thickness # of segments
f_max=40e9; %maximum frequency of interest

lam_minLTCC=(3e8/sqrt(7.1)/f_max); %minimum wavelength in LTCC
N_y_LTCC=10; %number of cells at minimum wavelength in LTCC
delta_min_LTCC=lam_minLTCC/N_y_LTCC; %largest spatial step size in LTCC
N_y=10; %minimum wavelength in BST
lam_min=(3e8/sqrt(173)/f_max); %number of cells at minimum wavelength in BST
```

```
delta_min=lam_min/N_y; %spatial step size in BST

delta_y=delta_min*2; %spatial step size in y
short_segs=floor(b_dim/delta_y); %number of segment for the waveguide height
deltay=ones(short_segs,1)*delta_y; %vector represent step size in y
expand_fact=1.1; %rate of expansion of the nonuniform lattice

lay_steps=2*lay_hthick; %total thickness of the BST layer
lay_start=0+wall_thick_z; lay_stop=lay_steps; %layer start and stop points
deltaz=ones(lay_steps,1)*delta_min; %vector represent step size in z
wg_width=sum(deltaz); %variable used to accumulate total structure width
delta_min_holdx=expand_fact*delta_min; %step size within loop
while wg_width<a_dim;
    deltaz=[delta_min_holdx; deltaz; delta_min_holdx];
    lay_start=lay_start+1;
    if (expand_fact*delta_min_holdx)<delta_min_LTCC
        delta_min_holdx=expand_fact*delta_min_holdx;
    else
        delta_min_holdx=delta_min_LTCC;
    end
    wg_width=sum(deltaz);
end
lay_stop=lay_start+lay_steps; %calculate new layer stop index

total_length=NL_taper_in+NL_taper_out+lay_length; %total length of SIW
%in cells
SIW_start=1; %Start point of BST layer (modified below)
```

```
deltax=ones(total_length,1)*delta_min; %vector of step sizes in x
wg_length=0; %lenth of LTCC pad area in x (physical length)
delta_min_holdx=expand_fact*delta_min; %step size within loop
while wg_length<L_pad;
    deltax=[delta_min_holdx; deltax; delta_min_holdx];
    SIW_start=SIW_start+1;
    wg_length=wg_length+delta_min_holdx;
    if (expand_fact*delta_min_holdx)<delta_min_LTCC
        delta_min_holdx=expand_fact*delta_min_holdx;
    else
        delta_min_holdx=delta_min_LTCC;
    end
end
x_steps=size(deltax,1); %total number of x_steps (without PMLs)
%% Courant Limit Conditions
dt=0.95*(1/(c/sqrt(ep_min_dt)*sqrt(1/min(deltax)^2+1/min(deltay)^2+...
    1/min(deltaz)^2)));


%% PML parameters
pml.x=10; %PML thickness (in number of segments) x
%expand deltax to accommodate PML's.
deltax=[delta_min_holdx*ones(pml.x,1); deltax;...
    delta_min_holdx*ones(pml.x,1)];
pml.y=0; %PML thickness (in number of segments) y
pml.z=0; %PML thickness (in number of segments) z %suppression PML ONLY
m_pml=3; %PML order
```

```
K.max=15; K.max_x=K.max; K.max_y=K.max; K.max_z=K.max; %kappa maxes
sigma.opt=(0.8*(m_pml+1))/(eta0/sqrt(7.1)*delta_min_LTCC); %optimum sigma
sigma.max_x=sigma.opt;
sigma.max_y=sigma.opt;
sigma.max_z=sigma.opt;
a.max=0.005; a.max_x=a.max; a.max_y=a.max; a.max_z=a.max;; %alpha maxes
%% free space spatial steps (the space BETWEEN the PML's)
long_segs=size(deltaz,1); %number of transverse cells between walls
%expand deltay and deltaz for waveguide walls
deltay=[delta_y*ones(wall_thick_y,1); deltay; delta_y*ones(wall_thick_y,1)];
deltaz=[delta_min_LTCC*ones(wall_thick_z,1); deltaz;...
    delta_min_LTCC*ones(wall_thick_z,1)];

y_steps=size(deltay,1); %total vertical transverse cells
z_steps=size(deltaz,1); %total number of transverse cells
SIW_start=SIW_start+pml.x; %Shift BST layer start point
SIW_stop=SIW_start+total_length; %Shift BST layer stop point
%% Loop Drive, Center Points, result storage point
%Loop Drive parameters
x_stop=x_steps+2*pml.x; %add PML's to total cell count in x
y_stop=y_steps;
z_stop=z_steps;
sys_size=[x_stop y_stop z_stop]; %total size of system
N=max_N;

%Center points (by cell count, may not be physical center)(for source drive)
x_cent=round(x_stop/2);
```

```
y_cent=round(y_stop/2);
z_cent=round(z_stop/2);

%plot points and vectors
y_store = y_cent;
prop_vect=cumsum(deltax);
trans_vect=cumsum(deltaz);
vert_vect=cumsum(deltay);

%Cosine taper factor for source plane
sc_taper_fact=(trans_vect-(max(trans_vect)/2))/(max(trans_vect)/2);

%Delta's for updating H-fields
deltax_H=(deltax(2:end)+deltax(1:end-1))/2;
deltaz_H=(deltaz(2:end)+deltaz(1:end-1))/2;

%power integration factor as function of position in x
power_fact=repmat(shiftdim(deltaz,-2),x_stop,y_stop)*delta_y;



%% source drive points and computation end bound
x_dr=5+pml.x; %source drive point in x(cell #)
x_end=x_dr+20; %Initial end of moving window

%% media definitions - media 2 triggers PEC assumption
%wall boundary definitions
z_bound_inner_pl=z_stop-wall_thick_z;  z_bound_outer_pl=z_stop;
```

```
z_bound_inner_mi=wall_thick_z;  z_bound_outer_mi=1;

y_bound_inner_pl=y_stop-wall_thick_y+1; y_bound_outer_pl=y_stop;

y_bound_inner_mi=wall_thick_y; y_bound_outer_mi=1;




%Media rules

%Base Point:

Nmedia=15; %number of distinct media

%1 - initial freespace

%2 - forced PEC (deactivated)

%3 - finite conductor for waveguide walls

%4 - Microstrip Load Resistance (deactivated)

%5 - LTCC

%6-15 - Non-linear BST options


media=ones(x_stop,y_stop,z_stop)*5; %establish initial free space as LTCC


%media 3 - electric conductor (waveguide walls)

media(1:x_stop,:,z_bound_inner_pl:z_bound_outer_pl)=3; %right wall 4

media(1:x_stop,:,z_bound_outer_mi:z_bound_inner_mi)=3; %left wall 4

media(1:x_stop,y_bound_inner_pl:y_bound_outer_pl,:)=3; %top wall

media(1:x_stop,y_bound_outer_mi:y_bound_inner_mi,:)=3; %bottom wall


%media 4 -dielectric slab


lay_ct=1;

l=1; %layer 1
```

```
for i=SIW_start:SIW_stop
    if i<=(SIW_start+NL_taper_in(l))
         %reduction width factor to procude taper
        NL_reduc(i)=round((lay_steps(l)-round(lay_steps(l)*...
            ((i-SIW_start)/NL_taper_in(l))))/2);
        if (lay_stop(l)-NL_reduc(i))-(lay_start(l)+NL_reduc(i))>1
            media(i,y_bound_inner_mi+1:y_bound_inner_pl-1,...
                (lay_start(l)+NL_reduc(i)):(lay_stop(l)-...
                NL_reduc(i)))=mat(l);
        end
    elseif i>=(SIW_stop-NL_taper_out(l))
        NL_reduc(i)=round((lay_steps(l)-round(lay_steps(l)*...
            ((SIW_stop-i)/NL_taper_out(l))))/2);
        if NL_reduc(i)< (lay_hthick(l))
            media(i,y_bound_inner_mi+1:y_bound_inner_pl-1,...
                (lay_start(l)+NL_reduc(i)):(lay_stop(l)-...
                NL_reduc(i)))=mat(l);
        end
    else %full width region
        NL_reduc(i)=0;
        media(i,y_bound_inner_mi+1:y_bound_inner_pl-1,...
            (lay_start(l)+NL_reduc(i)):(lay_stop(l)-...
            NL_reduc(i)))=mat(l);
    end
end

%material definitions
```

```
ep_base(1:4)=ep0;
ep_base(5)=7.1*ep0;
ep_base(6:6+dl_mats-1)=ep_0bias*ep0;
mu_base(1:size(ep_base,2))=mu0;

sigmae_base=zeros(1,size(ep_base,2));
sigmae_base(3)=3.5e7;
omega_loss=10e9*2*pi;
loss_tan=0.02;
sigmae_base(6:Nmedia)=loss_tan*(ep_0bias*ep0*omega_loss);
sigmah_base=zeros(1,size(ep_base,2))+eps;
```

.6 UpdCo.m

```
%% Material parameter preallocation
sigma.Ex=zeros(1,x_stop)+eps;
sigma.Hx=zeros(1,x_stop)+eps;
sigma.Ey=zeros(1,y_stop)+eps;
sigma.Hy=zeros(1,y_stop)+eps;
sigma.Ez=zeros(1,z_stop)+eps;
sigma.Hz=zeros(1,z_stop)+eps;

a.Ex=zeros(1,x_stop)+eps;
a.Hx=zeros(1,x_stop)+eps;
a.Ey=zeros(1,y_stop)+eps;
a.Hy=zeros(1,y_stop)+eps;
a.Ez=zeros(1,z_stop)+eps;
a.Hz=zeros(1,z_stop)+eps;
```

```
%Averaged effective parameters
sigmaE=zeros(x_stop,y_stop,z_stop);
sigmaH=zeros(x_stop,y_stop,z_stop);
ep_eff=zeros(x_stop,y_stop,z_stop);
mu_eff=zeros(x_stop,y_stop,z_stop);

%% E sigma and K factors
for i=1:1:x_stop %Loop for x dependent values
    if i <= pml.x %x negative boundary case
        rho_e(i)=((pml.x-i+0.75)/(pml.x));
        poly_fact=rho_e(i)^m_pml;
        sigma.Ex(i)=poly_fact*sigma.max_x;
        K.Ex(i)=poly_fact*(K.max_x-1)+1;
        a.Ex(i)=a.max_x*(1-rho_e(i));
    elseif i > pml.x+x_steps %x positive boundary case
        edge=x_steps+pml.x; %last free space cell
        rho_e(i)=(i-(edge+1)+0.25)/(pml.x);
        poly_fact=rho_e(i)^m_pml;
        sigma.Ex(i)=poly_fact*sigma.max_x;
        K.Ex(i)=poly_fact*(K.max_x-1)+1;
        a.Ex(i)=a.max_x*(1-rho_e(i));
    else
        K.Ex(i)=1; %central computation space
    end
    be_x(i)=exp(-(sigma.Ex(i)/K.Ex(i)+a.Ex(i))*(dt/ep0));
    ce_x(i)=(sigma.Ex(i)*(be_x(i)-1))/(K.Ex(i)*...
```

```
        (sigma.Ex(i)+a.Ex(i)*K.Ex(i)));
end

clear rho_e

for j=1:1:y_stop %Loop for y dependent values
    if j <= pml.y %y negative boundary case
        rho_e(j)=((pml.y-j+0.75)/(pml.y));
        poly_fact=rho_e(j)^m_pml;
        sigma.Ey(j)=poly_fact*sigma.max_y;
        K.Ey(j)=poly_fact*(K.max_y-1)+1;
        a.Ey(j)=a.max_y*(1-rho_e(j));
    elseif j > pml.y+y_steps %y positive boundary case
        edge=y_steps+pml.y; %first pml cell
        rho_e(j)=(j-(edge+1)+0.25)/(pml.y);
        poly_fact=rho_e(j)^m_pml;
        sigma.Ey(j)=poly_fact*sigma.max_y;
        K.Ey(j)=poly_fact*(K.max_y-1)+1;
        a.Ey(j)=a.max_y*(1-rho_e(j));
    else
        K.Ey(j)=1; %central computation space
    end
    be_y(j)=exp(-(sigma.Ey(j)/K.Ey(j)+a.Ey(j))*(dt/ep0));
    ce_y(j)=(sigma.Ey(j)*(be_y(j)-1))/(K.Ey(j)*...
        (sigma.Ey(j)+a.Ey(j)*K.Ey(j)));
end
```

```
clear rho_e

for k=1:1:z_stop %Loop for z dependent values
    if k <= pml.z %z negative boundary case
        rho_e(k)=((pml.z-k+0.75)/(pml.z));
        poly_fact=rho_e(k)^m_pml;
        sigma.Ez(k)=poly_fact*sigma.max_z;
        K.Ez(k)=poly_fact*(K.max_z-1)+1;
        a.Ez(k)=a.max_z*(1-rho_e(k));
    elseif k > pml.z+z_steps %z positive boundary case
        edge=pml.z+z_steps; %first pml cell
        rho_e(k)=(k-(edge+1)+0.25)/(pml.z);
        poly_fact=rho_e(k)^m_pml;
        sigma.Ez(k)=poly_fact*sigma.max_z;
        K.Ez(k)=poly_fact*(K.max_z-1)+1;
        a.Ez(k)=a.max_z*(1-rho_e(k));
    else
        K.Ez(k)=1; %central computation space
    end
    be_z(k)=exp(-(sigma.Ez(k)/K.Ez(k)+a.Ez(k))*(dt/ep0));
    ce_z(k)=(sigma.Ez(k)*(be_z(k)-1))/(K.Ez(k)*...
        (sigma.Ez(k)+a.Ez(k)*K.Ez(k)));
end


%% H update half offset sigma and K factors
```

```
offset=0.5;

H_adj=1;

for i=1:1:x_stop %Loop for x dependent values

    if i <= pml.x %x negative boundary case

        rho_h(i)=((pml.x-i+0.25)/(pml.x));

        poly_fact=rho_h(i)^m_pml;

        sigma.Hx(i)=H_adj*poly_fact*sigma.max_x;

        K.Hx(i)=poly_fact*(K.max_x-1)+1;

        a.Hx(i)=H_adj*a.max_x*(1-rho_h(i));

    elseif i > pml.x+x_steps %x positive boundary case

        edge=x_steps+pml.x; %last free space cell

        rho_h(i)=(i-(edge+1)+0.75)/(pml.x);

        poly_fact=rho_h(i)^m_pml;

        sigma.Hx(i)=H_adj*poly_fact*sigma.max_x;

        K.Hx(i)=poly_fact*(K.max_x-1)+1;

        a.Hx(i)=H_adj*a.max_x*(1-rho_h(i));

    else

        K.Hx(i)=1;

    end

    bh_x(i)=exp(-(sigma.Hx(i)/K.Hx(i)+a.Hx(i))*(dt/ep0));

    ch_x(i)=(sigma.Hx(i)*(bh_x(i)-1))/(K.Hx(i)*...

        (sigma.Hx(i)+a.Hx(i)*K.Hx(i)));

end


clear rho_h


for j=1:1:y_stop %Loop for y dependent values
```

```
    if j <= pml.y-1 %y negative boundary case
        rho_h(j)=((pml.y-j+0.25)/(pml.y));
        poly_fact=rho_h(j)^m_pml;
        sigma.Hy(j)=H_adj*poly_fact*sigma.max_y;
        K.Hy(j)=poly_fact*(K.max_y-1)+1;
        a.Hy(j)=H_adj*a.max_y*(1-rho_h(j));
    elseif j > pml.y+y_steps %y positive boundary case
        edge=y_steps+pml.y; %first pml cell
        rho_h(j)=(j-(edge+1)+0.75)/(pml.y);
        poly_fact=rho_h(j)^m_pml;
        sigma.Hy(j)=H_adj*poly_fact*sigma.max_y;
        K.Hy(j)=poly_fact*(K.max_y-1)+1;
        a.Hy(j)=H_adj*a.max_y*(1-rho_h(j));
    else
        K.Hy(j)=1; %central computation space
    end
    bh_y(j)=exp(-(sigma.Hy(j)/K.Hy(j)+a.Hy(j))*(dt/ep0));
    ch_y(j)=(sigma.Hy(j)*(bh_y(j)-1))/(K.Hy(j)*...
        (sigma.Hy(j)+a.Hy(j)*K.Hy(j)));
end

clear rho_h

for k=1:1:z_stop %Loop for z dependent values
    if k <= pml.z-1 %z negative boundary case
        rho_h(k)=((pml.z-k+0.25)/(pml.z));
        poly_fact=rho_h(k)^m_pml;
```

```
        sigma.Hz(k)=H_adj*poly_fact*sigma.max_z;
        K.Hz(k)=poly_fact*(K.max_z-1)+1;
        a.Hz(k)=H_adj*a.max_z*(1-rho_h(k));
    elseif k > pml.z+z_steps %z positive boundary case
        edge=pml.z+z_steps; %first pml cell
        rho_h(k)=(k-(edge+1)+0.75)/(pml.z);
        poly_fact=rho_h(k)^m_pml;
        sigma.Hz(k)=H_adj*poly_fact*sigma.max_z;
        K.Hz(k)=poly_fact*(K.max_z-1)+1;
        a.Hz(k)=H_adj*a.max_z*(1-rho_h(k));
    else
        K.Hz(k)=1;%central computation space
    end
    bh_z(k)=exp(-(sigma.Hz(k)/K.Hz(k)+a.Hz(k))*(dt/ep0));
    ch_z(k)=(sigma.Hz(k)*(bh_z(k)-1))/(K.Hz(k)*...
        (sigma.Hz(k)+a.Hz(k)*K.Hz(k)));
end

%% Initialize some parameter arrays
for m=1:Nmedia
    m_id=(media==m);
    sigmaE=sigmaE+m_id*sigmae_base(m);
    sigmaH=sigmaH+m_id*sigmah_base(m);
    ep_eff=ep_eff+m_id*ep_base(m);
    mu_eff=mu_eff+m_id*mu_base(m);
end
```

.7 space_ini.m

```
%Intialize the field space

Ex=zeros(x_stop,y_stop,z_stop);

Hx=zeros(x_stop,y_stop,z_stop);

Ey=zeros(x_stop,y_stop,z_stop);

Hy=zeros(x_stop,y_stop,z_stop);

Ez=zeros(x_stop,y_stop,z_stop);

Hz=zeros(x_stop,y_stop,z_stop);


psi_Exy=zeros(x_stop,y_stop,z_stop);

psi_Exz=zeros(x_stop,y_stop,z_stop);

psi_Eyx=zeros(x_stop,y_stop,z_stop);

psi_Eyz=zeros(x_stop,y_stop,z_stop);

psi_Ezx=zeros(x_stop,y_stop,z_stop);

psi_Ezy=zeros(x_stop,y_stop,z_stop);


psi_Hxy=zeros(x_stop,y_stop,z_stop);

psi_Hxz=zeros(x_stop,y_stop,z_stop);

psi_Hyx=zeros(x_stop,y_stop,z_stop);

psi_Hyz=zeros(x_stop,y_stop,z_stop);

psi_Hzx=zeros(x_stop,y_stop,z_stop);

psi_Hzy=zeros(x_stop,y_stop,z_stop);
```

.8 sc_build.m

```
%Source Builder

f_cut=1/(2*a_dim*sqrt(ep0*mu0*7.1*fill_permH)); %TE_10 cutoff frequency
```

```
f_cent=f_cut*1.5; %waveguide center band frequency
T=dt; %sample time
N_samp=50000; %maximum number of time samples
t=(0:N_samp-1)*T; %time vector
tau=550*T; %Gaussian variance
t0=900*T; %time step offset
stop_n=2000; %last value of ’n’ with any significant source value
Vs=pulse_amp.*cos(2*pi*f_cent*(t-t0)).*exp(-((t-t0).^2./tau.^2));
%Gaussian modulated cosine pulse
```

.9 cell_ave_fact.m

```
%cell average factors
sigEfX=0.25*(sigmaE(1:x_stop-1,2:y_stop-1,2:z_stop-1)+...
    sigmaE(1:x_stop-1,1:y_stop-2,2:z_stop-1)+...
    sigmaE(1:x_stop-1,2:y_stop-1,1:z_stop-2)+...
    sigmaE(1:x_stop-1,1:y_stop-2,1:z_stop-2));

sigEfY=.25*(sigmaE(2:x_stop-1,1:y_stop-1,2:z_stop-1)+...
    sigmaE(1:x_stop-2,1:y_stop-1,2:z_stop-1)+...
    sigmaE(2:x_stop-1,1:y_stop-1,1:z_stop-2)+...
    sigmaE(1:x_stop-2,1:y_stop-1,1:z_stop-2));

sigEfZ=.25*(sigmaE(2:x_stop-1,2:y_stop-1,1:z_stop-1)+...
    sigmaE(2:x_stop-1,1:y_stop-2,1:z_stop-1)+...
    sigmaE(1:x_stop-2,2:y_stop-1,1:z_stop-1)+...
    sigmaE(1:x_stop-2,1:y_stop-2,1:z_stop-1));
```

```
sigMfX=(2*sigmaH(2:x_stop,1:y_stop-1,1:z_stop-1).*...
    sigmaH(1:x_stop-1,1:y_stop-1,1:z_stop-1))./...
    (sigmaH(2:x_stop,1:y_stop-1,1:z_stop-1)+...
    sigmaH(1:x_stop-1,1:y_stop-1,1:z_stop-1));

sigMfY=(2*sigmaH(1:x_stop-1,2:y_stop,1:z_stop-1).*...
    sigmaH(1:x_stop-1,1:y_stop-1,1:z_stop-1))./...
    (sigmaH(1:x_stop-1,2:y_stop,1:z_stop-1)+...
    sigmaH(1:x_stop-1,1:y_stop-1,1:z_stop-1));

sigMfZ=(2*sigmaH(1:x_stop-1,1:y_stop-1,2:z_stop).*...
    sigmaH(1:x_stop-1,1:y_stop-1,1:z_stop-1))./...
    (sigmaH(1:x_stop-1,1:y_stop-1,2:z_stop)+...
    sigmaH(1:x_stop-1,1:y_stop-1,1:z_stop-1));

mufX=(2*mu_eff(2:x_stop,1:y_stop-1,1:z_stop-1).*...
    mu_eff(1:x_stop-1,1:y_stop-1,1:z_stop-1))./...
    (mu_eff(2:x_stop,1:y_stop-1,1:z_stop-1)+...
    mu_eff(1:x_stop-1,1:y_stop-1,1:z_stop-1));

mufY=(2*mu_eff(1:x_stop-1,2:y_stop,1:z_stop-1).*...
    mu_eff(1:x_stop-1,1:y_stop-1,1:z_stop-1))./...
    (mu_eff(1:x_stop-1,2:y_stop,1:z_stop-1)+...
    mu_eff(1:x_stop-1,1:y_stop-1,1:z_stop-1));

mufZ=(2*mu_eff(1:x_stop-1,1:y_stop-1,2:z_stop).*...
    mu_eff(1:x_stop-1,1:y_stop-1,1:z_stop-1))./...
```

```
    (mu_eff(1:x_stop-1,1:y_stop-1,2:z_stop)+...
    mu_eff(1:x_stop-1,1:y_stop-1,1:z_stop-1));

bexY1=repmat(be_x(2:pml.x).',[1,y_stop-1,z_stop-2]);
cexY1=repmat(ce_x(2:pml.x).',[1,y_stop-1,z_stop-2]);

bexY2=repmat(be_x(pml.x+x_steps+1:x_stop-1).',[1,y_stop-1,z_stop-2]);
cexY2=repmat(ce_x(pml.x+x_steps+1:x_stop-1).',[1,y_stop-1,z_stop-2]);

bexZ1=repmat(be_x(2:pml.x).',[1,y_stop-2,z_stop-1]);
cexZ1=repmat(ce_x(2:pml.x).',[1,y_stop-2,z_stop-1]);

bexZ2=repmat(be_x(pml.x+x_steps+1:x_stop-1).',[1,y_stop-2,z_stop-1]);
cexZ2=repmat(ce_x(pml.x+x_steps+1:x_stop-1).',[1,y_stop-2,z_stop-1]);

bhxY1=repmat(bh_x(1:pml.x).',[1,y_stop-1,z_stop-1]);
chxY1=repmat(ch_x(1:pml.x).',[1,y_stop-1,z_stop-1]);

bhxY2=repmat(bh_x(pml.x+x_steps+1:x_stop-1).',[1,y_stop-1,z_stop-1]);
chxY2=repmat(ch_x(pml.x+x_steps+1:x_stop-1).',[1,y_stop-1,z_stop-1]);

bhxZ=repmat(bh_x(pml.x+x_steps+1:x_stop-1).',[1,y_stop-1,z_stop-1]);
chxZ=repmat(ch_x(pml.x+x_steps+1:x_stop-1).',[1,y_stop-1,z_stop-1]);

bhxZ1=repmat(bh_x(1:pml.x).',[1,y_stop-1,z_stop-1]);
chxZ1=repmat(ch_x(1:pml.x).',[1,y_stop-1,z_stop-1]);
```

```
bhxZ2=repmat(bh_x(pml.x+x_steps+1:x_stop-1).',[1,y_stop-1,z_stop-1]);
chxZ2=repmat(ch_x(pml.x+x_steps+1:x_stop-1).',[1,y_stop-1,z_stop-1]);
```

.10 FDTD_time_loop.m

```
%FDTD main time loop
%little 'n' for time step variable
frame_count=0; %initialize frame count for result recording
cells=0; %Total number of cells computed (for statistics only)
supress_region=8; %must be less the value used below x_dr+____.
plane_evalE1=0; plane_evalE2=0; x_start=1;
dfs=5; %distance from source for evaluation
trail_edge_eval=x_dr+dfs;
supr_start=trail_edge_eval; %start point of trailing edge suppression zone
if int_diag
    t_hold=t_setup;
end

unstable=false; unst_type=0; %Instability stop controls
pp_ct=0; %count of time steps passed since 'pulse_passed' idicator tripped
ft_look=x_stop-pml.x-5; %output evaluation plane (cell #)
w_e_in(1)=0; w_e_out(1)=0; %initializae input and output energy storage
win_ups;
% P_flow=zeros(x_stop,N);
pulse_passed=false;  %boolean for pulse passing through output
final_n=N; %last time step computed (updated elsewhere)
or_ind=0; %Overwrite index for storage of E_mag
%%
```

```
for n=1:1:N
    %% Time step based controls

    win_move=false; %window movement indicator
    if int_diag
        clc
        fprintf('%i%% complete - step %i - %i to %i - run #%i\n',...
            round(n/N*100),n,x_start,x_end,run_count)
        if n>1
            fprintf('%e joules in, %e joules out',w_e_in(n-1),w_e_out(n-1))
        end
    end

    if n<(stop_n) %during time source is active
        sc_drive=true;
    elseif n==stop_n %at the switch off of the source
        win_min=x_end; %Window is prevented from shrink below it width
        %when the source switched off
    elseif n>stop_n %begin the possiblity of moving the trail window edge.
        if plane_evalE1<(pulse_amp/delta_y*1e-4)
            %if trailing edge is weak and wider than
            %the minimum window width
            x_start=max(1,trail_edge_eval-dfs+1); %advance the trailing edge
            trail_edge_eval=trail_edge_eval+1;
            supr_start=supr_start+1; %advance the edge
            %of the suppression region
            win_move=true;
```

```
    for i=x_start:supr_start %setup suppresion region
        sigmaE(i,y_cent-y_bound_inner+1:y_cent+y_bound_inner-2,...
            z_cent-z_bound_inner+1:z_cent+z_bound_inner-1)=...
            (supr_start-i)^2*0.1;
        sigmaH(i,y_cent-y_bound_inner+1:y_cent+y_bound_inner-2,...
            z_cent-z_bound_inner+1:z_cent+z_bound_inner-1)=...
            (supr_start-i)^2*0.1/(120*pi/sqrt(fill_permE(1)))+eps;
        if i==x_dr
            sigmaE(x_dr,(y_cent-short_segs/2:y_cent),z_dr)=...
                sigmae_base(3);
            sigmaH(x_dr,(y_cent-short_segs/2:y_cent),z_dr)=...
                sigmah_base(3);
        end
    end
    cell_ave_fact; %recompute cell average factors
    Ex(1:(x_start-2),:,:)=0;
    Ey(1:(x_start-2),:,:)=0;
    Ez(1:(x_start-2),:,:)=0;
    Hx(1:(x_start-2),:,:)=0;
    Hy(1:(x_start-2),:,:)=0;
    Hz(1:(x_start-2),:,:)=0;
    if int_diag
        fprintf('\nTrailing Boundary Advanced')
    end
end
sc_drive=false;
if (x_start-x_end-1)<=win_min && int_diag;
```

```
        %detect minimum window operation
        fprintf('\nAt or below minimum window Operation')
    end
    if trail_edge_eval+10==x_end
        fprintf(strcat('\nSimulation halted on wave passing out ',...
            'of computation region\n'))
        sim_run=false;
        break
    end
    %

end

%leading window edge movement
if x_end==2*pml.x+x_steps %do nothing if window has reached max point
    if int_diag
        fprintf('\nSimulation reached PML boundary')
    end
else %conditional expansion ofthe leading edge of the window
    if plane_evalE2>(pulse_amp*1e-7) && x_end<x_stop
        win_move=true;
        if x_end>pml.x+x_steps-1
            x_end=x_stop; %snap in PML as wave approaches
        else
            x_end=x_end+1; %otherwise gradually expand window
        end
    end
```

```
end

if plane_evalE2>50e6 || isnan(plane_evalE1) %instability evaluation
    unstable=true;
    unst_type=2;
end
if plane_evalE1>pulse_amp*50000 || isnan(plane_evalE1)
    %instability evaluation
    unstable=true;
    unst_type=3;
end

if win_move %if windows has moveed or expanded, recacluated
    %coefficient arrays
    win_ups;
end

%% Field magnitude and prior value holding and instability evaluations
E_mag(1:x_end,:,:)=sqrt(Ex(1:x_end,:,:).^2+Ey(1:x_end,:,:).^2+...
    Ez(1:x_end,:,:).^2);
plane_evalE1=max(max(max(E_mag(trail_edge_eval:trail_edge_eval+10,...
    y_bound_inner_mi+1:y_bound_inner_pl-1,...
    z_bound_inner_mi+1:z_bound_inner_pl-1))));
plane_evalE2=max(max(E_mag(x_end-1,...
    y_bound_inner_mi+1:y_bound_inner_pl-1,...
    z_bound_inner_mi+1:z_bound_inner_pl-1)));
if max(max(max(E_mag)))>120e6; %breakdown voltage check
```

```
    unstable=true;
    unst_type=7;
end

E_mag_sf=20; %time averaging for E_mag used
%to calculate nonlinear permittivity
if n>E_mag_sf
    or_ind=or_ind+1;
    if or_ind>E_mag_sf
        or_ind=1;
    end
    E_mag_store(SIW_start:SIW_stop,:,lay_start:lay_stop,or_ind)=...
        sqrt(Ex(SIW_start:SIW_stop,:,lay_start:lay_stop).^2+...
        Ey(SIW_start:SIW_stop,:,lay_start:lay_stop).^2+...
        Ez(SIW_start:SIW_stop,:,lay_start:lay_stop).^2);
    E_mag_ave=sum(E_mag_store,4)/E_mag_sf;
else
    or_ind=or_ind+1;
    E_mag_store(SIW_start:SIW_stop,:,lay_start:lay_stop,or_ind)=...
        sqrt(Ex(SIW_start:SIW_stop,:,lay_start:lay_stop).^2+...
        Ey(SIW_start:SIW_stop,:,lay_start:lay_stop).^2+...
        Ez(SIW_start:SIW_stop,:,lay_start:lay_stop).^2);
    E_mag_ave(SIW_start:SIW_stop,:,lay_start:lay_stop)=...
        E_mag_store(SIW_start:SIW_stop,:,lay_start:lay_stop,n);
end

%% Update ep_eff components and E fields
```

```
Exp=Ex; Eyp=Ey; Ezp=Ez; %prior value holding
SIW_end=min(SIW_stop,x_end);
Ni_max=2; %number of iteration in Newton iteration
%for nonlinear materials
for Ni=1:1:Ni_max
    ep_eff(SIW_start:SIW_end,:,:)=(media(SIW_start:SIW_end,:,:)<6).*...
        ep_eff(SIW_start:SIW_end,:,:);
    for l=1:lay_ct
        if mat(l)>=6
            diel=mat(l)-5;
            xi(SIW_start:SIW_end,...
             y_bound_inner_mi+1:y_bound_inner_pl-1,...
                lay_start(l):lay_stop(l))=...
                E_mag_ave(SIW_start:SIW_end,...
                y_bound_inner_mi+1:y_bound_inner_pl-1,...
                lay_start(l):lay_stop(l))./E_N(diel);
            xiSQ(SIW_start:SIW_end,...
                y_bound_inner_mi+1:y_bound_inner_pl-1,...
                lay_start(l):lay_stop(l))=...
                xi(SIW_start:SIW_end,...
                y_bound_inner_mi+1:y_bound_inner_pl-1,...
                lay_start(l):lay_stop(l)).^2;
            ep_eff(SIW_start:SIW_end,...
                y_bound_inner_mi+1:y_bound_inner_pl-1,...
                lay_start(l):lay_stop(l))=...
              ep_eff(SIW_start:SIW_end,...
                y_bound_inner_mi+1:y_bound_inner_pl-1,...
```

```
          lay_start(l):lay_stop(l))+...
        (media(SIW_start:SIW_end,...
          y_bound_inner_mi+1:y_bound_inner_pl-1,...
          lay_start(l):lay_stop(l))==...
        mat(l)).*max(ep_min_dt,ep00(diel)./...
        ((sqrt(xiSQ(SIW_start:SIW_end,...
          y_bound_inner_mi+1:y_bound_inner_pl-1,...
          lay_start(l):lay_stop(l))+...
        eta(diel)^3)+xi(SIW_start:SIW_end,...
          y_bound_inner_mi+1:y_bound_inner_pl-1,...
          lay_start(l):lay_stop(l))).^(2/3)+...
        (sqrt(xiSQ(SIW_start:SIW_end,...
          y_bound_inner_mi+1:y_bound_inner_pl-1,...
          lay_start(l):lay_stop(l))+...
        eta(diel)^3)-xi(SIW_start:SIW_end,...
          y_bound_inner_mi+1:y_bound_inner_pl-1,...
          lay_start(l):lay_stop(l))).^(2/3)-eta(diel))).*ep0./10;
      %divided by 10 due to dopant
    end
end




%Ex
epf=0.25*(ep_eff(x_start:x_end-1,2:y_stop-1,2:z_stop-1)+...
    ep_eff(x_start:x_end-1,1:y_stop-2,2:z_stop-1)+...
    ep_eff(x_start:x_end-1,2:y_stop-1,1:z_stop-2)+...
```

```
    ep_eff(x_start:x_end-1,1:y_stop-2,1:z_stop-2));
Ca=(1-((sigEfX(x_start:x_end-1,:,:)*dt)./(2*epf)))./...
    (1+((sigEfX(x_start:x_end-1,:,:)*dt)./(2*epf)));
Cb=(dt/epf)./(1+((sigEfX(x_start:x_end-1,:,:)*dt)./(2*epf)));

Ex(x_start:x_end-1,2:y_stop-1,2:z_stop-1)=...
    Ca.*Exp(x_start:x_end-1,2:y_stop-1,2:z_stop-1)+...
    Cb.*((Hz(x_start:x_end-1,2:y_stop-1,2:z_stop-1)-...
    Hz(x_start:x_end-1,1:y_stop-2,2:z_stop-1))./KEyX-...
    (Hy(x_start:x_end-1,2:y_stop-1,2:z_stop-1)-...
    Hy(x_start:x_end-1,2:y_stop-1,1:z_stop-2))./KEzX);

if Ni==Ni_max %update PML's on last iteration
    psi_Exy(x_start:x_end-1,2:y_stop-1,2:z_stop-1)=...
        beyX.*psi_Exy(x_start:x_end-1,2:y_stop-1,2:z_stop-1)+...
        ceyX.*(Hz(x_start:x_end-1,2:y_stop-1,2:z_stop-1)-...
        Hz(x_start:x_end-1,1:y_stop-2,2:z_stop-1))/delta_y;
    Ex(x_start:x_end-1,2:y_stop-1,2:z_stop-1)=...
        Ex(x_start:x_end-1,2:y_stop-1,2:z_stop-1)+...
        Cb.*(psi_Exy(x_start:x_end-1,2:y_stop-1,2:z_stop-1)-...
        psi_Exz(x_start:x_end-1,2:y_stop-1,2:z_stop-1));
end


%Ey


epf=0.25*(ep_eff(x_start+1:x_end-1,1:y_stop-1,2:z_stop-1)+...
```

```
            ep_eff(x_start:x_end-2,1:y_stop-1,2:z_stop-1)...
            +ep_eff(x_start+1:x_end-1,1:y_stop-1,1:z_stop-2)+...
            ep_eff(x_start:x_end-2,1:y_stop-1,1:z_stop-2));



        Ca=(1-((sigEfY(x_start:x_end-2,:,:)*dt)./(2*epf)))./...
            (1+((sigEfY(x_start:x_end-2,:,:)*dt)./(2*epf)));
        Cb=(dt/epf)./(1+((sigEfY(x_start:x_end-2,:,:)*dt)./(2*epf)));



        Ey(x_start+1:x_end-1,1:y_stop-1,2:z_stop-1)=...
            Ca.*Eyp(x_start+1:x_end-1,1:y_stop-1,2:z_stop-1)+...
            Cb.*((Hx(x_start+1:x_end-1,1:y_stop-1,2:z_stop-1)-...
            Hx(x_start+1:x_end-1,1:y_stop-1,1:z_stop-2))./KEzY-...
            (Hz(x_start+1:x_end-1,1:y_stop-1,2:z_stop-1)-...
            Hz(x_start:x_end-2,1:y_stop-1,2:z_stop-1))./KExY);

if Ni==Ni_max %update PML's on last iteration
    if x_start<pml.x %requires snap out of PML
        psi_Eyx(2:pml.x,1:y_stop-1,2:z_stop-1)=...
            bexY1.*psi_Eyx(2:pml.x,1:y_stop-1,2:z_stop-1)+...
            cexY1.*(Hz(2:pml.x,1:y_stop-1,2:z_stop-1)-...
            Hz(1:pml.x-1,1:y_stop-1,2:z_stop-1))./delta_min_holdx;
        Ey(2:pml.x,1:y_stop-1,2:z_stop-1)=...
            Ey(2:pml.x,1:y_stop-1,2:z_stop-1)+...
            Cb(1:pml.x-1,1:y_stop-1,1:z_stop-2).*...
            (psi_Eyz(2:pml.x,1:y_stop-1,2:z_stop-1)-...
```

```
            psi_Eyx(2:pml.x,1:y_stop-1,2:z_stop-1));
    end


    if x_end==x_stop %this is the case when the pml snap-in occurs
        psi_Eyx(pml.x+x_steps+1:x_stop-1,1:y_stop-1,2:z_stop-1)=...
            bexY2.*...
            psi_Eyx(pml.x+x_steps+1:x_stop-1,1:y_stop-1,2:z_stop-1)+...
            cexY2.*(Hz(pml.x+x_steps+1:x_stop-1,1:y_stop-1,2:z_stop-1)-...
            Hz(pml.x+x_steps+1-1:x_stop-2,1:y_stop-1,2:z_stop-1))./...
            delta_min_holdx;
        Ey(pml.x+x_steps+1:x_stop-1,1:y_stop-1,2:z_stop-1)=...
            Ey(pml.x+x_steps+1:x_stop-1,1:y_stop-1,2:z_stop-1)+...
            Cb(pml.x+x_steps-(x_start-1):x_stop-2-(x_start-1),...
            1:y_stop-1,1:z_stop-2).*...
            (psi_Eyz(pml.x+x_steps+1:x_stop-1,1:y_stop-1,2:z_stop-1)-...
            psi_Eyx(pml.x+x_steps+1:x_stop-1,1:y_stop-1,2:z_stop-1));
    end
end


        %Ez
        epf=0.25*(ep_eff(x_start+1:x_end-1,2:y_stop-1,1:z_stop-1)+...
            ep_eff(x_start:x_end-2,2:y_stop-1,1:z_stop-1)...
            +ep_eff(x_start+1:x_end-1,1:y_stop-2,1:z_stop-1)+...
            ep_eff(x_start:x_end-2,1:y_stop-2,1:z_stop-1));

        Ca=(1-((sigEfZ(x_start:x_end-2,:,:)*dt)./(2*epf)))./...
            (1+((sigEfZ(x_start:x_end-2,:,:)*dt)./(2*epf)));
```

```
Cb=(dt/epf)./(1+((sigEfZ(x_start:x_end-2,:,:)*dt)./(2*epf)));

Ez(x_start+1:x_end-1,2:y_stop-1,1:z_stop-1)=...
    Ca.*Ezp(x_start+1:x_end-1,2:y_stop-1,1:z_stop-1)+...
    Cb.*((Hy(x_start+1:x_end-1,2:y_stop-1,1:z_stop-1)-...
    Hy(x_start:x_end-2,2:y_stop-1,1:z_stop-1))./KExZ-...
    (Hx(x_start+1:x_end-1,2:y_stop-1,1:z_stop-1)-...
    Hx(x_start+1:x_end-1,1:y_stop-2,1:z_stop-1))./(KEyZ));

if Ni==Ni_max %update PML's on last iteration
    psi_Ezy(x_start+1:x_end-1,2:y_stop-1,1:z_stop-1)=...
        beyZ.*psi_Ezy(x_start+1:x_end-1,2:y_stop-1,1:z_stop-1)+...
        ceyZ.*(Hx(x_start+1:x_end-1,2:y_stop-1,1:z_stop-1)-...
        Hx(x_start+1:x_end-1,1:y_stop-2,1:z_stop-1))/delta_y;
    Ez(x_start+1:x_end-1,2:y_stop-1,1:z_stop-1)=...
        Ez(x_start+1:x_end-1,2:y_stop-1,1:z_stop-1)+Cb.*...
        (-psi_Ezy(x_start+1:x_end-1,2:y_stop-1,1:z_stop-1));

if x_start<pml.x
    psi_Ezx(2:pml.x,2:y_stop-1,1:z_stop-1)=...
        bexZ1.*psi_Ezx(2:pml.x,2:y_stop-1,1:z_stop-1)+...
        cexZ1.*(Hy(2:pml.x,2:y_stop-1,1:z_stop-1)-...
        Hy(1:pml.x-1,2:y_stop-1,1:z_stop-1))./delta_min_holdx;
    Ez(2:pml.x,2:y_stop-1,1:z_stop-1)=...
        Ez(2:pml.x,2:y_stop-1,1:z_stop-1)+...
        Cb(1:pml.x-1,1:y_stop-2,1:z_stop-1).*...
        (psi_Ezx(2:pml.x,2:y_stop-1,1:z_stop-1));
```

```
    end


    if x_end==x_stop
        psi_Ezx(pml.x+x_steps+1:x_stop-1,2:y_stop-1,1:z_stop-1)=...
            bexZ2.*psi_Ezx(pml.x+x_steps+1:x_stop-1,...
            2:y_stop-1,1:z_stop-1)+...
            cexZ2.*(Hy(pml.x+x_steps+1:x_stop-1,2:y_stop-1,...
            1:z_stop-1)-...
            Hy(pml.x+x_steps+1-1:x_stop-2,2:y_stop-1,...
            1:z_stop-1))./delta_min_holdx;
        Ez(pml.x+x_steps+1:x_stop-1,2:y_stop-1,1:z_stop-1)=...
            Ez(pml.x+x_steps+1:x_stop-1,2:y_stop-1,1:z_stop-1)+...
            Cb(pml.x+x_steps-(x_start-1):x_stop-2-(x_start-1),...
            1:y_stop-2,1:z_stop-1).*...
            (psi_Ezx(pml.x+x_steps+1:x_stop-1,2:y_stop-1,1:z_stop-1));
    end
    end


    if Ni<Ni_max && n>E_mag_sf %recompute E_mag_ave with new values
        E_mag_store(SIW_start:SIW_stop,:,...
        lay_start:lay_stop,E_mag_sf)=...
            sqrt(Ex(SIW_start:SIW_stop,:,lay_start:lay_stop).^2+...
            Ey(SIW_start:SIW_stop,:,lay_start:lay_stop).^2+...
            Ez(SIW_start:SIW_stop,:,lay_start:lay_stop).^2);
        E_mag_ave=sum(E_mag_store,4)/E_mag_sf;
    end
end %end nonlinear iteration loop
```

```
%Source Drive
if n<=stop_n
    for k=z_bound_inner_mi+1:z_bound_inner_pl-1
        Ey(x_dr,y_bound_inner_mi+1:y_bound_inner_pl-1,k)=...
            Ey(x_dr,y_bound_inner_mi+1:y_bound_inner_pl-1,k)+...
            Vs(n)/((short_segs)*delta_y)*cos((pi/2)*sc_taper_fact(k));
    end
end

%% Update H components

% Hx
Hx(x_start+1:x_end,1:y_stop-1,1:z_stop-1)=...
    DaX.*Hx(x_start+1:x_end,1:y_stop-1,1:z_stop-1)+...
    DbX.*((Ey(x_start+1:x_end,1:y_stop-1,2:z_stop)-...
    Ey(x_start+1:x_end,1:y_stop-1,1:z_stop-1))./KHzX-...
    (Ez(x_start+1:x_end,2:y_stop,1:z_stop-1)-...
    Ez(x_start+1:x_end,1:y_stop-1,1:z_stop-1))./KHyX);

psi_Hxy(x_start+1:x_end,1:y_stop-1,1:z_stop-1)=bhyX....
    *psi_Hxy(x_start+1:x_end,1:y_stop-1,1:z_stop-1)+...
    chyX.*(Ez(x_start+1:x_end,2:y_stop,1:z_stop-1)-...
    Ez(x_start+1:x_end,1:y_stop-1,1:z_stop-1))/delta_y;
Hx(x_start+1:x_end,1:y_stop-1,1:z_stop-1)=...
    Hx(x_start+1:x_end,1:y_stop-1,1:z_stop-1)+...
    DbX.*(psi_Hxz(x_start+1:x_end,1:y_stop-1,1:z_stop-1)-...
```

```
    psi_Hxy(x_start+1:x_end,1:y_stop-1,1:z_stop-1));

% Hy
Hy(x_start:x_end-1,2:y_stop,1:z_stop-1)=...
    DaY.*Hy(x_start:x_end-1,2:y_stop,1:z_stop-1)+...
    DbY.*((Ez(x_start+1:x_end,2:y_stop,1:z_stop-1)-...
    Ez(x_start:x_end-1,2:y_stop,1:z_stop-1))./KHxY-...
    (Ex(x_start:x_end-1,2:y_stop,2:z_stop)-...
    Ex(x_start:x_end-1,2:y_stop,1:z_stop-1))./KHzY);

if x_start<pml.x %requires snap out of PML
    psi_Hyx(1:pml.x,2:y_stop,1:z_stop-1)=...
        bhxY1.*psi_Hyx(1:pml.x,2:y_stop,1:z_stop-1)+...
        chxY1.*(Ez(2:pml.x+1,2:y_stop,1:z_stop-1)-...
        Ez(1:pml.x,2:y_stop,1:z_stop-1))/delta_min_holdx;
    Hy(1:pml.x,2:y_stop,1:z_stop-1)=...
        Hy(1:pml.x,2:y_stop,1:z_stop-1)+...
        DbY(1:pml.x,:,:).*(psi_Hyx(1:pml.x,2:y_stop,1:z_stop-1)-...
        psi_Hyz(1:pml.x,2:y_stop,1:z_stop-1));
end

if x_end==x_stop %this is the case when the pml snap-in occurs
    psi_Hyx(pml.x+x_steps+1:x_stop-1,2:y_stop,1:z_stop-1)=...
        bhxY2.*psi_Hyx(pml.x+x_steps+1:x_stop-1,2:y_stop,1:z_stop-1)+...
        chxY2.*(Ez(pml.x+x_steps+2:x_stop,2:y_stop,1:z_stop-1)-...
        Ez(pml.x+x_steps+1:x_stop-1,2:y_stop,1:z_stop-1))/...
        delta_min_holdx;
```

```
    Hy(pml.x+x_steps+1:x_stop-1,2:y_stop,1:z_stop-1)=...
        Hy(pml.x+x_steps+1:x_stop-1,2:y_stop,1:z_stop-1)+...
        DbY(pml.x+x_steps+1-(x_start-1):x_stop-1-(x_start-1),:,:).*...
        (psi_Hyx(pml.x+x_steps+1:x_stop-1,2:y_stop,1:z_stop-1)-...
        psi_Hyz(pml.x+x_steps+1:x_stop-1,2:y_stop,1:z_stop-1));
end

%Hz
Hz(x_start:x_end-1,1:y_stop-1,2:z_stop)=...
    DaZ.*Hz(x_start:x_end-1,1:y_stop-1,2:z_stop)+...
    DbZ.*((Ex(x_start:x_end-1,2:y_stop,2:z_stop)-...
    Ex(x_start:x_end-1,1:y_stop-1,2:z_stop))./KHyZ-...
    (Ey(x_start+1:x_end,1:y_stop-1,2:z_stop)-...
    Ey(x_start:x_end-1,1:y_stop-1,2:z_stop))./KHxZ);



psi_Hzy(x_start:x_end-1,1:y_stop-1,2:z_stop)=...
    bhyZ.*psi_Hzy(x_start:x_end-1,1:y_stop-1,2:z_stop)+...
    chyZ.*(Ex(x_start:x_end-1,2:y_stop,2:z_stop)-...
    Ex(x_start:x_end-1,1:y_stop-1,2:z_stop))/delta_y;
Hz(x_start:x_end-1,1:y_stop-1,2:z_stop)=...
    Hz(x_start:x_end-1,1:y_stop-1,2:z_stop)+DbZ.*...
    psi_Hzy(x_start:x_end-1,1:y_stop-1,2:z_stop);

if x_start<pml.x %requires snap out of PML
    psi_Hzx(1:pml.x,1:y_stop-1,2:z_stop)=...
        bhxZ1.*psi_Hzx(1:pml.x,1:y_stop-1,2:z_stop)+...
```

```
        chxZ1.*(Ey(2:pml.x+1,1:y_stop-1,2:z_stop)-...
        Ey(1:pml.x,1:y_stop-1,2:z_stop))/delta_min_holdx;
    Hz(1:pml.x,1:y_stop-1,2:z_stop)=Hz(1:pml.x,1:y_stop-1,2:z_stop)+...
        DbZ(1:pml.x,:,:).*(-psi_Hzx(1:pml.x,1:y_stop-1,2:z_stop));
end

if x_end==x_stop %this is the case when the pml snap-in occurs
    psi_Hzx(pml.x+x_steps+1:x_stop-1,1:y_stop-1,2:z_stop)=...
        bhxZ2.*psi_Hzx(pml.x+x_steps+1:x_stop-1,1:y_stop-1,2:z_stop)+...
        chxZ2.*(Ey(pml.x+x_steps+2:x_stop,1:y_stop-1,2:z_stop)-...
        Ey(pml.x+x_steps+1:x_stop-1,1:y_stop-1,2:z_stop))/...
        delta_min_holdx;
    Hz(pml.x+x_steps+1:x_stop-1,1:y_stop-1,2:z_stop)=...
        Hz(pml.x+x_steps+1:x_stop-1,1:y_stop-1,2:z_stop)+...
        DbZ(pml.x+x_steps+1-(x_start-1):x_stop-1-(x_start-1),:,:).*...
        (-psi_Hzx(pml.x+x_steps+1:x_stop-1,1:y_stop-1,2:z_stop));
end
%% Power / Energy computation
Px=Ey.*Hz-Ez.*Hy;
P_flow(:,n)=sum(sum(Px.*power_fact,3),2);
w_e_in(n)=sum(P_flow(x_dr,:))*dt;
w_e(:,n)=sum(P_flow(:,:),2)*dt;
w_e_out(n)=sum(P_flow(ft_look,:))*dt;
Pfdiv=diff(P_flow(ft_look,1:n));
Pfdiv_sc=diff(P_flow(x_dr+10,1:n));
if n>(t0/T/2) && max(Pfdiv)>max(Pfdiv_sc) && pulse_passed==0
    pulse_passed=true;
```

```
end
if n>(t0/T/8) && max(diff(w_e(SIW_start+1:end,n)))>5e-6 &&...
        ~pulse_passed
    unstable=true;
    fprintf('increasing energy failure detechted')
    unst_type=8;
end
%% frame record
if mod((n+frame_step-1),frame_step)==0 && int_diag
    frame_count=frame_count+1;
    Res(frame_count).Ey=Ey(:,y_store,:);
    Res(frame_count).Ez=Ez(:,y_store,:);
    Res(frame_count).EPF=ep_eff(:,y_store,:);
    Res(frame_count).Px=Px(:,y_store,:);
    plot_bounds(frame_count,:)=[x_start x_end];
end
%% time step stats
if int_diag
    t_step(n)=toc-t_hold;
    t_hold=toc;
    cells=cells+(x_end-x_start)*y_stop*z_stop;
end
%% Unstable halt
if any(isnan(P_flow(:,n)))
    unstable=true;
    unst_type=6;
end
```

```
    if unstable
        fprintf('\n\nSimulation  numerical instability, type %i\n\n',...
            unst_type)
        sim_run=false;
        final_n=n;
        Pfit=0; Pfdiv_max=0;
        break
    end
    if pulse_passed
        pp_ct=pp_ct+1;
        if pp_ct>400 %count the time steps after the pulse has past
            sim_run=false;
            final_n=n;
            break
        end
    end

    %% Simulation completion
    if n==N %simulation has run to completion
        sim_run=false;
        final_n=n;
    end
end
%% Solution Evaluation
if unstable==0
    ave_fact=3;
    for n=ave_fact:final_n-ave_fact
```

```
        Pfdiv_ave(n-ave_fact+1)=...
            sum(Pfdiv(n-ave_fact+1:n+ave_fact-1))/(2*ave_fact-1);
        Pfdiv_sc_ave(n-ave_fact+1)=...
            sum(Pfdiv_sc(n-ave_fact+1:n+ave_fact-1))/(2*ave_fact-1);
    end
    Pfdiv_sc_max=max(Pfdiv_sc_ave);
    Pfdiv_max=max(Pfdiv_ave);
    sol_fit=Pfdiv_max/Pfdiv_sc_max
end

if int_diag
    fprintf('Final simulation step ran from x cell %f to %f\n',...
        x_start,x_end);
end
```

.11 win_ups.m

```
%Window dependant update factors
%H field update factors
DaX=(1-((sigMfX(x_start:x_end-1,:,:)*dt)./...
    (2*mufX(x_start:x_end-1,:,:)))./...
    (1+((sigMfX(x_start:x_end-1,:,:)*dt)./...
    (2*mufX(x_start:x_end-1,:,:))));
DbX=(dt./mufX(x_start:x_end-1,:,:))./...
    (1+((sigMfX(x_start:x_end-1,:,:).*dt)./...
    (2*mufX(x_start:x_end-1,:,:))));
KHzX=repmat(shiftdim(K.Hz(1:z_stop-1).*deltaz_H(1:z_stop-1).',-1),...
    [x_end-1-(x_start-1),y_stop-1,1]);
```

```
KHyX=repmat(K.Hy(1:y_stop-1).*deltay(1:y_stop-1).',[x_end-1-(x_start-1),...
    1,z_stop-1]);

DaY=(1-((sigMfY(x_start:x_end-1,:,:)*dt)./...
    (2*mufY(x_start:x_end-1,:,:))))./...
    (1+((sigMfY(x_start:x_end-1,:,:)*dt)./...
    (2*mufY(x_start:x_end-1,:,:))));
DbY=(dt./mufY(x_start:x_end-1,:,:))./...
    (1+((sigMfY(x_start:x_end-1,:,:).*dt)./...
    (2*mufY(x_start:x_end-1,:,:))));
KHxY=repmat((K.Hx(x_start:x_end-1).*deltax_H(x_start:x_end-1).').',...
    [1,y_stop-1,z_stop-1]);
KHzY=repmat(shiftdim(K.Hz(1:z_stop-1).*deltaz_H(1:z_stop-1).',-1),...
    [x_end-1-(x_start-1),y_stop-1,1]);


DaZ=(1-((sigMfZ(x_start:x_end-1,:,:)*dt)./...
    (2*mufZ(x_start:x_end-1,:,:))))./...
    (1+((sigMfZ(x_start:x_end-1,:,:)*dt)./...
    (2*mufZ(x_start:x_end-1,:,:))));
DbZ=(dt./mufZ(x_start:x_end-1,:,:))./...
    (1+((sigMfZ(x_start:x_end-1,:,:).*dt)./...
    (2*mufZ(x_start:x_end-1,:,:))));
KHyZ=repmat(K.Hy(1:y_stop-1).*deltay(1:y_stop-1).',...
    [x_end-1-(x_start-1),1, z_stop-1]);
KHxZ=repmat((K.Hx(x_start:x_end-1).*deltax_H(x_start:x_end-1).').',...
    [1,y_stop-1,z_stop-1]);
```

```
beyX=repmat(be_y(1,2:y_stop-1),[x_end-x_start,1,z_stop-2]);
ceyX=repmat(ce_y(1,2:y_stop-1),[x_end-x_start,1,z_stop-2]);

beyZ=repmat(be_y(1,2:y_stop-1),[x_end-x_start-1,1,z_stop-1]);
ceyZ=repmat(ce_y(1,2:y_stop-1),[x_end-x_start-1,1,z_stop-1]);

bhyX=repmat(bh_y(1,1:y_stop-1),[x_end-x_start,1,z_stop-1]);
chyX=repmat(ch_y(1,1:y_stop-1),[x_end-x_start,1,z_stop-1]);

bhyZ=repmat(bh_y(1,1:y_stop-1),[x_end-x_start,1,z_stop-1]);
chyZ=repmat(ch_y(1,1:y_stop-1),[x_end-x_start,1,z_stop-1]);

%E field update factors
KEyX=repmat(K.Ey(2:y_stop-1).*deltay(2:y_stop-1).',[x_end-1-(x_start-1),...
    1,z_stop-2]);
KEzX=repmat(shiftdim(K.Ez(2:z_stop-1).*deltaz(2:z_stop-1).',-1),...
    [x_end-1-(x_start-1),y_stop-2,1]);

KEzY=repmat(shiftdim(K.Ez(2:z_stop-1).*deltaz(2:z_stop-1).',-1),...
    [x_end-2-(x_start-1),y_stop-1,1]);
KExY=repmat((K.Ex(x_start+1:x_end-1).*deltax(x_start+1:x_end-1).').',...
    [1,y_stop-1,z_stop-2]);

KExZ=repmat((K.Ex(x_start+1:x_end-1).*deltax(x_start+1:x_end-1).').',...
    [1,y_stop-2,z_stop-1]);
KEyZ=repmat(K.Ey(2:y_stop-1).*deltay(2:y_stop-1).',[x_end-2-(x_start-1),...
```

```
    1,z_stop-1]);
```

.12 res_plot.m

```
 %results plotter
FR=frame_count; %total number of frames
view(114,14)
%% Main plot


for n=1:FR


    [az,el]=view;
    surf(trans_vect,prop_vect(1:x_stop),(squeeze(Res(1,n).Px(:,1,:)./...
        (100^2)))); scale_lim=50e7; zlim([-1,1].*scale_lim);
%   surf(trans_vect,prop_vect(1:x_stop),(squeeze(Res(1,n).Ey(:,1,:)-...
%       0*media(:,y_cent,:)))); scale_lim=50e6; zlim([-1,1].*scale_lim);
%   surf(trans_vect(lay_start-2:lay_stop+2),...
%         prop_vect(SIW_start:SIW_stop),...
%         squeeze(Res(1,n).EPF(SIW_start:SIW_stop,1,...
%         lay_start-2:lay_stop+2)./ep0));
% scale_lim=175; zlim([0,1].*scale_lim);
    zlim([-1,1].*scale_lim);
    set(gca,'CLim',[-.4,1].*scale_lim);
    ylabel('Propagation (m)')
    xlabel('Transverse (m)')
    zlabel('E_y amplitude at the center of the guide (V/m)')
%   zlabel('P_x (W/cm^2) @ y center ')
    shading flat
```

```
%   colormap(gray)
    grid on
    title(['Time step #',num2str(n*frame_step)])
    view(az,el) %recycle current positon
    drawnow
    pause(an_rate)
end



%% y center cut
clf; set(gcf,'visible','on');
for n=1:10:final_n

    plot(prop_vect(1:size(P_flow,1)),P_flow(1:end,n));
    scale_lim=6e7;
    ylim([-1,1].*scale_lim);
    ylabel('Total P_{flow} [W] through z-y planes')
    title(['Time step #',num2str(n)])
    xlabel('Propagation Dimension [m]')
    grid on
    pause(an_rate)
end

%% P_flow at loc vs. time
clf;
T2loc=ft_look;
T1loc=x_dr+10;
```

```
PfT1=P_flow(T1loc,:);

PfT2=P_flow(T2loc,:);

subplot(2,1,1)

hold on

plot([1:1:size(P_flow,2)]*dt,[PfT1].')

plot([1:1:size(PfT2,2)]*dt,[PfT2].','--r')

hold off

grid minor

xlabel('Time [s]')

ylabel('P_{flow}')

title('P_{flow} vs. Time')

legend(sprintf('Input @%2.0i cells from Source',T1loc-x_dr),...

    sprintf('Output: @%2.0i cells from Source',...

    T2loc-x_dr),'location','best');


fs=dt;

NFFT=2^(nextpow2(size(P_flow,2))+5);

Pff1=fft(PfT1,NFFT)/size(P_flow,2);

Pff2=fft(PfT2,NFFT)/size(PfT2,2);

f_scale=Fs*linspace(0,1,NFFT);

subplot(2,1,2)

hold on

plot(f_scale(1:end)./1e9,abs([Pff1(1:end)].'))

plot(f_scale(1:end)./1e9,abs([Pff2(1:end)].'),'--r')

hold off

xlim([0 50])

xlabel('Frequency [GHz]')
```

```
ylabel('|P_{flow} (f)|')
legend(sprintf('@%2.0i cells from Source',T1loc-x_dr),...
    sprintf('@%2.0i cells from Source',T2loc-x_dr));
grid minor



%% Total energy vs space
for n=1:20:size(P_flow,2)
   plot([sum(P_flow(:,1:n),2)*dt, sum(P_flow,2)*dt]);
   xlabel('Spatial Step')
   ylabel('Total Energy')
   title(sprintf('Through time step %1.0i',n))
   drawnow
   pause(an_rate)
end
```

Appendix B: FDTD Validation

The core FDTD algorithm (without nonlinearity) was validated by simulation of the fabricated X-band structure in Chapter 8. A nonuniform grid was used with the minimum lattice space set to $\Delta_{min} = \lambda_{min}/60$, where $\lambda_{min} = c/(\sqrt{\varepsilon_{r_{LTCC}}} f_{max})$. The maximum frequency of interest was chosen as twice the center operating frequency: $f_{max} = 20\ GHz$. Simulation used either a band limited ($f_{c_{10}}$ to $f_{c_{20}}$) source (Figure 2) or a wide band Gaussian pulse source (Figure 3). The source was applied to the microstrip as a soft source setting of vertical field components between the microstrip trace and the ground plane, as given in (1), and shown in Figure 4, where b is the substrate thickness (SIW height).

$$E^n_{y(x_{dr},y,z)} = E^n_{y(x_{dr},y,z)} + \frac{V_s(n)}{b} \tag{1}$$

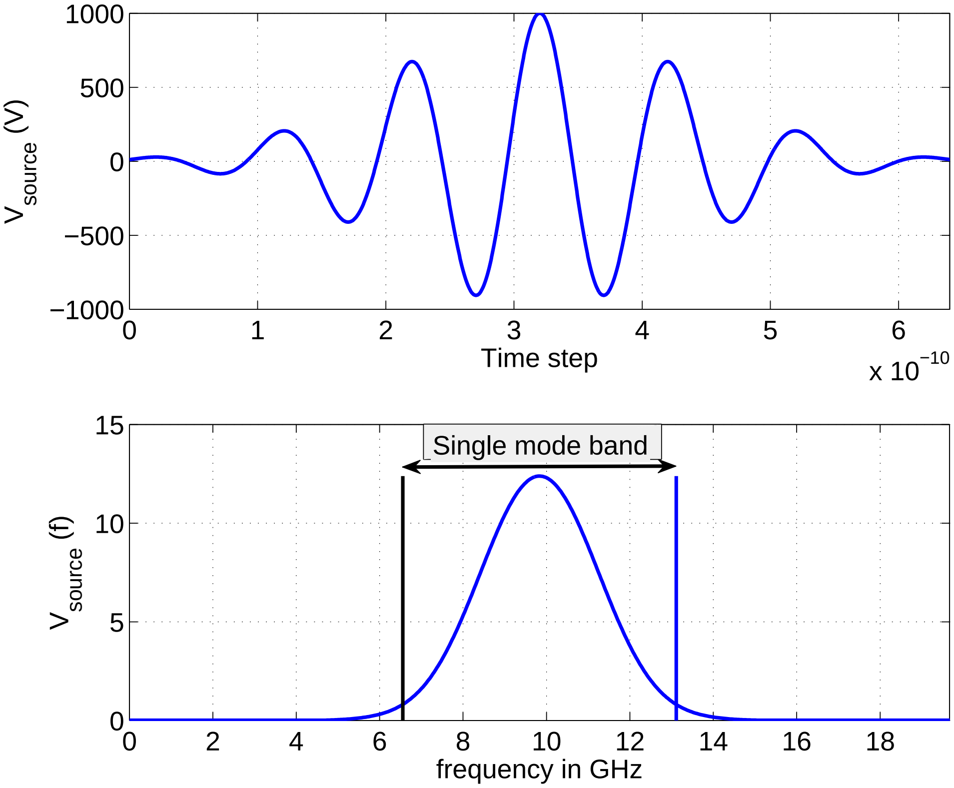

Figure 2: Band limited source and the associated voltage spectrum

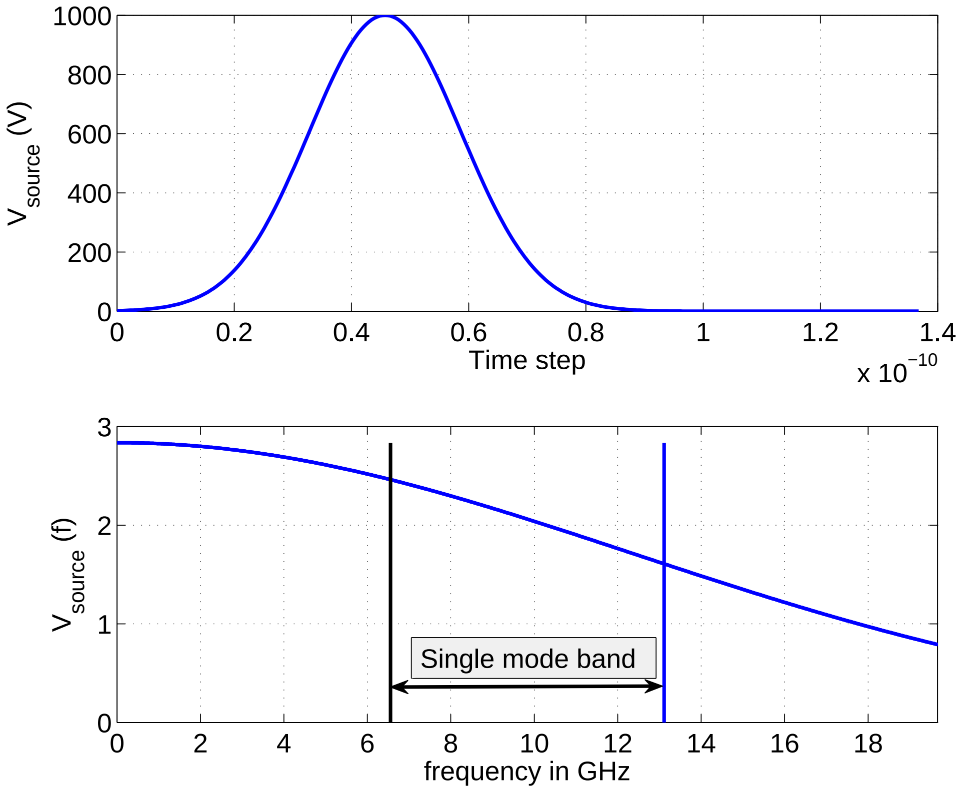

Figure 3: Wide band source and the associated voltage spectrum

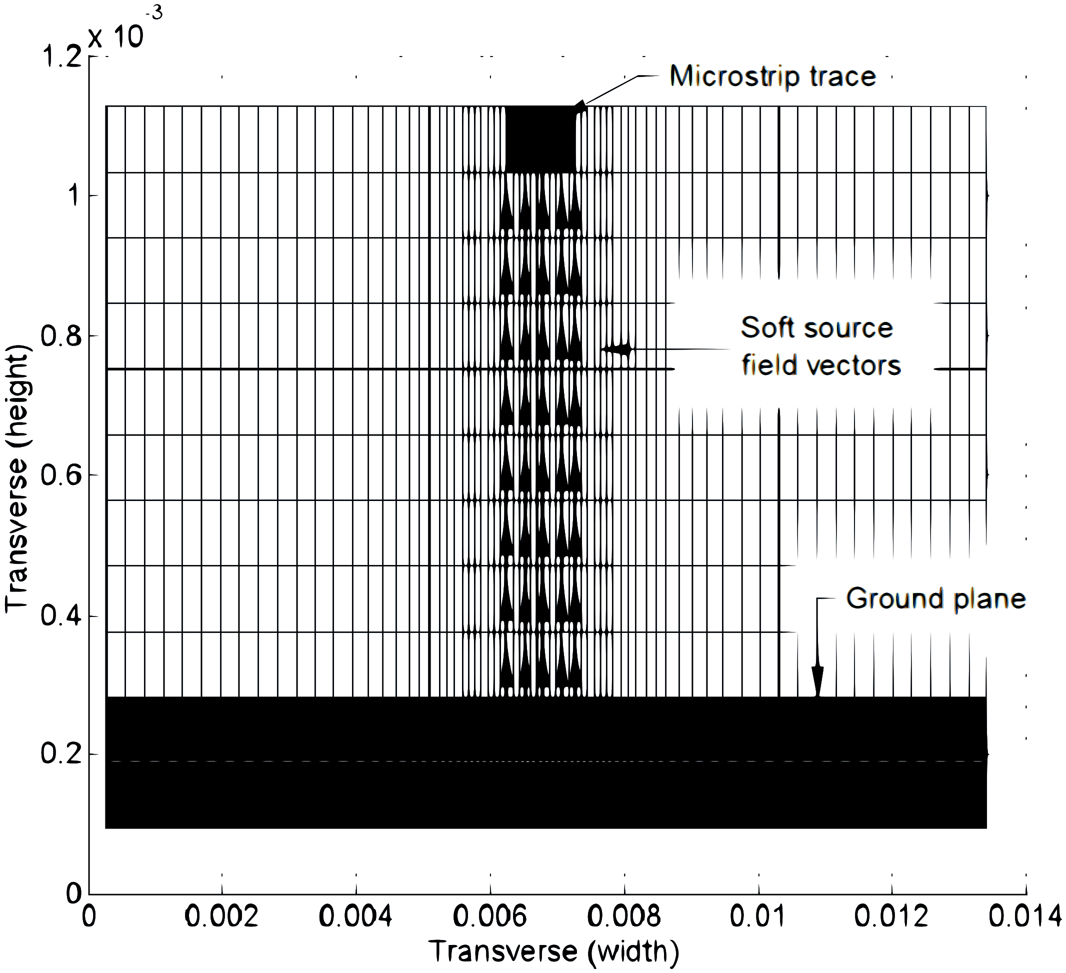

Figure 4: Source electric field vectors

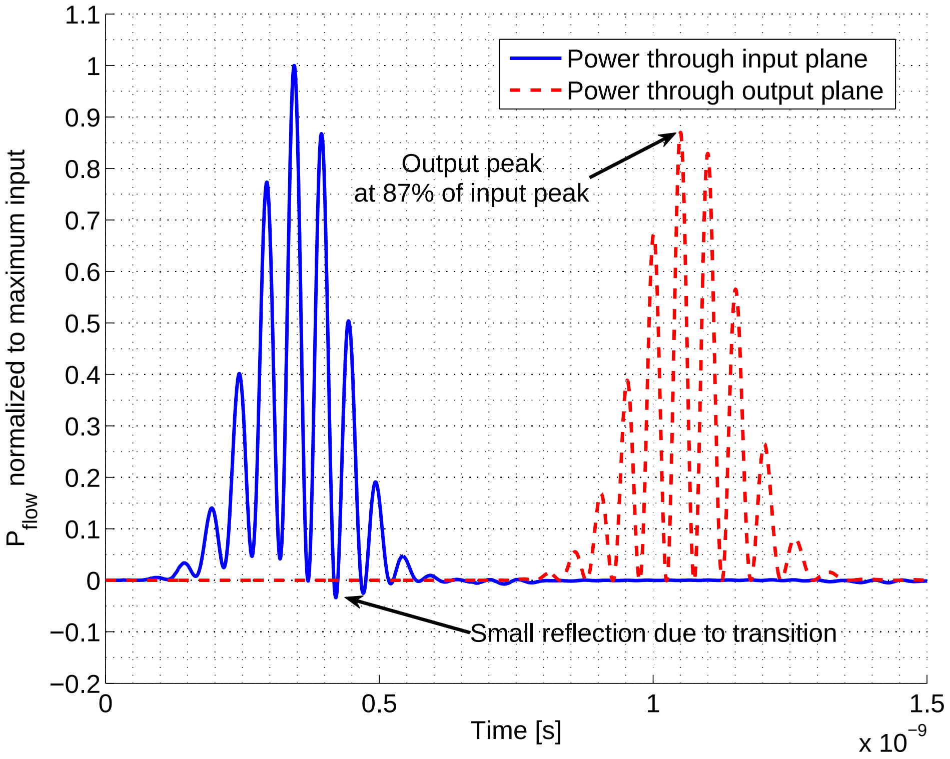

Figure 5: Input and output power resulting from a band limited source

When the band limited source is used, a very small reflection occurs due to the tapered microstrip transitions, as can be seen in Figure 5. This is expected since the transition length is a function of wavelength. The large conductivity of the assumed silver metalization results in a small loss from input to output of only $\sim 0.6\ dB$.

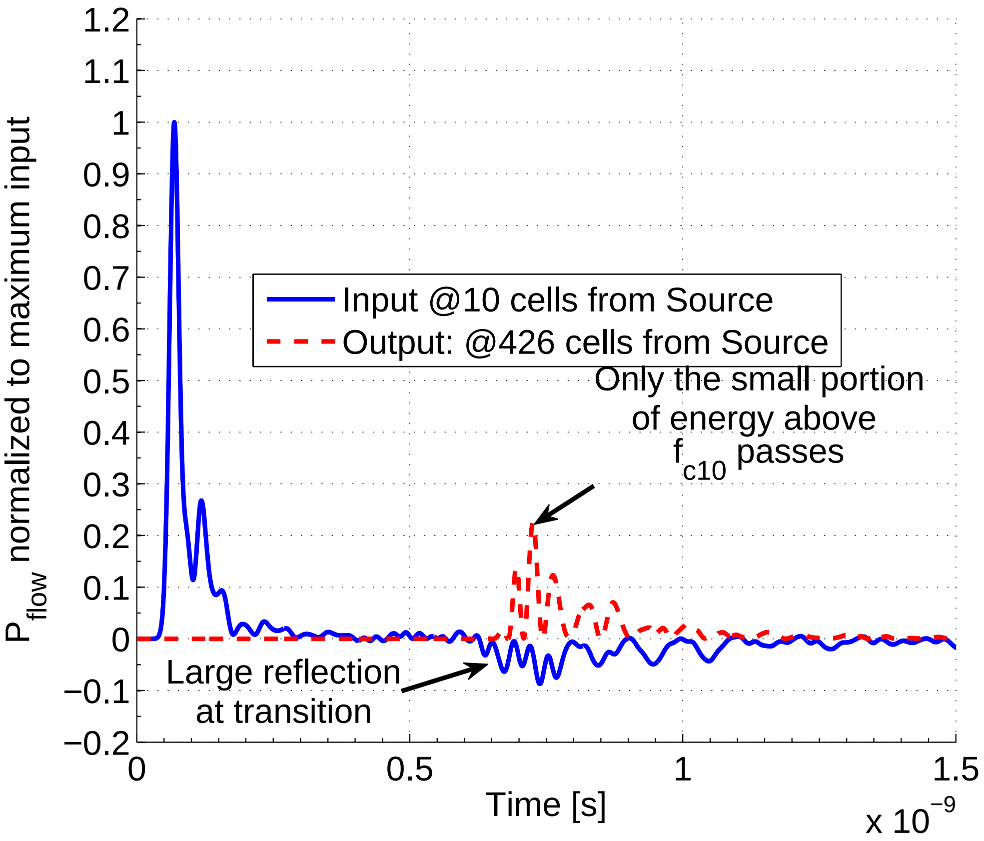

Figure 6: Input and output power resulting from a wide band source

Using the wide band Gaussian pulse, significant reflections can be observed returning through the input plane, as represented by negative values in Figure 6. The spectrum of the input power, as shown in Figure 7, is a result of the complex combination of the multiple reflections. A close examination of the output power spectrum reveals a deep null at $f \approx 2f_{c_{10}}$, which corresponds to the expected high-pass filtering effect of the waveguide. This explains why only a small option of the power passes from input to output.

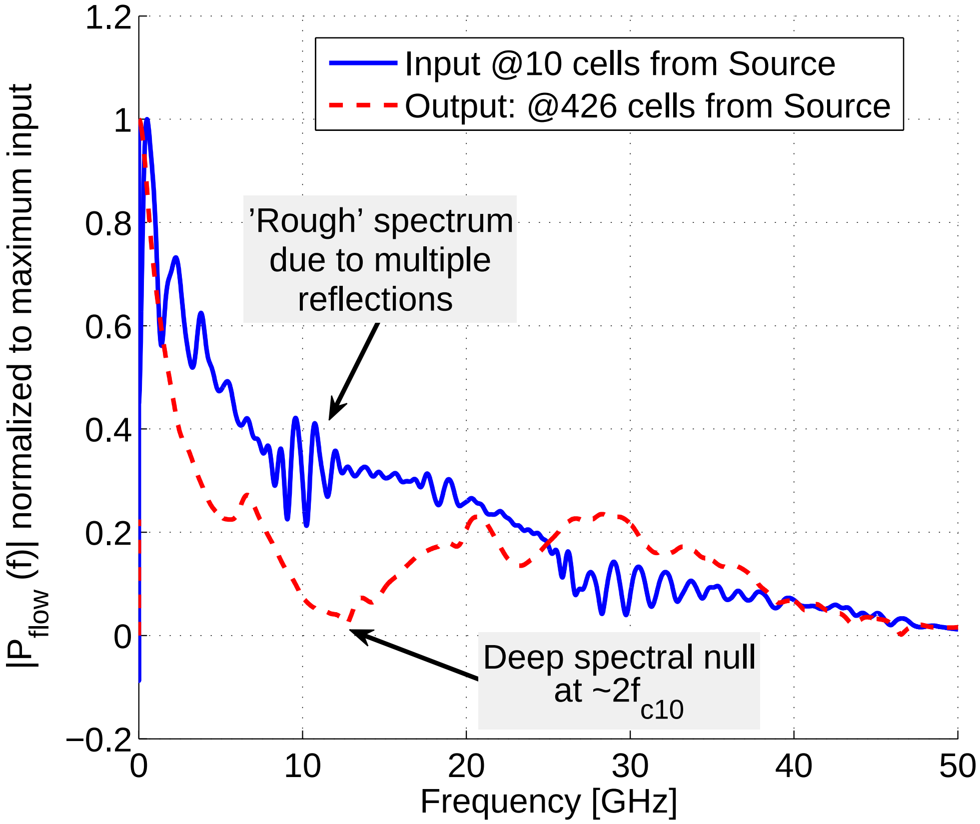

Figure 7: Input and output power spectrum resulting from a wide band source